Measurement of the $\gamma n \rightarrow K^0\Sigma^0$ photoproduction at the BGOOD experiment and the relation to possible pentaquark states

Dissertation
zur
Erlangung des Doktorgrades (Dr. rer. nat.)
der
Mathematisch-Naturwissenschaftlichen Fakultät
der
Rheinischen Friedrich-Wilhelms-Universität Bonn

von
Katrin Kohl
aus
Troisdorf

Bonn, September 2021

Angefertigt mit Genehmigung der Mathematisch-Naturwissenschaftlichen Fakultät der Rheinischen Friedrich-Wilhelms-Universität Bonn

1. Gutachter:	Prof. Dr. Hartmut Schmieden
2. Gutachter:	Prof. Dr. Sebastian Neubert
Tag der Promotion:	16.03.2022
Erscheinungsjahr:	2022

Abstract

Hadrons are particles consisting of quarks bound by the strong force. Ground states and lower lying excitations can be described successfully as mesons consisting of quark-antiquark pairs and baryons consisting of three quarks. At higher excitation energies however, discrepancies between the theoretical description and the experimental observations become obvious. Multi-quark structures consisting of $qq\overline{qq}$ or $qqqq\overline{q}$ could explain the observations. These could be realized as compact colour bound structures or meson-meson or meson-baryon type systems in analogy to the binding of nucleons in a nucleus. Experimental results have confirmed tetra-quark and penta-quark objects to exist with a minimal quark content of $c\bar{c}u\bar{u}$ (X(3872) discovered at Belle) and $uudc\bar{c}$ (P_C states discovered at LHCb) respectively.

Also in the uds-quark sector interesting observations have been made. A cusp in the cross section of the reaction $\gamma p \longrightarrow K^0\Sigma^+$ could be explained by the same model that predicted the abovementioned penta-quark states at LHCb. The structure is described as an interference of intermediate $K^*\Lambda$ and $K^*\Sigma$ states, amplified by the presence of a vector meson-baryon dynamically generated $K^*\Sigma$ resonance, the $N^*(2030)$. This resonance is the strange quark analogue to the P_C states in the charm quark sector. From this model a prediction is made for the reaction on the neutron $\gamma n \longrightarrow K^0\Sigma^0$. The destructive interference leading to a cusp in $\gamma p \longrightarrow K^0\Sigma^+$ becomes constructive and produces a peak in $\gamma n \longrightarrow K^0\Sigma^0$. An observation of this peak would be a smoking gun signal for meson-baryon type resonances to exist not only in the charm quark sector, but also in the strange sector.

In this thesis the differential cross section of $\gamma n \longrightarrow K^0\Sigma^0$ is measured at BGOOD at ELSA from threshold to a beam energy of 2 600 MeV. A peak is observed at 1 750 MeV in the angular range $0.2 < \cos\theta^K_{\mathrm{CM}} < 0.5$. The available statistics prevent a final claim of evidence, also the structure originating from "conventional" resonances can not be strictly ruled out. However, shape and position are consistent with the model of the vector-meson baryon dynamically generated state. The enhancement being real is further supported by findings on the photoproduction of $K^+\Lambda(1405)$. A structure in the cross section is described by a triangle singularity fed by the same $N^*(2030)$ $K^*\Sigma$ type resonance, indicating that also the enhancement observed in the $\gamma n \longrightarrow K^0\Sigma^0$ cross section is caused by this predicted resonance.

Acknowledgements

I would like to thank everyone who supported me during my thesis. Special thanks goes to Prof. Schmieden for making this thesis possible and for giving me a very interesting topic. I would also like to thank Prof. Neubert for his advise on hypothesis tests. Finally I want to thank all members of the working group for making the past years the exciting time that they were.

Contents

CHAPTER 1

Introduction

Since ancient times it is a human desire to understand the principles and building blocks that form our matter. The ancient Greeks thought the atom (from Greek atomos, meaning undivisible) to be the smallest building block. It took until the 19th century to discover that such atoms indeed exist. Little later it became obvious they are not the most basic matter constituents, but posses an inner structure. With the discovery of the electron by J.J. Thomson in 1897 [1] there was first evidence of subatomic particles. In Thomson's model of the atom these electrons where distributed in a positively charged volume. A few years later Rutherford concluded from his famous experiment, where he bombarded alpha particles on gold foil [2], that an atom has a small positively charged nucleus which contains most of the atoms mass, but makes up only a tiny fraction of its size. In 1913 Niels Bohr described the atom as a system of a small dense positively charged nucleus, with negatively charged electrons orbiting around the nucleus [3].

Technological progress in the next decades allowed to investigate smaller and smaller particles. Nuclei were shown to consist not only of positively charged protons but also neutral particles called neutrons. More and more of such subatomic particles were discovered and initially thought to be elementary particles. The large number lead to the term "particle zoo".

In the 1960s their number had become so large, that is was clear, they could not be all elementary. From later experiments it was concluded that there must be even smaller particles, called quarks, which are summarized in the Standard Model of particle physics shown in figure 1.1. As of today quarks are considered point-like elementary particles that have no substructure.

The "zoo" particles consisting of quarks and bound by the strong force were called hadrons. According to the quark model, hadrons are classified in groups with either three valence quarks (baryons) or quark-antiquark pairs (mesons). Based on SU(3) flavour symmetry, these hadrons can be sorted into different multiplets depending on their spin. Quarks have spin S=1/2 and are therefore fermions.

In mesons the spins of the quark-antiquark pair can be either aligned or anti-aligned, resulting in a spin of the meson of either S=0 or S=1. In Fig. 1.2 the two ground state (L=0) nonets for pseudo-scalar ($J^P = 0^-$) and vector mesons ($J^P = 1^-$) are shown. P denotes the parity and J=L+S is the total angular momentum combined of spin S and orbital angular momentum L.

In baryons the spins of the three valence quarks are oriented to form a total of either 1/2 or 3/2. The corresponding ground state octet with $J^P = 1/2^+$ and decuplet with $J^P = 3/2^+$ are shown in Fig. 1.3. In each of the multiplets the particles are sorted by the strangeness quantum number S, not to

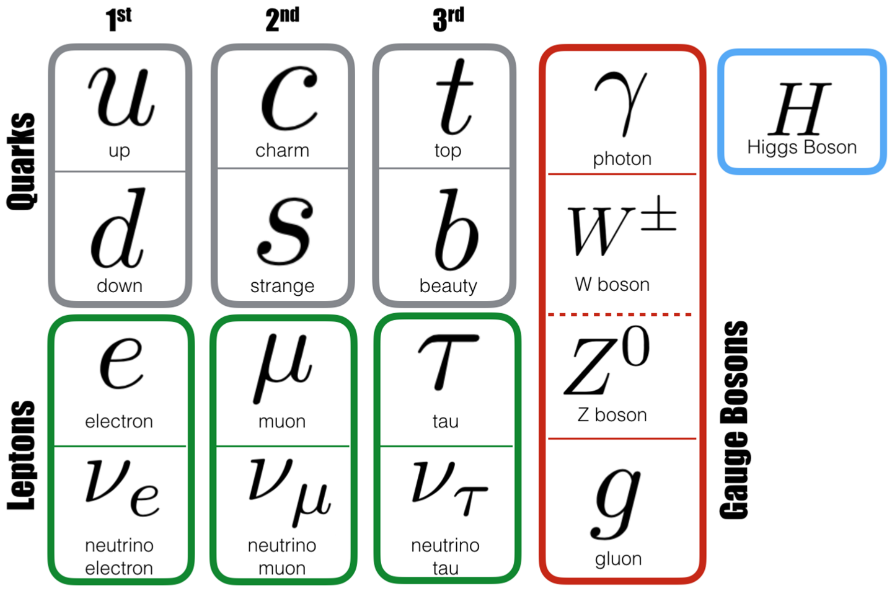

Figure 1.1: Overview of the elementary building blocks of matter, summarized in the Standard Model of particle physics. Figure taken from Ref. [4]

be confused with the spin; and I_3 the third component of the Isospin.

Inside hadrons the quarks bind together through the strong colour force. The interaction of colour carrying particles is described by quantum chromodynamics (QCD). The gluon is the exchange particle of QCD, analogous to the photon being the exchange particle of quantum electrodynamics (QED) which describes the interaction of electrically charged particles. While the photon does not carry charge, the gluon does carry colour. This leads to the two phenomena known as *asymptotic freedom* and *confinement* that are special to QCD.

Asymptotic freedom describes the effect of the interaction between quarks to become asymptotically weaker for low distances. As it carries colour, the gluon can bind to itself. This makes the relative strength of the resulting force, parametrized by the strong coupling constant α_S, strongly dependent on the distance scale. Fig. 1.4 shows the running of α_S as a function of the momentum transfer scale Q. This momentum scale correponds to the inverse of the distance scale. For very high momentum, or low distances, the coupling is small.

For decreasing momentum or increasing distance, the coupling becomes very strong, leading to *confinement*. Quarks and gluons carrying colour can not exist freely, they are always bound in colour neutral hadrons[1]. It is not possible to separate quarks from each other without creating new quarks.

The constituent quark model is very successful as ordering scheme of the ground states in the meson and baryon sector (as e.g. depicted in Fig. 1.2 and 1.3). Also for the inevitably emerging excitations it seemed to work relatively well at lower excitation energies, though at higher excitation energies issues start to appear. In the nucleon octet already at the lowest excitations the parity ordering is reversed. In the conventional quark model, the lowest excited baryon is expected to have spin parity $1/2^-$. However,

---

[1] With the exception of the top quark, which, due to its enormous mass, decays faster than the time hadronization would require.

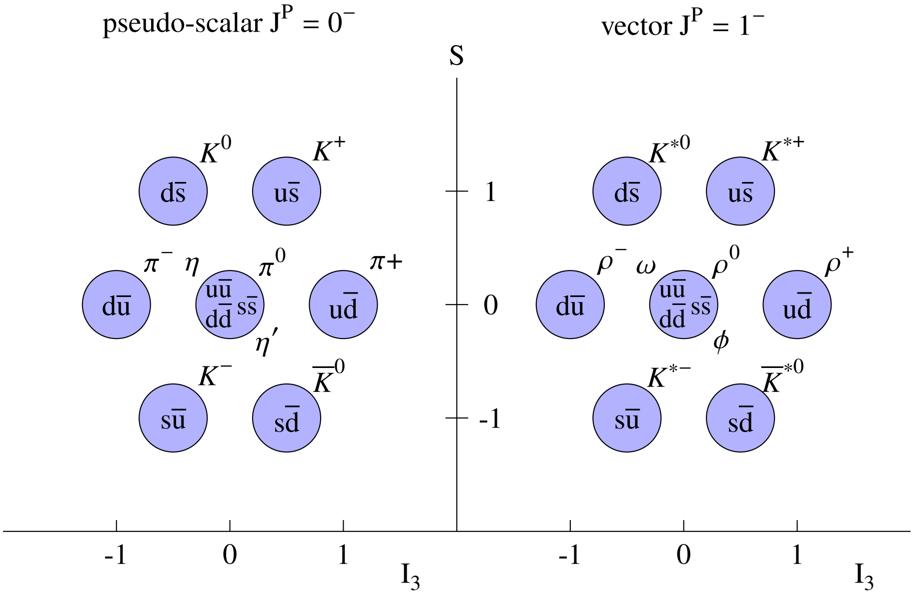

Figure 1.2: Multiplets of pseudo scalar (left) and vector (right) meson states. The quark-antiquark components are given in the circles with the names next to it. The mesons are sorted by strangeness (S) and Isospin (I_3).

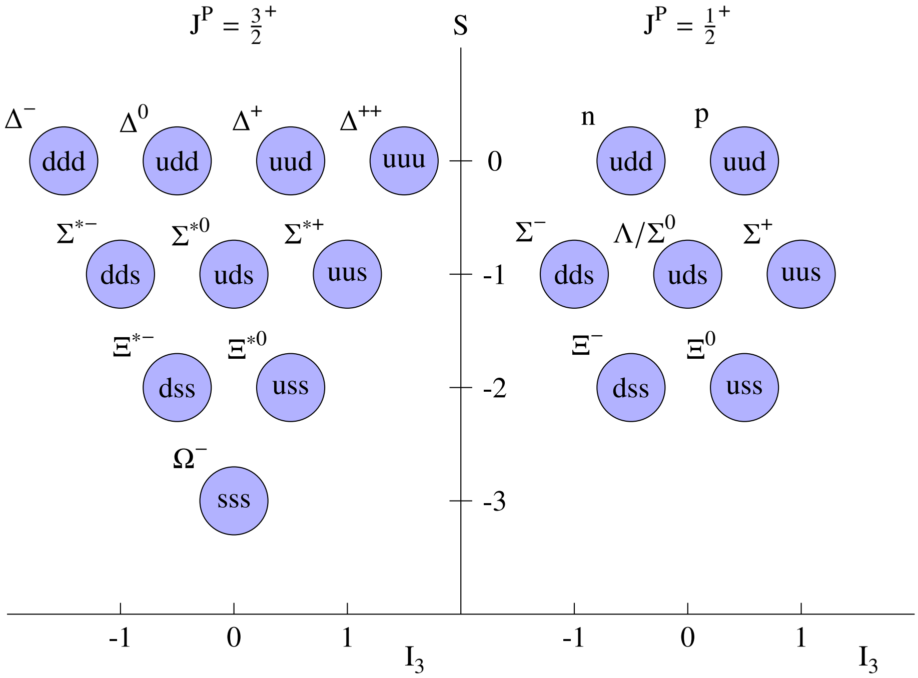

Figure 1.3: Baryon states with $J^P = \frac{3}{2}^+$ (left) and $J^P = \frac{1}{2}^+$ (right). The ordering scheme within the multiplets is the same as in Fig. 1.2.

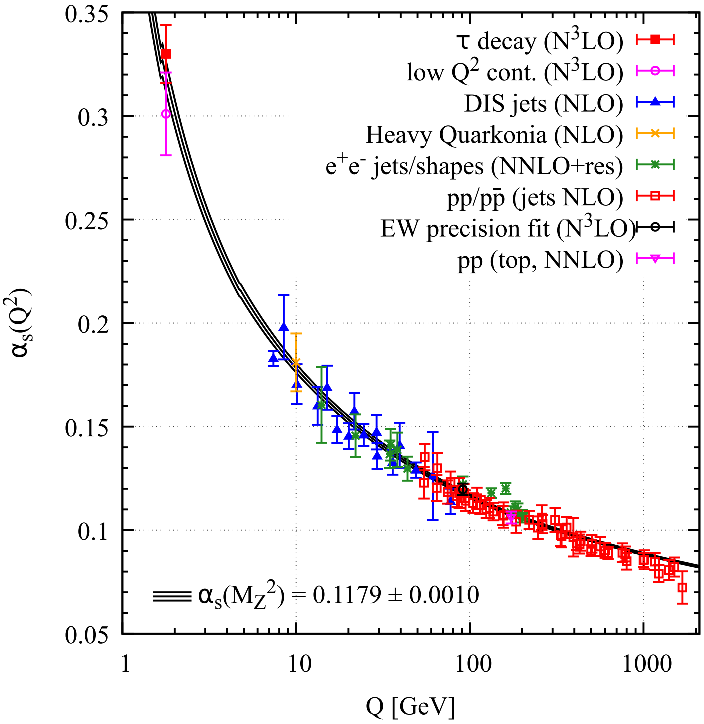

Figure 1.4: Measurements of the strong coupling constant. Figure taken from Ref. [5].

experimentally the lowest excited state is the N(1440) with spin parity $1/2^+$. The lowest negative parity nucleon resonance is the N(1535), which is almost 100 MeV heavier. Additionally at higher excitation energies significantly more states are predicted than could be observed.

These problems could be explained by introducing multi-quark structures, containing $q\bar{q}q\bar{q}$ for mesons and $qqqq\bar{q}$ for baryons. These objects can be realized either as compact colour bound structures, or as meson-meson or meson-baryon type systems in analogy to the binding of nucleons in a nucleus.

There is impressive confirmation of this theory through new experimental results in the c-sector by Belle and the LHCb experiment, where the X(3872) [6] was first identified as a tetra-quark object with minimal quark content of $c\bar{c}u\bar{u}$, and P_C pentaquark states [7–9] with minimal quark content of $uudc\bar{c}$ were discovered.

Also the concept of meson-baryon type systems is no new invention. Before the quark model existed, the $\Lambda(1405)$ was predicted to be a meson-baryon molecule composed of $\overline{K}N$. With the development of the constituent quark model it was described as an excited baryon with quark content uds. Modern LQCD calculations [10] suggest again a bound meson-baryon component and is first evidence, that also in the uds-quark sector structures beyond the conventional constituent quark model exist.

In the uds quark sector another interesting observation has been made at CBELSA/TAPS [11]. In the $\gamma p \to K^0\Sigma^+$ cross section an unexpected cusp has been observed, that could not be explained with conventional quark models. It could be described however, by the same theoretical model, that predicted the P_C states at LHCb. This model also gives a prediction for the cross section on the neutron $\gamma n \to K^0\Sigma^0$. In contrast to the cusp observed in the $\gamma p \to K^0\Sigma^+$ a peak is predicted in the $\gamma n \to K^0\Sigma^0$ cross section, originating from interference of $K^*\Lambda$ and $K^*\Sigma$ intermediate states, magnified by a vector meson-baryon dynamically generated resonance, a $K^*\Sigma$ type "pentaquark" state, the $N^*(2030)$ resonance. An observation of the predicted peak would be a *smoking gun* signal for such meson-baryon type resonances to exist in the strange quark sector, in analogy to the P_C states in the charm quark sector. Measurement of the $\gamma n \rightarrow K^0\Sigma^0$ cross section in the energy region of the predicted peak, i. e. the K^* threshold region is the subject of this thesis.

The thesis is ordered as follows. Chapter 2 will give a more detailed introduction to multi-quark states beyond the conventional quark model and explain their role in the investigated cross section. In chapter 3 the setup of the BGOOD experiment, which was used for the measurement, will be explained and in chapter 4 the challenges of simulating a reaction on the deuteron as a neutron target, will be discussed and a new event generator is introduced. The analysis steps on the way to extract a signal yield and to measure the differential cross section are explained in chapter 5 and 6, followed by the results in chapter 7. In chapter 8 the thesis is summarized.

CHAPTER 2

Unconventional quark structures

This chapter discusses unconventional quark structures beyond the constituent quark model. They are unconventional in a sense, that they have more than the usual qqq or $q\overline{q}$ quark configuration, which is beyond the constituent quark model, but not prohibited in QCD. In the charm quark sector many such structures have meanwhile been observed, but there is indication for them to exist in the strange quark sector as well. In this chapter several of these observations are presented and their possible internal structure is discussed.

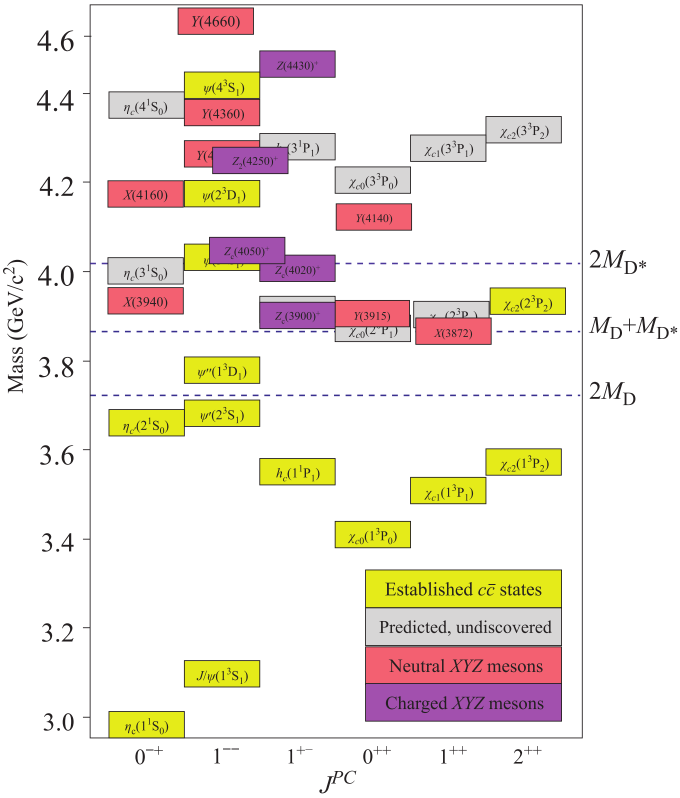

Figure 2.1: Spectrum of predicted and measured charmonium and charmonium-like states. Figure from Ref. [12]

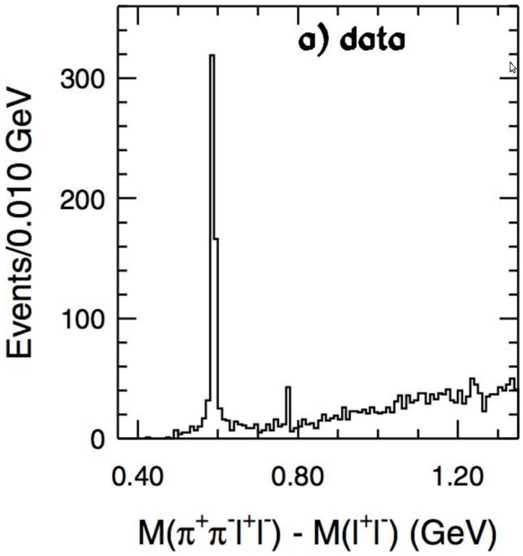

Figure 2.2: Distribution of the difference of invariant masses of $(\pi^+\pi^- l^+ l^-)$ and $(l^+ l^-)$, l being either μ or e. Figure taken from Ref. [6]

The constituent quark model has been a great success in explaining the ordering scheme of hadrons. While theoretical calculations and experimental results agree on the ground states, higher lying states show discrepancies. Calculations from LQCD predict many states that have not been observed yet. Additionally the parity ordering in the nucleon octet is reversed for the lowest excitations. In contrast to the expectation from the constituent quark model, the lowest excited state has spin parity $1/2^+$ instead of $1/2^-$.

These issues can be explained by introducing multi-quark structures with a quark content beyond the conventional qqq or $q\overline{q}$ quark configuration. In recent years more and more such structures were discovered. Exemplary Fig. 2.1 shows the spectrum of charmonium and charmonium-like states. The lower lying states are well established. However, above 3.8 GeV several of the predicted states are not yet experimentally confirmed, but several charged and neutral states are observed where none were predicted. Many of these states can not be explained with the conventional quark model.

So far these multi-quark structures have only been observed in the (heavy) charm and bottom quark sector, but there are interesting parallels to the strange sector as will be shown later in the chapter.

The first discovery of such a state was made by Belle in 2003 [6]. They discovered a new particle called X(3872) when studying the $J/\psi\pi^+\pi^-$ invariant mass spectrum of B^+ mesons decaying to $J/\psi\pi^+\pi^- K^+$. Figure 2.2 shows the invariant mass difference $\mathrm{M}(\pi^+\pi^- l^+ l^-) - \mathrm{M}(l^+ l^-)$ with l being either μ or e. The well-known $\psi(2S)$ is clearly visible next to another unexpected peak signalling a structure decaying to the same final state. While the quantum numbers would agree with a conventional pure $c\overline{c}$ state, its small width and the observed decay modes are not expected for a conventional hadron. The simplest possible explanation is a tetra-quark structure of $c\overline{c}u\overline{u}$. The discovery was confirmed by BaBar [13] soon after and the LHC experiments [14, 15] a few years later. In fact the X(3872) became one of the most precisely studied unconventional hadrons. Nonetheless the internal structure and the exact way the constituents bind together still remains debated. Models [16–20] including a colour

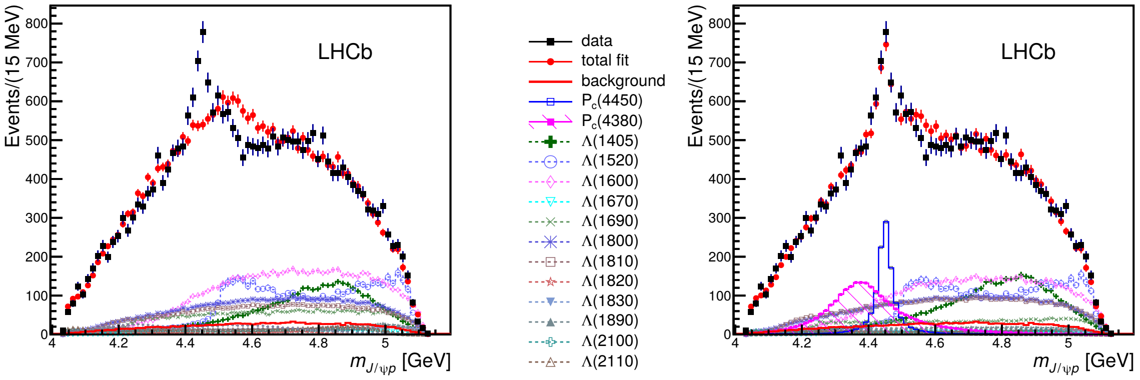

(a) Fit with conventional Λ^* baryons only.

(b) Fit including $P_c(4380)$ and $P_c(4450)$ states.

Figure 2.3: Fit to the distribution of the invariant mass of $J\psi$. Data are shown in black, the full fit in red. The remaining coloured distributions are different Λ contributions. Figures taken from Ref. [7]

	c -sector		s -sector	
state(s)	$X(3872)$	$P_c^*(4380/4450)$	$f_1(1285)$	$N^*(2030/2080)$
π-exchange transition	$D^{*0}\overline{D^0} + D^0\overline{D^{*0}}$	$\Lambda_C^*\overline{D} + \Sigma_c\overline{D^*}$	$K^*\overline{K} + K\overline{K^*}$	$\Lambda^*\overline{K} + \Sigma\overline{K^*}$
quark content	$c\bar{c}u\bar{u}$	$uudc\bar{c}$	$s\bar{s}u\bar{u}$	$uuds\bar{s}$

Table 2.1: Overview over possible parallel meson-baryon states in (hidden) charm and strange sector [27].

bound 4-(anti)quark structure or molecular states which are governed by the interaction between colourless hadrons, in a sense similar to nuclear binding of baryons, are employed to describe the structures. The most natural one is a molecule of $D^0\overline{D^{*0}}$ bound py pion-exchange, the X(3872) mass is right at the threshold to produce $D^0\overline{D^{*0}}$.

In 2015 the LHCb experiment discovered another class of such unconventional hadrons. They are viewed as a pentaquark structure with minimal quark content $uudc\bar{c}$ at around 4.4 GeV [7–9]. This would naturally explain the observed decay pattern and the invariant mass distribution of $J/\Psi p$ in $\Lambda_b^0 \to J/\Psi K^- p$ decays. Fig. 2.3 shows the fit without and with the contribution of the unconventional hadrons. In the second fit two unconventional components $P_c(4380)^+$ and $P_c(4450)^+$ [7] were included. Further investigation [9] showed the latter consists of the two states $P_c(4440)^+$ and $P_c(4457)^+$ and found another state at $P_c(4312)^+$. While the existence of these states is undisputed, the way these quarks bind together within the resonances is unknown. Mechanisms similar to the ones discussed for the X(3872) appear possible, for example a molecular bound state of $\Sigma_c\overline{D}^*$. Again, the threshold to produce the constituents is in direct proximity to the observed peaks.

Several more unconventional states were found in the (hidden) charm sector [21, 22] among them charged Z states which can impossibly be pure $c\bar{c}$ states [23–26]. Fig. 2.1 and Ref. [12] give an overview. All these states have in common, that they can not be explained with conventional quark models.

So far such unconventional states where only seen in the heavy quark sector. If the underlying structure principle was meson-meson or meson-baryon dynamics, then this could work for lighter

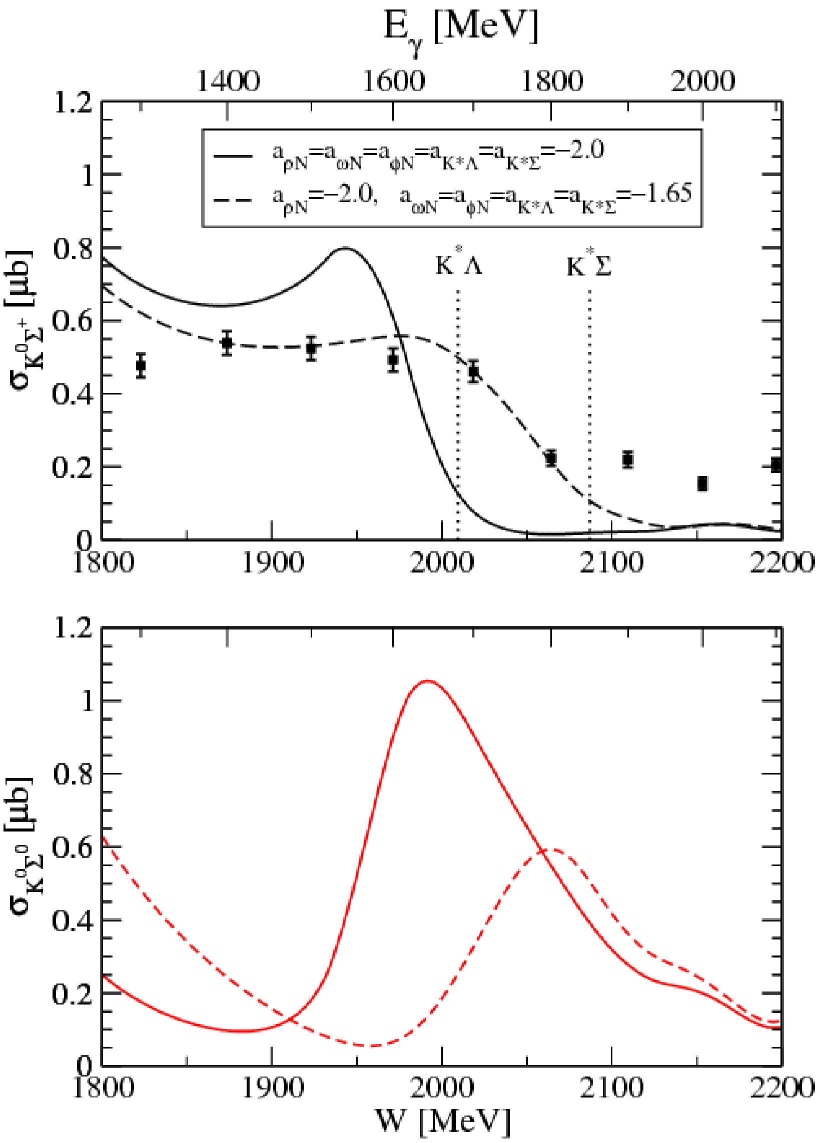

Figure 2.4: Upper plot: $\gamma p \to K^0\Sigma^+$ cross section obtained from two different parameter sets. For the dashed line the parameters were adjusted to fit the measurement of CBELSA/TAPS [11] (black squares). Lower plot: Predicted $\gamma n \to K^0\Sigma^0$ cross section for the same parameter sets. Figure from Ref. [28].

quarks too. Actually, there are interesting parallels between the charm and the strange sector. By exchanging the charm quarks with strange quarks in the mentioned tetra- and pentaquark candidates, lighter multi-quark states can be created. Table 2.1 gives an overview of possible states.

These lighter multi-quark states also lie directly at the corresponding thresholds and could be understood as a molecular type structure. Unconventional multi-quark states in the (hidden) strange sector have not yet been confirmed, but the same theoretical model, that used vector meson-baryon interactions to predict the LHCb pentaquark candidates [29], was extended to describe a cusp like structure observed in $\gamma p \to K^0\Sigma^+$ directly at K^* threshold [11] by including a vector meson-baryon dynamically generated $K^*\Sigma$ resonance, the $N^*(2030)$ (Fig. 2.4 upper plot) [28].

In this interpretation the interference between intermediate $K^*\Lambda$ and $K^*\Sigma$ states is magnified by the presence of this resonance. This interference is destructive in the reaction $\gamma p \to K^0\Sigma^+$. Contrary, for the analogue reaction on the neutron, $\gamma n \to K^0\Sigma^0$, the interference is predicted to become constructive and produce an enhancement (Fig. 2.4 lower plot). An observation of this enhancement would be a *smoking gun* signal for this meson-baryon type resonances to exist in the strange sector.

Investigation of the $\gamma n \to K^0\Sigma^0$ cross section in the region of the $K^*\Lambda/\Sigma$ threshold is the central goal of this thesis. The measured cross section will be compared to the prediction made by E. Oset and A. Ramos [28] to investigate whether the predicted enhancement can be observed. The all neutral channel is difficult to observe, only one previous measurement exists [30], which does not reach high enough energies around the K^* threshold. With the BGOOD experiment the necessary energies are well accessible.

CHAPTER 3

The BGOOD experiment

The BGOOD Experiment [31] at the ELSA accelerator facility in Bonn is dedicated to study hadron excitation spectra in meson photoproduction on a nucleon target. The accelerator provides it with an electron beam up to 3.2 GeV, it is described in chapter 3.1. The electron beam is converted to a real photon beam, this is explained in chapter 3.2. The photons impinge on a target (chapter 3.3) of either liquid hydrogen or liquid deuterium which is surrounded by the central detectors (chapter 3.4). Forward going particles are detected in the forward spectrometer (chapter 3.6), the region between the central detectors and the forward spectrometer is covered by the intermediate detectors, explained in chapter 3.5. At the very end of the experiment the photon flux is monitored (chapter 3.7).

An overview over the experiment is given in Fig 3.1, the orientation of the used coordinate system is also shown there. A more detailed illustration of this coordinate system and the definition of the angles ϕ and θ is shown in Fig. 3.2.

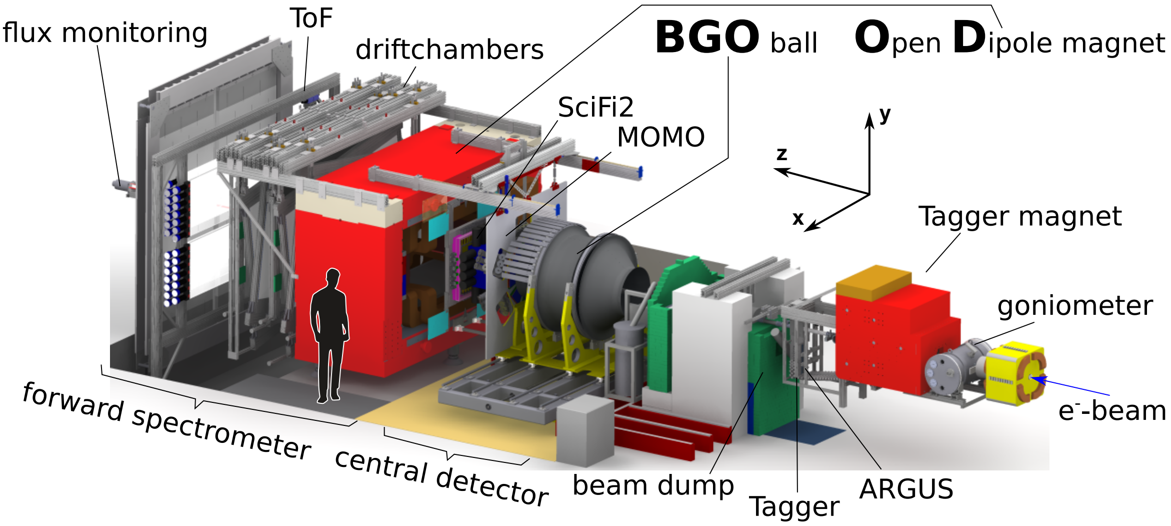

Figure 3.1: Overview of the BGOOD experiment showing the main detector components and a sketch of the orientation of the coordinate system.

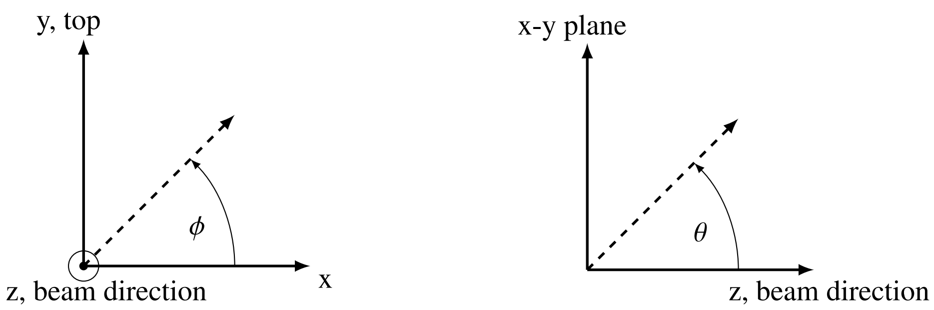

Figure 3.2: Sketch of the coordinate system in the BGOOD experiment. A right hand coordinate system is oriented such, that the z-coordinate is parallel to the beam direction and the x-coordinate is parallel to the floor. The azimuthal angle ϕ is defined as the angle in the x-y plane and the polar angle θ is defined as the angle from the beam direction towards the x-y plane.

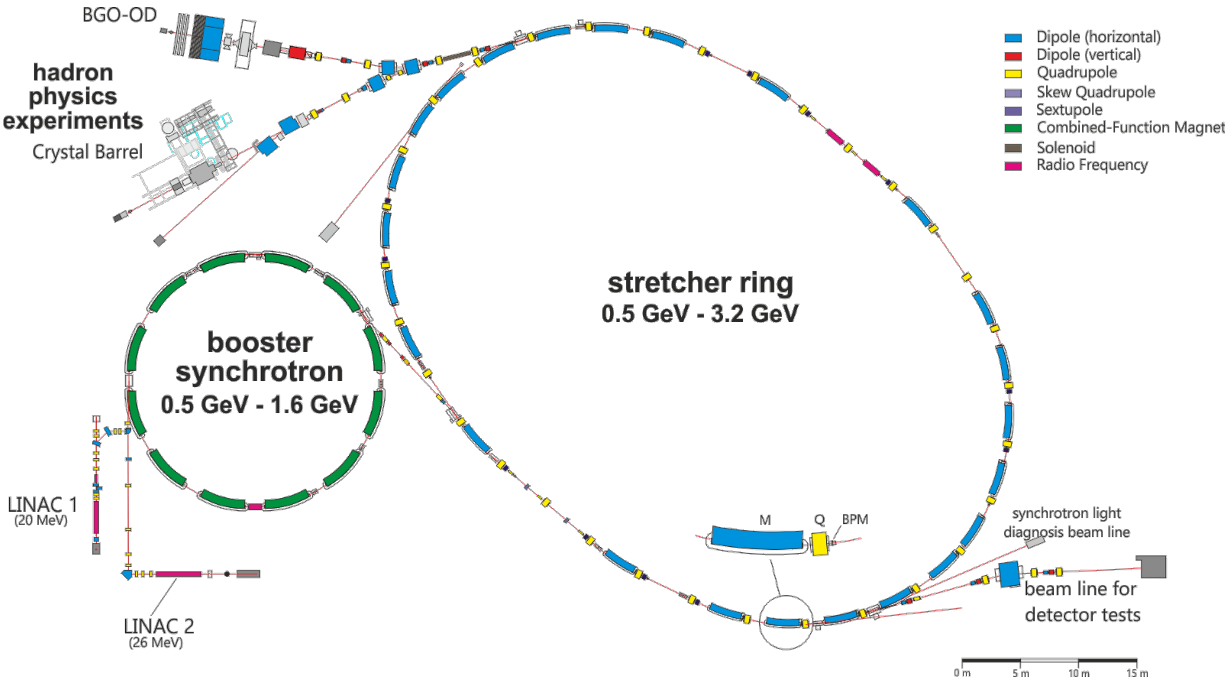

Figure 3.3: Overview of the ELSA accelerator facility in Bonn [32]. The BGOOD experiment is located in the top left corner.

3.1 ELSA

The **El**ectron **S**tretcher **A**ccelerator ELSA[32, 33] is a three stage electron accelerator located beneath the Physikalisches Institut of the University of Bonn. The setup is shown in Fig 3.3. The electrons are emitted from a thermal gun in the first stage and accelerated by the LINAC (linear accelerator) to an energy of approximately 26 MeV. At the time of this thesis only LINAC 2 was operational. The second stage is the booster synchrotron into which the electrons are injected after the LINAC. The booster synchrotron further accelerates the electrons to an energy between 0.5 to 1.6 GeV. The

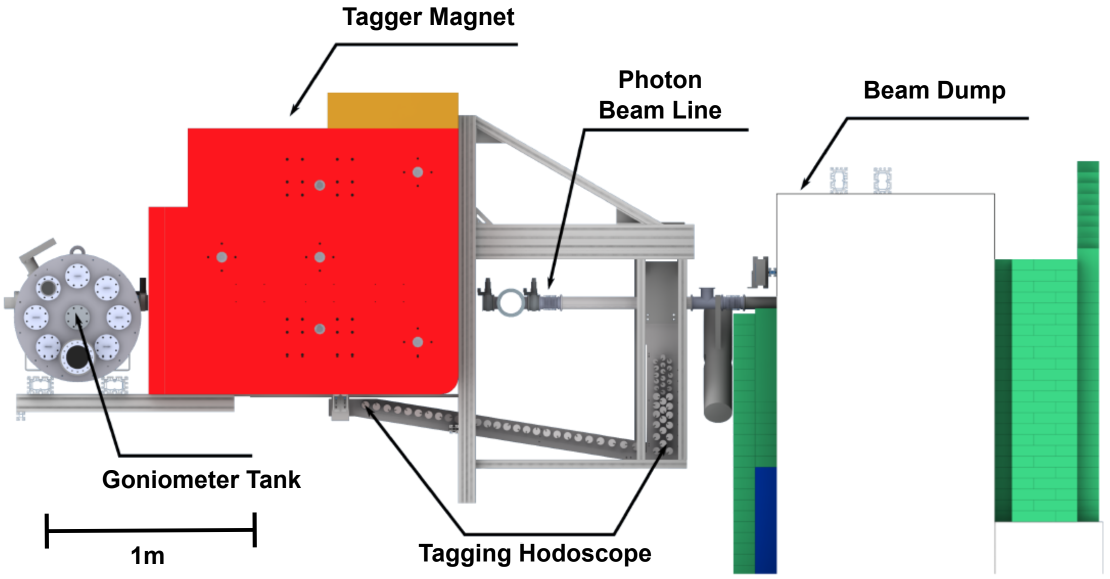

Figure 3.4: Side view of the photon tagging system. The electron beam enters from the left. While the bremsstrahlung photon beam continues through the photon beam line in a straight line, the post-bremsstrahlung electron are deflected by the magnetic field and are detected in the Tagging hodoscope.

third stage, the stretcher ring, is filled in bunches, 2 ns apart, from the booster synchrotron. This is repeated several times until the stretcher ring is filled completely. Then the electrons are accelerated to their final energy of maximum 3.2 GeV and extracted to one of the experiments. The amount of extracted electrons can be adjusted to provide different intensity for the experiment, resulting in a quasi-continuous beam with a duration of 5 to 15 s. After this time period the stretcher ring has to be filled again which takes about 1 s. During refilling no beam is extracted to the experiments.

3.2 Photon Tagging System

The extracted electrons enter the beam line of the experiment and are guided to the experiment. In the photon tagging system a real photon beam is generated via bremsstrahlung and the energy of the resulting photons is determined. Fig. 3.4 shows an overview of this part of the experiment. Inside the goniometer tank different radiators can be precisely aligned to the beam. For producing unpolarized photons different copper radiators with varying thickness are available, polarized photons can be produced by using a diamond radiator of 560 μm thickness [34]. In contrast to the copper radiators, where only a single atom is involved in the bremsstrahlung process, here the whole crystal lattice takes over the recoil momentum. This process, known as coherent bremsstrahlung, enhances the production in one plane, resulting in linearly polarized photons. The effect can be seen as a peak in the energy spectrum convoluted with the $1/E_\gamma$ spectrum of the incoherent production.

The post-bremsstrahlung electrons and photons then enter the Tagger Magnet. While the photons pass the magnetic field unaffected, the electrons are deflected by the Lorentz-force depending on their momentum. They are detected in the Tagging hodoscope, which consists of 120 overlapping scintillators and covers 10% to 90% of the electron beam energy E_0. The segmented structure allows to measure the post-bremsstrahlung electrons energy E' with a precision of $0.55\%E_0$ to $2.28\%E_0$ [34] and determine the energy difference to the electron beam energy $(E_0 - E')$, which is the energy of the bremsstrahlung photon E_γ. Electrons that did not undergo bremsstrahlung are deflected into the beam dump and are stopped there without being measured by the tagging hodoscope.

To further increase the energy resolution in the region where usually the coherent bremsstrahlung peak is expected, the range from 30% to 66% of the electron beam energy E_0 is covered by ARGUS. Scintillating fibres detect electrons with a higher spatial resolution, resulting in a energy resolution between 0.1% and 0.4% of the beam energy [35, 36].

3.3 Target

The photon beam impinges on a target consisting of either liquid hydrogen or liquid deuterium. It is cooled down to around 20 Kelvin by a cryostat system. The target material is contained in an aluminium cylinder of 3 cm inner diameter. To reduce material in the line of the beam the cylinder is closed by 0.1 mm thick Mylar foil and placed inside the vacuum beam pipe. The length of the target cell can be either 5 or 10 cm. Since the Mylar windows expand outwards due to the pressure difference the total length amounts to 6 or 11 cm.

3.4 Central Detectors

The target cell is surrounded by the central detector system, covering the polar angle range between 25° and 155°. The BGO electromagnetic calorimeter is supported by the **M**ulti-**W**ire **P**roportional **C**hambers (MWPC) and the scintillator Barrel. Fig 3.5 shows a slice view of the three detectors around the target system. The MWPC is located directly around the target and is intended to reconstruct charged particle tracks at high precision. The scintillator Barrel, usually called Barrel, surrounds the MWPC and is used to identify charged particles tracks. The most outer part is the BGO electromagnetic calorimeter where the particles are stopped and their kinetic energy is measured. In the following sections, the three detectors are described in more detail.

3.4.1 BGO-ball

The electromagnetic calorimeter was originally used in the GRAAL experiment [37] and consists of 480 crystals of bismuth germanium oxide $(Bi_4GeO_4)_3$. They are arranged in 15 sectors with 32 crystals each, covering the full azimuthal range ϕ and the polar angle range θ from 25° to 155°. To fit the crystals in a round shape different trapezoidal shapes are used. Each crystal covers 11.25° in ϕ and 6° to 10° in θ. Their length of 24 cm corresponds to 21 radiation lengths. The whole structure is build in two halfes and mounted on a rail system to access the detectors and the target inside.

The small radiation length and a good energy resolution is the reason this inorganic scintillator material is chosen for the calorimeter. These advantages come however with a relatively long signal and a modest time resolution. This can be mostly compensated by sampling the signal. With the used electronics a time resolution of 2 ns can be achieved.

The detector is optimised to measure the kinetic energy and position of photons, but also charged particles can be detected. Photons passing through the detector material produce an electromagnetic

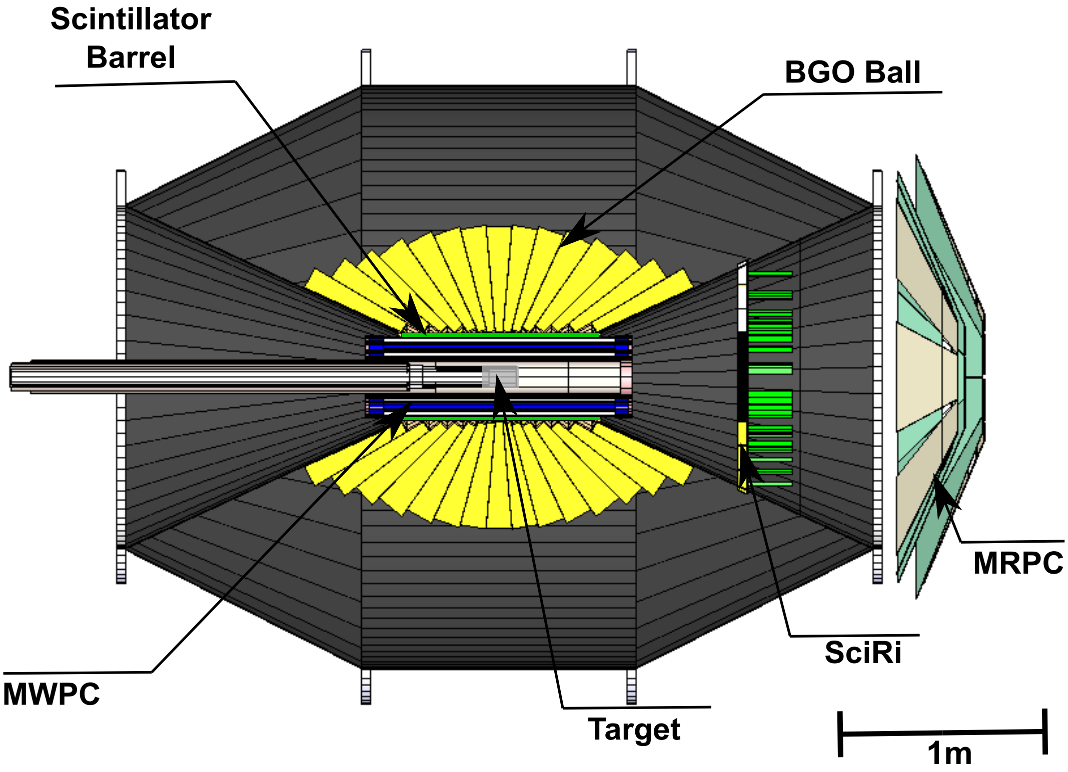

Figure 3.5: Slice view of the central detector system surrounding the target. On the right side the intermediate detectors SciRi and MRPC are shown.

shower which spreads across several crystals. This allows for a better position resolution than the crystal size. To measure the correct energy deposition in the detector a calibration is essential. A first level calibration is done with radioactive ^{22}Na sources placed inside the detector directly around the target. Two characteristic energies at 0.511 MeV and 1.275 MeV can be observed. This is mainly used to match the gain of all channels by adjusting the high-voltage of the photo-multiplier tubes attached to the crystals. Since this procedure alone would require a high linearity of the electronics (the energy deposit during data-taking is usually 100 times larger), a second level calibration is done by reconstructing the π^0 from its 2γ decay and fitting to the π^0 mass peak. A run by run correction is applied to correct for changes in the gain from temperature differences. Additionally a correction is made for each individual crystal. This is done iteratively, since each correction affects the spectra of the other crystals. In Chapter 5 the resulting π^0 mass spectrum is shown for different data sets. More information can be found in Ref. [31].

3.4.2 Scintillator Barrel

Inside the BGO calorimeter 32 plastic scintillator bars are used to distinguish between charged and neutral particles. Each scintillator bar covers 11.25° in ϕ and 25° to 155° in θ with a thickness of

0.5 cm. Since the detector only responds to charged particles a decision can be made whether a signal in the BGO-ball corresponds to a charged or neutral particles track [31].

3.4.3 MWPC

The MWPC consists of two cylindrical gas filled chambers with different diameter, but similar structure. Each chamber is constructed in three layers, two layers of helicaly wound cathode strips around a number of anode wires oriented parallel to the beam direction. This allows reconstruction of tracks very close to the target and also determination of displaced vertices. The MWPC is fully commissioned and taking data, but since the development of the complex software necessary to reconstruct the tracks was still in progress, it was not used in this thesis [31].

3.5 Intermediate Detectors

The intermediate range between the central detectors and the forward spectrometer (10° to 25°) is intended to be covered by the MRPC (**M**ulti gap **R**esistive **P**late **C**hamber). Until this is fully operational SciRi gives position information for charged particles.

SciRi

The scintillating ring detector (SciRi) [38] is build from 96 plastic scintillators segmented in three rings in θ, each ring contains 32 scintillators covering 11.25° in ϕ. The detector is constructed in two halfes to fit in the opening cone of the BGO-ball. The read-out is done with avalanche photo diodes.

MRPC

The design of the experiment intends to cover the acceptance gap between the central detectors and the forward spectrometer with a high accuracy MRPC. This detector is still under commission. Once finished an angular resolution of 2° and a time resolution of 50 ps is expected.

3.6 Forward Spectrometer

Forward going particles with $\theta < 11^\circ$ are detected in the forward spectrometer. Tracking detectors in front of and behind an open-dipole magnet provide information on direction and momentum of the particle. The setup is complemented by time-of-flight measurement to allow full particle identification. Fig. 3.6 shows an overview of the spectrometer. Two scintillating fibre detectors in front of the magnet and eight drift chambers behind measure the particles trajectory. At the very back three time of flight walls complete the setup.

3.6.1 MOMO and SciFi

Tracks of charged particles in forward direction are measured in the two scintillating fibre detectors MOMO and SciFi [39]. While MOMO consists of 6 trapezoidal modules, SciFi consists of layers of horizontal and vertical fibres. Both detector designs leave a hole in the middle, where the photons that did not interact with the target can pass without producing a signal.

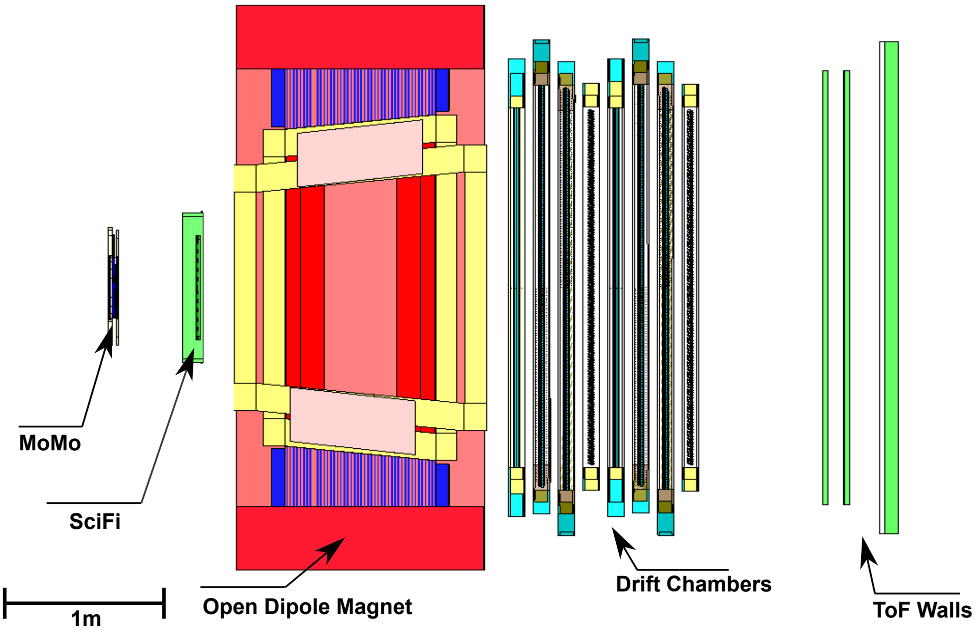

Figure 3.6: Overview of the forward spectrometer

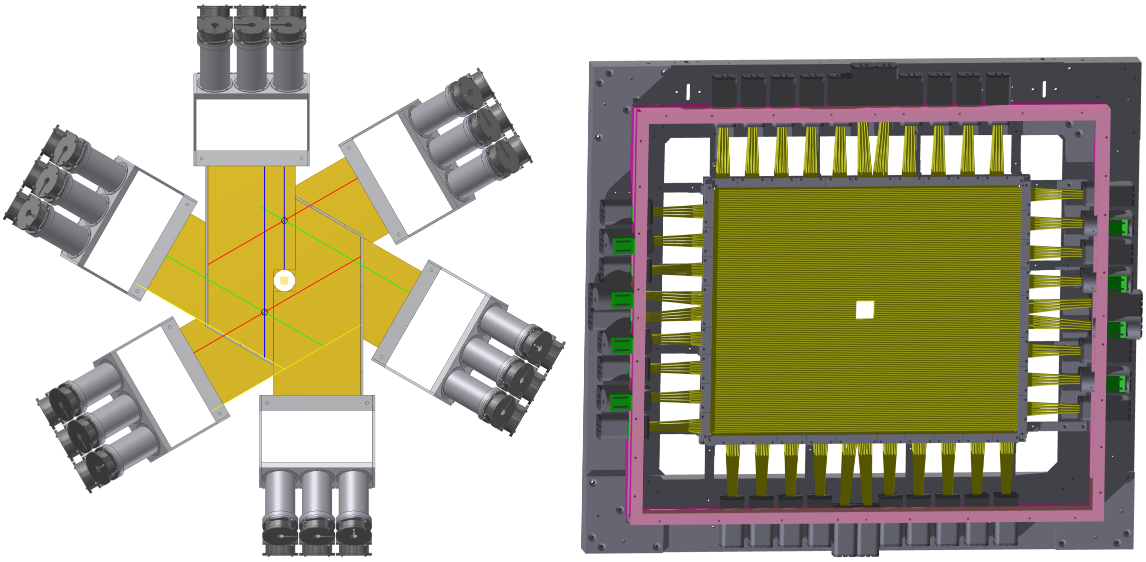

(a) MOMO (b) SciFi

Figure 3.7: CAD drawing of the scintillating fibre detectors MOMO and SciFi. Both structures show an acceptance gap in the middle to let the photon beam pass.

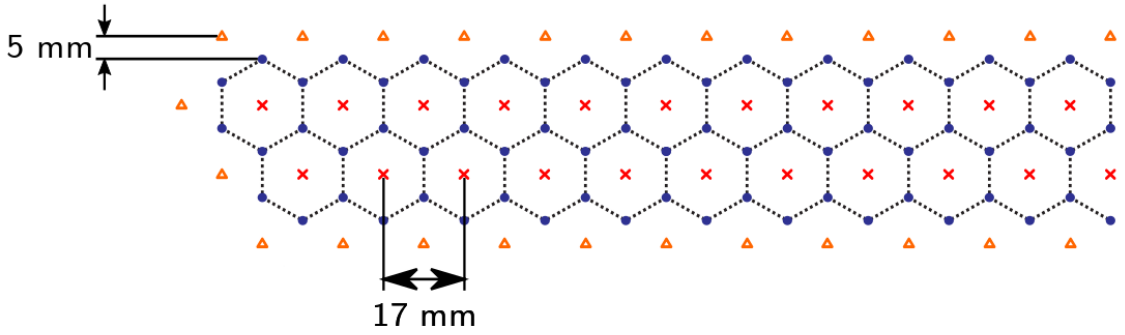

Figure 3.8: Sketch of the structure of the driftchambers. Red crosses are signal wires, blue points are potential wires. The hexagonal geometry of a drift cell is indicated by the blue dotted lines. Field forming wires are shown as orange triangles. (c.f. [41])

3.6.2 Open Dipole Magnet

Behind the two tracking detectors MOMO and SciFi the open dipole magnet, which is a permanent loan from DESY, is placed. The magnetic field in the gap can reach more than 0.5 T [40] and bends charged particles trajectories in the horizontal plane. At these field strength low energetic particles are bent outside of the acceptance of the detectors behind the magnet, so for data-taking usually a 'half field' setting is used. This slightly reduces the momentum resolution, but increases the efficiency especially for low energetic protons.

3.6.3 Drift chambers

The particles tracks behind the magnet are detected with 8 drift chambers with 4 different wire orientations. All 8 chambers together allow to reconstruct particles tracks in 3D space. Each chamber consists of 2 layers of drift cells as shown in Fig. 3.8. The shifted hexagonal structure resolves ambiguities. Each drift cell is formed by potential wires at a high negative voltage (up to 3 kV) around signal sensitive anode wires at ground potential. Field forming wires at ground potential outside the sensitive area complete the setup. In the central region the wires are made insensitive by adding a gold plating to let the photon beam pass [42].

3.6.4 Time-of-Flight Walls

The momentum information from the tracking detectors is complemented by time of flight walls (ToF) to complete particle identification. Three walls of horizontal plastic scintillator bars are read out with PMTs at both ends, which allows the determination of the horizontal hit position in each bar. The vertical position is given by the bar. To determine the time of flight, the time information from the ToF walls acts as a stop signal, the start information is given by the Tagger, the time the photon beam needs to travel to the target is subtracted. With this information the particles β can be calculated [43].

3.7 Photon Monitoring System

The photon monitoring system is placed at the very back of the experiment and measures the photon flux available at the target. This value is necessary for normalization, e.g. for cross section determination. It consists of two subdetectors, the GIM to measure the total flux at low intensities and FluMo, which measures a fixed percentage of the flux at higher intensities.

GIM

The GIM (Gamma Intensity Monitor) is a lead glass block which is fully absorbing for the beam photons. The photons produce Cherenkov light in the detector, which is read out with a PMT at the end of the detector. This allows to measure the absolute flux, but only at low beam currents.

FluMo

At rates usually used for data taking the GIM is saturated due to dead time effects. Therefore the FluMo (Flux Monitor) is used for the actual monitoring of the flux during data taking. It consists of five thin scintillator plates and measures the photon flux indirectly through pair production. A small fraction of photons converts to electron-positron pairs on their way through the experiment. These electron-positron pairs can be detected by the scintillator plates. Using the GIM the fraction of the flux measured in FluMo can be determined and the absolute photon flux can be calculated.

CHAPTER 4

Analysis Framework and MC Event Generation

Most parts of analysis performed at the BGOOD experiment is based on ExPlORA[1], a C++ based extension to the ROOT framework [44]. Basic analysis steps like decoding of raw data, calibration, cluster formation and track finding are done without any physics analysis or selecting reactions. This *preanalysis* allows the user to start the analysis of a special reaction on the level of tracks and particles. A detailed explanation of the framework and preanalysis can be found in Ref. [43, 45].

The ExPlORA framework is also used for simulated data. In a first step the kinematic relations of initial and final state particles are generated. This event generation is part of this thesis and explained in chapter 4.1. In a second step energy loss and decay of the final state particles is simulated with GEANT4 [46], a Monte Carlo based tool to simulate particles passage through matter. From this position and energy deposition in the different detectors can be determined and analysed in the same way as it is done with real data.

4.1 Event Generator

A correct description of a reaction in simulation is essential to every analysis. To achieve this, not only the modelling of the final states particles path through the experiment is necessary, but already the initial state, the incoming photon and especially the target nucleon has to modelled correctly. When working with a deuterium target, as it is done in this thesis, the Fermi motion of the nucleons has to be taken into account. To include this, a new event generator was implemented during this thesis.

The new event generator is based on an existing version and reuses the communication structure with the ExPLORA frame work, which will then take care of the decay and the passage through the experiment. The event generator receives different parameters as input, the user can choose from a variety of reaction channels and three different target types, either hydrogen, incoherent production off the deuteron or coherent production off the deuteron. When hydrogen or coherent deuteron is chosen, the reaction happens on a proton or deuteron at rest respectively, in case of incoherent production of the deuteron, the reaction happens on either the proton, or the neutron in the deuteron nucleus, the other acting as spectator. In both cases, the target particle is not at rest, but the nucleons follow a Fermi motion. This is described in Chapter 4.2.

The event generator recognizes initial and final state particles from the given reaction name and

---

[1] **Ex**tended **Pl**uggable **O**bjectoriented **R**OOTified **A**nalysis

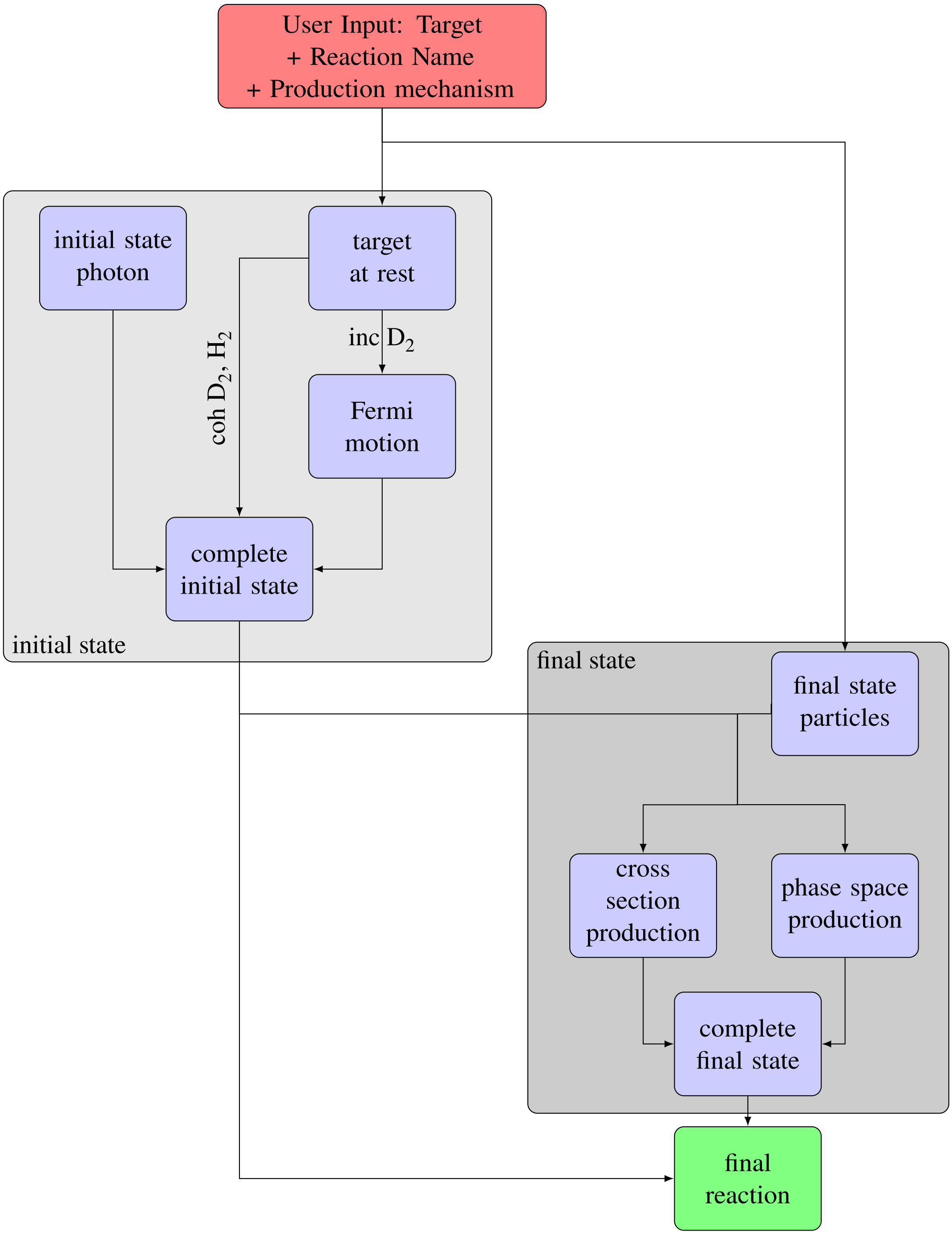

Figure 4.1: Schematic scetch of event generation. The user input is used to decide on the target type, together with the initial state photon this forms the complete initial state. The initial state energy is used to determine the final state particles momentum and direction using either phase space or cross section production. The complete reaction contains the informations from both the initial and final state.

provides them with their respective properties mass and width. Depending on the reaction the production threshold energy is calculated and a random initial state photon energy is created, following a bremsstrahlung spectrum which ranges from threshold to electron beam energy. These limits can be adjusted if a smaller energy range is desired for the initial state photons. The photon is always created with a direction exactly in z-direction. Depending on the setting, the final state particles momentum and direction is determined in different ways. Either a cross section is given, or a phase space distribution is used (Chapter 4.3).

The resulting four momenta of initial and final state particles are written to file and handed back to ExPlORA. Fig. 4.1 gives an overview of the different steps from user input over creation of the initial state and the calculation of the final state to the complete reaction.

4.2 Generating Fermi Motion

When an incoherent reaction is to be simulated on a deuterium target, the internal movement of the nucleons has to be taken into consideration. This can be understood when looking at the structure of the deuteron, the deuterium nucleus. It is a bound system of a proton and neutron. The binding energy is 2.225 MeV [47], which is relatively small compared to the nucleons masses of 938.27 MeV [47] and 939.57 MeV [47] for proton and neutron respectively. The binding energy is the amount of energy that is necessary to remove a nucleon from the bound system. Or in other words it limits the possible kinetic energy that a bound nucleon can have. A simple estimation of the momentum of a nucleon in the deuteron can be made:

$$E_{\text{kin}} = \frac{p^2}{2m} \tag{4.1}$$

$$p = \sqrt{2mE_{\text{kin}}} \tag{4.2}$$

With the mass of the deuteron of $m = 1\,875.61\,\text{MeV}$ [47] and $E_{\text{kin}} = 2.225\,\text{MeV}$ the momentum can be approximated to 90 MeV. In reality this is of course not a fixed value, but a distribution. There are different models that describe this momentum distribution of the nucleons inside the deuteron, often called Fermi motion. Here either the Paris-model [48] or the Bonn-model [49] can be chosen. Both distributions are shown in Fig. 4.2.

To correctly model the deuteron, the Fermi motion and the binding of the two nucleons has to be taken into account. Nucleons in a bound system are not necessarily on mass shell. Since the binding energy is very small compared to the nucleons masses, this difference must be small on average and will be neglected here. The effect of Fermi motion however is not negligible. To simulate Fermi motion, a random value following one of the model distributions shown in Fig. 4.2 is added to the target at rest with a random uniform direction. This additional momentum will increase or decrease the total energy of the initial state, depending on the relative direction to the incoming photon, resulting in a smearing of the reaction threshold. On a target at rest, a fixed photon energy is necessary to have enough energy for a reaction to happen. In case of deuterium this additional momentum will allow the reaction to happen at lower photon energies. Therefore the reaction threshold is recalculated for every event. The effect can be seen in Fig. 4.3. The spectrum for a target at rest starts with a sharp line and decreases with $1/E_\gamma$ following the bremsstrahlung spectrum. The spectrum where Fermi motion was taken into account shows a smearing around the sharp threshold of the target at rest. While it is

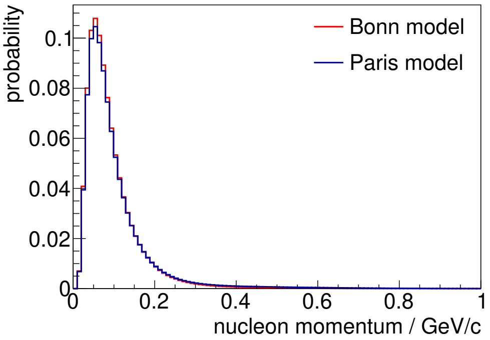

Figure 4.2: Probability distribution of the nucleon momentum inside the deuteron.Two different models are shown, in red the Bonn model [49] and in blue the Paris model [48].

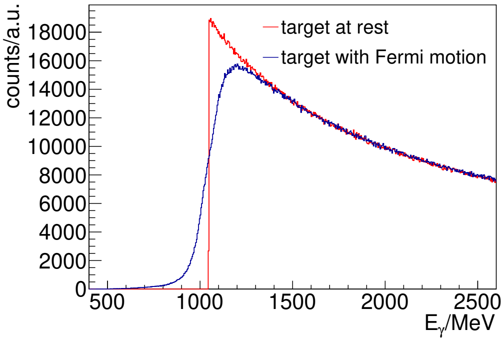

Figure 4.3: Simulated photon energy spectrum from threshold to 2 600 MeV for the reaction $\gamma n \rightarrow K^0\Sigma^0$ for a target at rest (red) and a target where Fermi motion is taken into account (blue).

possible to produce the reaction at lower photon energies the integral remains the same, resulting in lower counts at higher energies.

4.3 Production Methods

There are different ways to generate momentum and direction of the final state particles. Here cross section and phase space production are used. The former follows a given cross section distribution, the latter produces random values in the available phase space. Both methods provide a full description of the final state.

Cross section production

If a reaction is already well known, and its cross section is measured, it is possible to determine the four-vectors of the final state particles from this cross section. The cross section is provided as a function of centre-of-mass energy E_{CM} and meson angle θ_{CM}. At the time of this writing this method is only implemented for final states with one meson. If the final state contains more than one meson phase space production should be preferred.

To determine the four-vector of the meson, the $1/E_\gamma$ bremsstrahlung spectrum is boosted into the centre-of-mass system and convoluted with the given energy distribution. A random value is chosen from the resulting spectrum. From this initial state energy and the meson mass, the amplitude of the meson momentum can be determined. For the direction the angle θ_{CM} is randomly chosen from the given θ_{CM} distribution, the angle ϕ is a random value of a uniform distribution. In the centre-of-mass system the baryon four-vector is the negative meson four-vector.

If necessary beam asymmetry *BA* and polarization *PL* can be included, in this case the cross section becomes $\frac{d\sigma(E,\theta)_{pol\pm}}{d\Omega} = \frac{d\sigma(E,\theta)}{d\Omega}(1 \pm BA \cdot PL \cdot sin(2\phi))$.

Phase space production

Since often a cross section is not known it is necessary to find another way to generate the energy and angle distribution of the final state particles. This can be done with phase space production. ROOT provides the class *TGenPhaseSpace* which generates momentum distributions for n-body events from phase space. Phase space is limited from the total initial state energy and the final state particles masses, the resulting energy difference is randomly distributed among the final state particles obeying energy and momentum conservation laws. This option is advantageous if a cross section is not known, or it is undesirable to use it, or the final state consists of more than two particles. Since this thesis aims to measure an unknown cross section, in the following only the phase space production will be used.

CHAPTER 5

$\gamma n(p) \rightarrow K_S^0\Sigma(p)$ event selection

This chapter describes the reconstruction of the reaction $\gamma n \longrightarrow K_S^0\Sigma^0$ and methods to suppress and remove background. The final extraction of the signal yield will be explained in chapter 6.

The K_S^0 is reconstructed from its decay $K_S^0 \rightarrow 2\pi^0 \rightarrow (\gamma\gamma)(\gamma\gamma)$ which is ideal to make use of the almost 4π coverage for photon reconstruction through the BGO calorimeter (Chapter 5.1). The Σ^0 always decays to $\Lambda\gamma$, identification of the photon from this decay is a helpful tool to suppress background, see chapter 5.2. The dominant decay channel for the Λ is to $p\pi^-$ with 63.9% [47] branching ratio. This results in five photons and two charged particles in total. The photons are detected in the central calorimeter only, while the charged particles are detected in all detectors of the experiment. The full identification of the charged particle is only possible in the forward spectrometer. As many charged particles are observed also in the central or intermediate detectors, the reconstruction of these particles will be limited to their trajectory. This is described in more detail in chapter 5.3.

As a free neutron target does not exist, the data for this thesis were taken on a deuterium target. This results in background from the proton as well. To remove this, the same analysis is performed on hydrogen data and the resulting spectrum is subtracted from the deuterium data. Chapter 5.4 describes this in more detail. Both data sets used an ELSA electron beam of 2.9 GeV and an 11 cm long target. Hardware trigger and beam conditions were also identical for both data taking periods. The integrated photon flux from threshold to a beam energy of 2 600 MeV was $6.39 \cdot 10^{12}$ for deuterium and $5.78 \cdot 10^{12}$ for hydrogen.

5.1 K^0 reconstruction

In this thesis the K_S^0 is reconstructed not from its dominant decay to $\pi^+\pi^-$ (69.20% BR [47]), but from $2\pi^0$ (30.69% BR [47]). This channel was chosen due to the very good photon detection efficiency over a large angular range. The photons from the $2\pi^0$ decay are observed in the BGO calorimeter.

When a photon enters a BGO crystal an electromagnetic shower is created by pair-production and bremsstrahlung. This shower usually spreads over several crystals. The particle's position is determined by a weighted mean of the deposited energy position. This allows for a better resolution than the width of a single crystal.

In contrast, heavy charged particles such as $\pi^\pm$ or protons loose their energy via Bethe-Bloch ionisation and deposit energy in only one or two adjacent crystals. Distinguishing charged particles and photons by this multiplicity is difficult however, since there is no hard discrimination. To distinguish

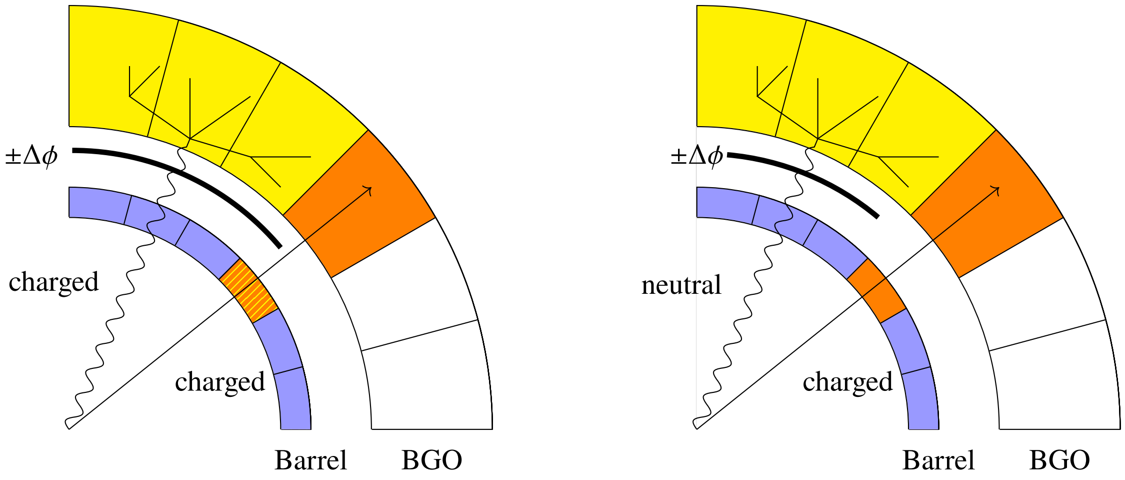

(a) $\Delta\phi$ is too large. The photon track is associated with the signal in the Barrel and assigned charge.

(b) $\Delta\phi$ is correct. The signal in the Barrel is only associated to the track which produced it. The photon track is not assigned charge.

Figure 5.1: Simplified slice view of the central detector with BGO and Barrel. Shown are the trajectories of a charged particle (straight line) and a photon (wavy line). The detector signals associated to each track are coloured orange and yellow respectively. The sketch is not to scale.

between charged and neutral tracks instead the information from the Barrel is used.

Trajectories of particles in the BGO calorimeter are assumed to originate at the target centre. If such a trajectory can be associated with a hit in the Barrel it is identified as a charged track. A trajectory is associated with a hit in the Barrel, if it is close enough in ϕ, the maximum allowed difference is called $\Delta\phi$.

A large number of particles as in this reaction increases the probability of two or more particles being close in ϕ, which may result in a photon trajectory being falsely associated with a Barrel hit and considered as a charged particle. Fig. 5.1 illustrates the effect of different $\Delta\phi$. Shown is a charged particle's trajectory, giving a signal in the Barrel and the BGO, and a photon, producing a shower in the BGO. Also shown is the angular range $\Delta\phi$ within which a Barrel hit would be associated to the photon track. In Fig. 5.1(a) $\Delta\phi$ is too large, the signal in the Barrel that was caused by the charged particle can be associated with the cluster in the BGO that was caused by a photon, falsely assigning the photon track charge. In Fig. 5.1(b) $\Delta\phi$ is chosen better, the signal in the Barrel is not associated with the Photon cluster and it is correctly assigned no charge.

In simulation the effect of the size of $\Delta\phi$ in which BGO and Barrel signals are combined can be studied in more detail. Figure 5.2 shows the number of charged and neutral tracks reconstructed in BGO and Barrel for different $\Delta\phi$ when requesting at least seven particles in the BGO. From the simulated reaction $\gamma n \to K^0\Sigma^0$ a peak at five neutral and two charged particles would be expected[1].

In Fig 5.2(b) it can be seen that for the default value of $\Delta\phi = 20°$ there are as many events with only four neutral particles as there are with five. Fig 5.2(a) shows, that for 20° there are many events with three or more charged tracks. With decreasing $\Delta\phi$ the number of neutral particles increases and the

---

[1] It is of course possible, that not all reaction particles are observed in the BGO, but instead go in more forward direction. However, for this study it was requested, that all particles can be observed in the angular range covered by the BGO.

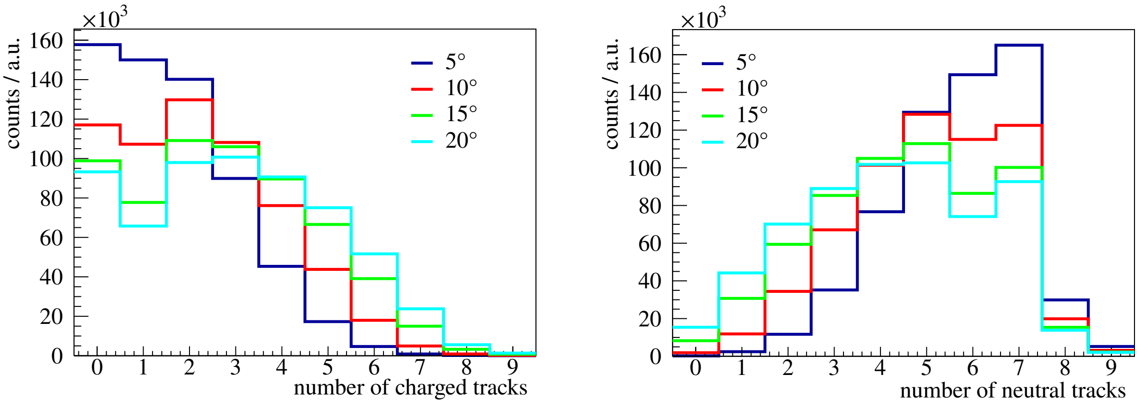

(a) Number of charged tracks in the central detector for different $\Delta\phi$ angles between BGO and Barrel signal.

(b) Number of neutral tracks in the central detector for different $\Delta\phi$ angles between BGO and Barrel signal.

Figure 5.2: Charged and neutral tracks in the central detector for different $\Delta\phi$ angles between BGO and Barrel signal determined from simulated $\gamma n \to K^0\Sigma^0$events. Expected are five neutral and two charged tracks. The optimum lies at $\Delta\phi = 10°$.

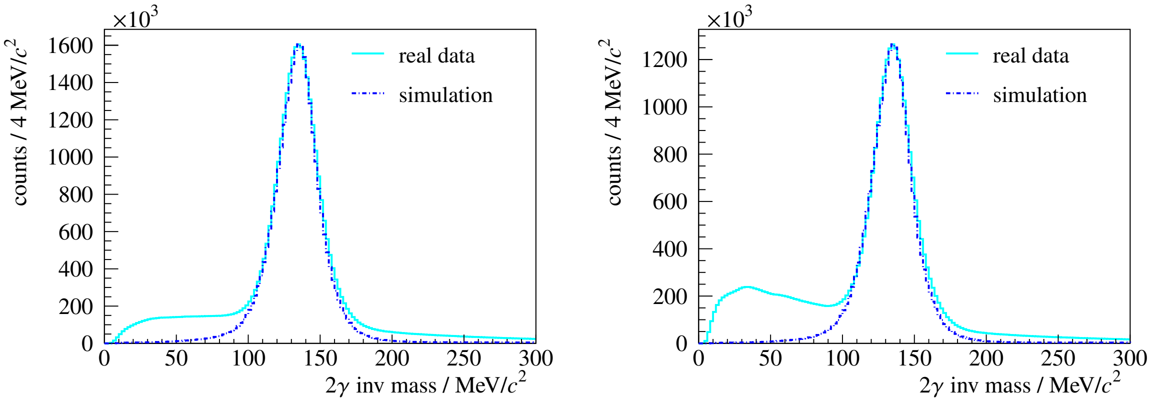

(a) 2γ invariant mass spectrum in real data and simulation using a deuterium target.

(b) 2γ invariant mass spectrum in real data and simulation using a hydrogen target.

Figure 5.3: 2γ invariant mass spectrum in real data and simulation for a deuterium and hydrogen target. Requested are exactly two γ in the BGO. The simulated channel is $\gamma p \to \pi^0 p$, this data is scaled to fit the height of the real data. In both cases the 1σ resolution is approximately 15 MeV.

number of charged particles decreases. At $\Delta\phi = 5°$ however, more neutral and less charged tracks then expected are observed. At very low $\Delta\phi$ charged particles are not associated with the corresponding track in the Barrel anymore and considered neutral. The optimum lies around $\Delta\phi = 10°$, which corresponds to approximately one crystal, and increases the number of reconstructed events by about 20% compared to the default value. The peak at zero charged and seven neutral particles comes from the neutral Λ decay that is not used in this thesis.

The photons observed in the BGO calorimeter are then combined to pairs. If they are the decay particles of a π^0, a peak at the π^0 mass is expected in the 2γ invariant mass spectrum. This peaks width

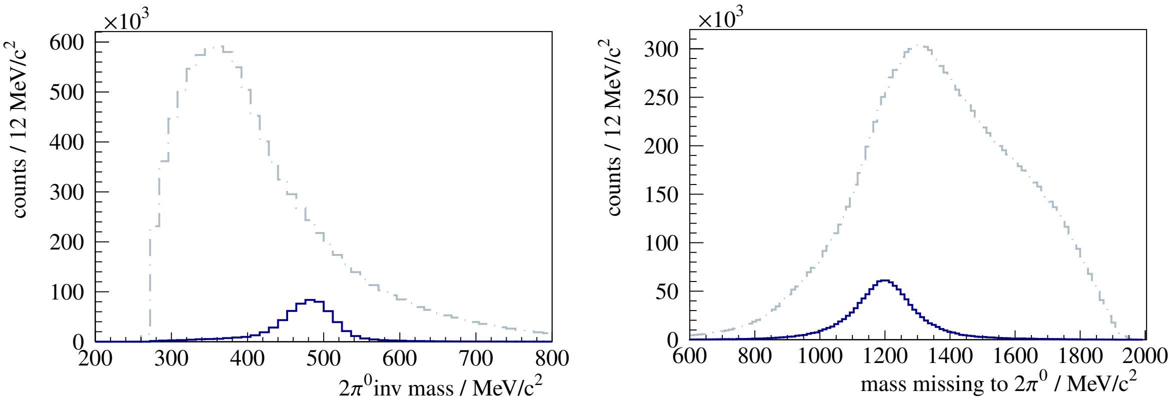

(a) $2\pi^0$ invariant mass spectrum after selecting four photons in the BGO and combining them to two π^0. Additionally the missing mass to the $2\pi^0$ system is required to be consistent with the Σ^0 mass between 1 150 to 1 250 MeV.

(b) Spectrum of the mass missing to the $2\pi^0$ reconstructed in the BGO. The $2\pi^0$ invariant mass is required to be consistent with the K^0_S mass between 430 to 530 MeV.

Figure 5.4: $2\pi^0$ invariant mass and mass missing to the $2\pi^0$ (grey dashed line). In both figures the signal expected from simulated $\gamma n \rightarrow K^0\Sigma^0$ is included in an arbitrary scale (blue line).

and position must agree in simulation and real data. Fig. 5.3 shows the 2γ invariant mass spectrum for deuterium and hydrogen data in real data and simulation. To get a clean spectrum exactly two photons were required in the BGO and the reaction $\gamma p \rightarrow \pi^0 p$ was simulated. This has no effect on the π^0 mass peak but has the advantage that the combinatorial background is reduced compared to four or five photons that one would observe in a simulation of $\gamma n \rightarrow K^0\Sigma^0$ and the analysis can be performed on both targets. Fig. 5.3(a) and 5.3(b) both show a good agreement between simulation and real data. Here the simulated data is scaled to fit the height of the real data.

Every pair of photons with an invariant mass within ±30 MeV of the nominal π^0 mass is considered a π^0 candidate. This selection corresponds to approximately $\pm 2\sigma$ of the 2γ invariant mass peak. In the next step two π^0 candidates are combined and the invariant mass of the $2\pi^0$ system is determined. It was ensured, four different photons were used to form the two π^0 candidates and no photon was used twice. Additionally the missing mass to the $2\pi^0$ system is required to be around the Σ^0 mass between 1 150 to 1 250 MeV. The missing mass is calculated according to Eqn 5.1

$$M_{\text{missing}} = \sqrt{(P_{\text{initial state}} - P_{2\pi^0})^2}, \tag{5.1}$$

with $P_{\text{initial state}}$ and $P_{2\pi^0}$ being the four-vectors of the initial state and the $2\pi^0$ system respectively.

Fig. 5.4(a) shows the $2\pi^0$ invariant mass spectrum after the selection of the missing mass. At the K^0_S mass of 497.6 MeV a peak is expected but not observed. Fig. 5.4(b) shows the mass missing to the $2\pi^0$ system. Here the invariant mass of the $2\pi^0$ is required to be consistent with the K^0_S mass between 430 to 530 MeV. A peak at the Σ^0 mass is expected, but also not observed. Since this selection is obviously not sufficient to observe a K^0_S peak in the $2\pi^0$ invariant mass spectrum, or a Σ^0 peak in the missing mass, further selection criteria and methods to suppress background have to be applied.

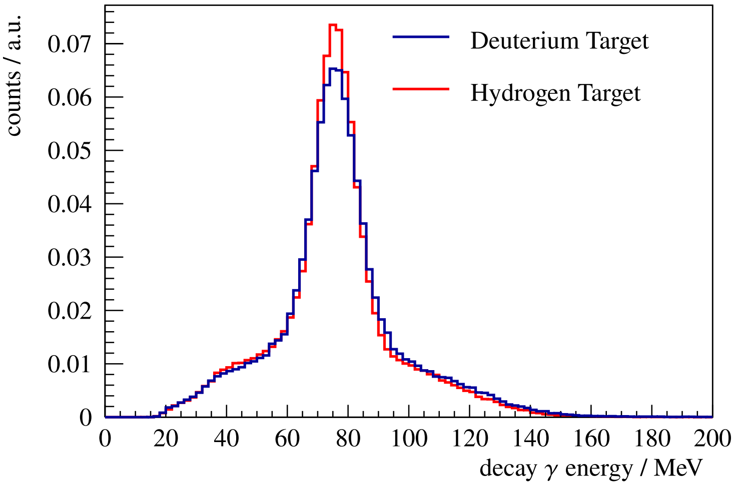

Figure 5.5: Simulated energy spectrum of the Σ^0 decay photon off deuterium and hydrogen. The integral of both spectra is normalized to 1.

5.2 Identifying the Σ^0 decay

A strong tool to enhance the signal is the very characteristic decay of the Σ^0 to $\Lambda\gamma$ with a branching ratio of 100%. In the Σ^0 rest frame the photon has a well defined Energy of 74.42 MeV:

$$\begin{aligned} m_\Sigma^2 &= (E_\Lambda + E_\gamma)^2 - (\vec{p}_\Lambda + \vec{p}_\gamma)^2 && (5.2)\\ &= m_\Lambda^2 + 2m_\Sigma E_\gamma && (5.3)\\ \Rightarrow E_\gamma &= \frac{m_\Sigma^2 - m_\Lambda^2}{2m_\Sigma} && (5.4)\\ &= \frac{(1\,192.6\,\text{MeV})^2 - (1\,115.7\,\text{MeV})^2}{2\cdot 1\,192.6\,\text{MeV}} = 74.42\,\text{MeV} && (5.5) \end{aligned}$$

In the following this photon is called *decay photon* to distinguish it from other photons. To identify the decay photon the fifth photon that was observed in the BGO but not used to form the $2\pi^0$ system is boosted in the Σ^0 rest-frame. Since the Σ^0 is not measured, it is identified as the *missing four momentum* to the $2\pi^0$ system.

$$P_\Sigma = P_{\text{initial state}} - P_{2\pi^0} \tag{5.6}$$

The initial state contains the beam photon and the target. In case of deuterium the target nucleon is not at rest but moves according to Fermi motion. Since it is impossible to know the momentum of the target nucleon it is assumed at rest. This introduces an error in the *missing four momentum* and thus in the energy of the decay photon candidates. As Fermi motion is uniform in all directions this will not cause a shift, but a broadening of the energy spectrum of the decay photon candidates.

To test this, the reaction $\gamma p \rightarrow K^+\Sigma^0$ is ideally suited. The reaction can happen on a deuterium

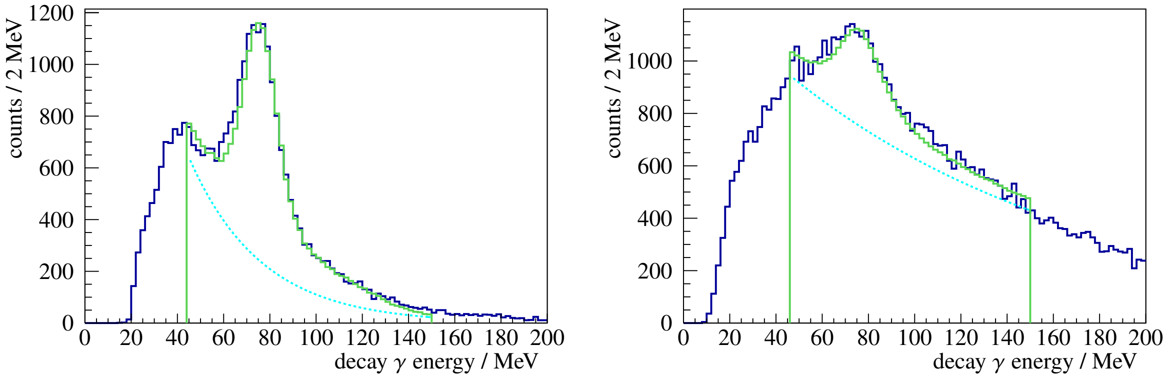

(a) Energy spectrum of decay photon candidates in the Σ^0 rest frame which is calculated from the four momentum missing to a reconstructed K^+ (dark blue line). The visible peak is compared to simulated $\gamma p \longrightarrow K^+\Sigma^0$ (green line), the background is approximated with an exponential function (dashed light blue line) and added to the the simulated spectrum which is scaled to describe the real data.

(b) Energy spectrum of decay photon candidates in the Σ^0 rest frame calculated from the four momentum missing to a reconstructed K^0 (dark blue line). The visible peak is compared to simulated $\gamma n \longrightarrow K^0\Sigma^0$ (green line), the background is approximated with an exponential function (dashed light blue line) and added to the the simulated spectrum which is scaled to describe the real data.

Figure 5.6: Reconstructed energy spectrum of decay photon candidates in the rest frame of the Σ^0. The Σ^0 is reconstructed as the missing four momentum to either a K^+ (Fig. 5.6(a)) or a K^0_S (Fig. 5.6(b)). In both cases the background is approximated with an exponential function and added to the simulated spectrum which is scaled to fit the real data.

target as well as on a hydrogen target, the K^+ can be easily identified in the Forward Spectrometer and it has less background than $\gamma n \longrightarrow K^0\Sigma^0$. In the determination of the decay photon energy the $2\pi^0$ system is simply replaced with the K^+. Fig. 5.5 shows the reconstructed energy spectrum of the decay photon from simulated $\gamma p \longrightarrow K^+\Sigma^0$ on a deuterium and hydrogen target. To compare the shape of the peak the integral of both spectra is normalised to one. As expected the spectrum off a deuterium target is slightly broader than the one off a hydrogen target, while both peak at the expected energy.

In a second step the peak generated in simulation is compared to real data. Again the reaction $\gamma p \longrightarrow K^+\Sigma^0$ is used. Fig. 5.6(a) shows the comparison of the simulated spectrum with real data where a K^+ was identified in the Forward Spectrometer. The background underneath the peak is approximated with an exponential function and added to the simulated spectrum. Position and width of the peak agree very well between real and simulated data.

Now this is applied to the reaction $\gamma n \longrightarrow K^0\Sigma^0$. Fig. 5.6(b) shows the reconstructed energy spectrum of the decay photon candidates in real data and simulated $\gamma n \longrightarrow K^0\Sigma^0$. The decay photon peak is a lot less pronounced than it was for the test reaction $\gamma p \longrightarrow K^+\Sigma^0$. To make it visible only events with a $2\pi^0$ invariant mass around the K^0_S mass between 430 to 530 MeV are plotted. Again the background is approximated with an exponential function and added to simulation. Peak position and width are consistent.

Photons within ±21 MeV of 74.42 MeV, which corresponds to $\pm 3\sigma$, are considered as decay photons. Using only such events drastically reduces the background. Fig. 5.7 shows the $2\pi^0$ invariant mass spectrum and the missing mass to the π^0 after selecting the decay photon candidates. An enhancement at the K^0_S mass is now visible on top of the background in Fig. 5.7(a) while in the missing

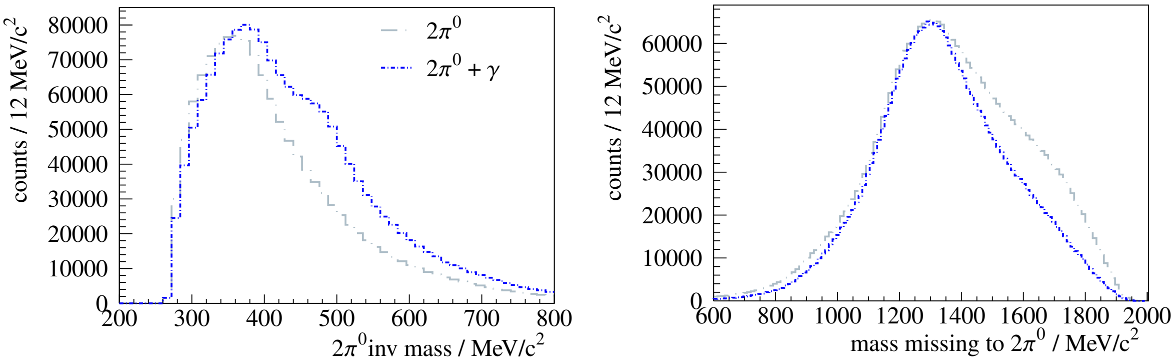

(a) $2\pi^0$ invariant mass spectrum after reconstructing two π^0 in the BGO and selecting decay photon candidates (blue dotted line). Additionally the same spectrum before selecting the decay photon candidates (Fig. 5.4(a)) is shown for comparison. To approximately match the height it is scaled by a factor 0.13. The missing mass to the $2\pi^0$ system is required to be consistent with the Σ^0 mass between 1 150 to 1 250 MeV for both spectra.

(b) Spectrum of the mass missing to the $2\pi^0$ reconstructed in the BGO after selecting decay photon candidates (blue dotted line). For comparison the spectrum before selecting the decay photon candidates shown in Fig. 5.4(b) is plotted additionally. To match the height it is scale by a factor 0.22. The $2\pi^0$ invariant mass is required to be consistent with the K_S^0 mass between 430 to 530 MeV for both spectra.

Figure 5.7: $2\pi^0$ invariant mass and mass missing to the $2\pi^0$ after selecting decay photon candidates.

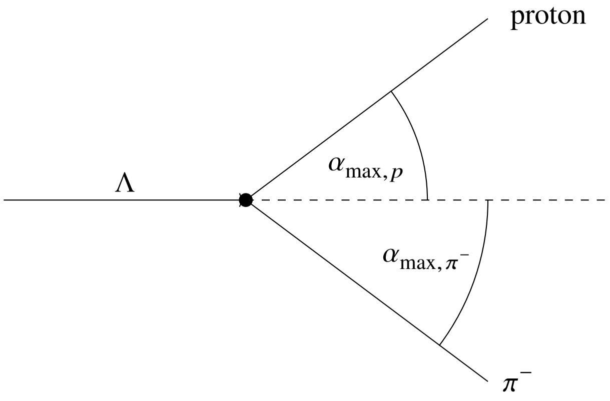

Figure 5.8: Sketch of Λ decaying to p and π^-. $\alpha_{\max}$ is the maximum possible angle that can be measured between the Λ and its respective decay particles in the laboratory frame.

mass spectrum in Fig. 5.7(b) no signal can be observed. As the enhancement is still quite small and difficult to separate from the background the identification of the Λ decay particles is applied as a third selection cut.

5.3 Identification of Λ decay particles

The dominant decay channel of the Λ is $\Lambda \rightarrow p\pi^-$ with a branching ratio of 63.9%. These particles can be measured in all detector regions, however, a full identification is only possible in the forward

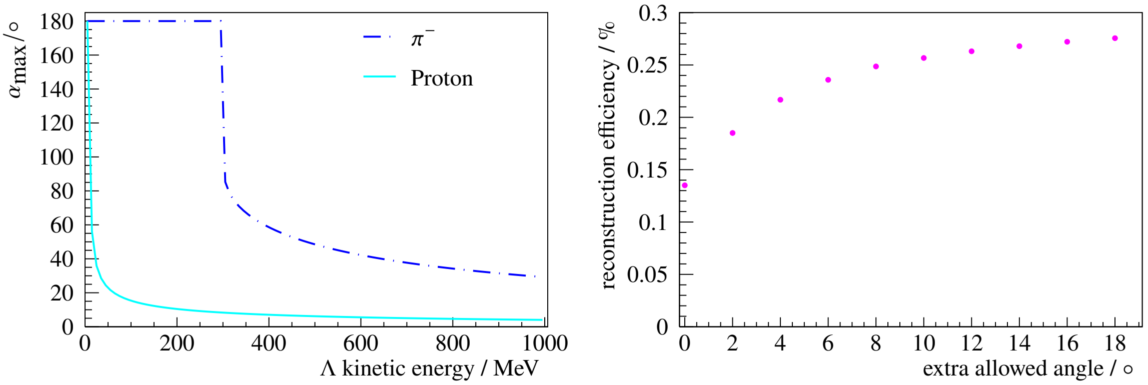

(a) Maximum possible angle $\alpha_{\max}$ between the Λ and its decay particles, either the proton or the π^-, as a function of Λ kinetic energy.

(b) Total reconstruction efficiency as a function of an angle additionally allowed to $\alpha_{\max}$.

Figure 5.9: Maximum possible angle $\alpha_{\max}$ and reconstruction efficiency as a function of an angle additionally allowed to $\alpha_{\max}$.

spectrometer. Therefore the measurement will be limited to charge and direction.

To ensure the detected charged particles are consistent with the decay particles of the Λ their direction must lie in the kinematically allowed region with respect to the Λ. This region is determined as the angle between the charged particle and the Λ as a function of the kinetic energy of the Λ in the laboratory system as depicted in Fig. 5.8. Assuming a Λ at rest the decay particles can move in any direction, the maximum angle $\alpha_{\max}$ is 180°. With increasing kinetic energy the decay particles are boosted more and more in the direction of the Λ and the maximum possible angle between the Λ and the charged particle that can be measured in the laboratory system decreases. This maximum possible angle is depicted in Fig. 5.9(a). Due to its higher mass the boost affects the proton stronger and the maximum possible angle drops rapidly. The relatively light π^- can reach 180° up to kinetic energies of the Λ of around 300 MeV before the maximum possible angle also drops.

To account for angular resolution an extra 10° is allowed. Fig. 5.9(b) shows the effect of different values of extra allowed angles on the total reconstruction efficiency, determined from simulated $\gamma n \rightarrow K^0\Sigma^0$ by dividing all reconstructed events by the number of generated events. The efficiency increases with increasing angle. While the curve increases quickly at low angles it flattens when going to higher angles. A larger angle will not only increase the number of desired events, but will also allow more background events to pass the selection. An extra 10° almost doubles the reconstruction efficiency without picking up too much background.

To identify the decay particles of the Λ exactly two charged particles are required. One has to fulfil the kinematic constraints of a proton, the other the constraints of a π^- as depicted in Fig. 5.9. Fig. 5.10(a) shows the effect of this selection on the $2\pi^0$ invariant mass spectrum. At the expected position of the K_S^0 a peak is now clearly visible. The $2\pi^0$ invariant mass spectra after the previous selection cuts are also plotted for comparison. Fig. 5.10(b) shows the corresponding missing mass spectra. Here still no peak is visible at the Σ^0 mass. As it is not possible to identify a signal in the missing mass spectrum, in the following the missing mass will always be selected to be between 1 150 to 1 250 MeV and the $2\pi^0$ invariant mass spectrum will be used to extract the yield of the reaction

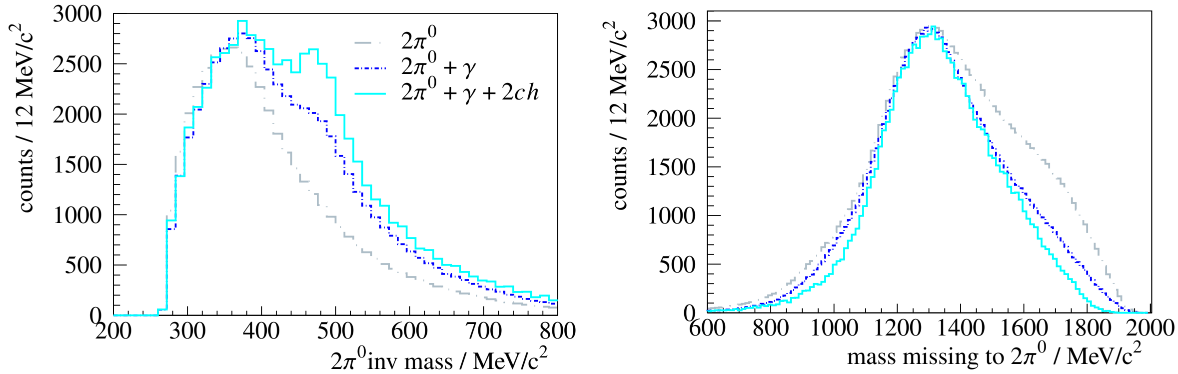

(a) $2\pi^0$ invariant mass spectrum after reconstructing two π^0, selecting the decay photon and identifying the Λ decay particles (light blue). For comparison the spectra after only reconstructing two π^0 (grey) and selecting the decay photon (dark blue) are also shown again. They are scaled by a factor of 0.0045 and 0.035 respectively to approximately match the height. The missing mass to the $2\pi^0$ system is required to be consistent with the Σ^0 mass between 1 150 to 1 250 MeV for all three spectra.

(b) Spectrum of the mass missing to the $2\pi^0$ system reconstructed in the BGO after selecting decay photon candidates and identifying the Λ decay particles (light blue). For comparison the spectra after only reconstructing two π^0 (grey) and selecting the decay photon (dark blue) are also shown again. They are scaled by a factor of 0.0097 and 0.045 respectively to approximately match the height. The $2\pi^0$ invariant mass is required to be consistent with the K^0_S mass between 430 to 530 MeV for all three spectra.

Figure 5.10: $2\pi^0$ invariant mass and mass missing to the $2\pi^0$ after selecting decay photon candidates and identifying the Λ decay particles.

$\gamma n \longrightarrow K^0\Sigma^0$.

5.4 Subtracting hydrogen background

The previous selections already enhanced the signal and reduced background. The remaining background can be split in two contributions. The first contribution is competing reactions on the neutron with the same or a similar final state, the second, larger contribution is caused by reactions happening on the proton of the deuterium.

In a simple approach the number of events measured off the deuterium target equals the events measured off the neutron plus the events off the proton:

$$N_D = N_p + N_n$$

In this approach the proton contribution can be removed, for example by repeating the same analysis with data taken on a hydrogen target and subtracting them from the data taken on a deuterium target. This is of course over simplified. Data taken on a free proton target as hydrogen is not exactly the same as data taken on a quasi-free proton target as deuterium. The two main aspects that have to be regarded are Fermi motion and Final State Interactions (FSI). The latter will be discussed later.

As was already mentioned before, the nucleons inside the deuteron are not at rest, while the proton in the hydrogen is. Since the momentum of the target nucleon inside the deuterium is not known it is assumed at rest. This will not affect measured properties, but will introduce a broadening in the

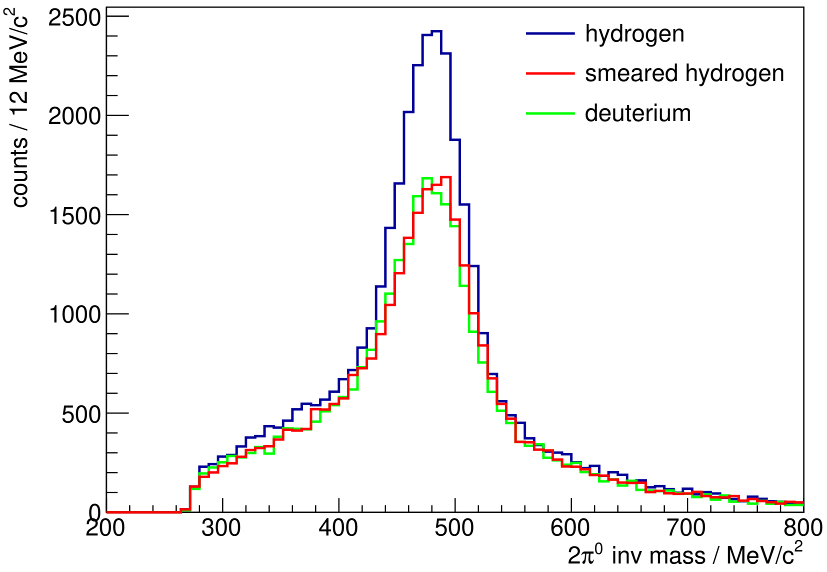

Figure 5.11: $2\pi^0$ invariant mass spectrum reconstructed from simulated $\gamma p \to K^0\Sigma^+$ off a deuterium and hydrogen target and a hydrogen target with artificial Fermi motion (smeared hydrogen).

missing mass that is calculated from equation 5.1.

As the missing mass is selected to be around the Σ^0 mass this will indirectly affect the $2\pi^0$ invariant mass spectrum. The effect can be studied in simulation. Here the reaction $\gamma p \to K^0\Sigma^+$ is used. This background reaction was chosen as it will produce a peak at the K^0_S mass which might contribute to the extracted signal yield if not subtracted correctly. Other background channels, mainly π and η production, are flat in the signal region and will not have that much impact on the signal yield.

Fig. 5.11 shows the $2\pi^0$ invariant mass spectrum for simulated $\gamma p \to K^0\Sigma^+$ off a deuterium and a hydrogen target. Also shown is the data off the hydrogen target, where the effect of Fermi motion was artificially created. This was achieved by giving the target nucleon a random momentum following the Paris model [48] momentum distribution given in Fig. 4.2 and repeating the analysis with this now "moving" target. To distinguish it from the hydrogen at rest this data is call *smeared hydrogen*. As can be seen in Fig. 5.11 the smeared hydrogen reproduces the shape of the deuterium data very well, while the hydrogen at rest is very different.

This allows now to *smear* a real hydrogen data set and to subtract it from the deuterium data. To subtract the correct number of events, the smeared hydrogen data is scaled by luminosity. Fig. 5.12 shows the scaled smeared hydrogen data together with the deuterium data and the result after subtraction. It can be seen that the proton background contribution is significant. This is expected, as the reconstruction required charged particles. The remaining background contribution after subtracting the smeared hydrogen data is much smaller now, while the signal is quite pronounced. In the next step this remaining background and the signal peak is fitted using different techniques to extract the signal yield. This is explained in chapter 6.

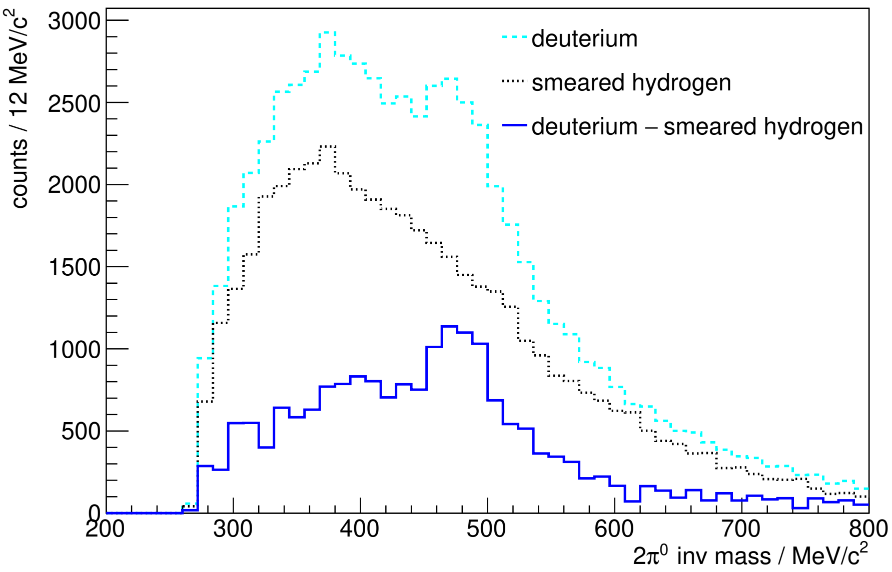

Figure 5.12: The invariant mass distribution of the $2\pi^0$ system after all selection criteria for deuterium and smeared hydrogen data. The smeared hydrogen data is scaled by luminosity and subtracted from the deuterium data. The resulting spectrum is also shown.

CHAPTER 6

Extracting the K_S^0 yield

In this chapter the K_S^0 yield is extracted by fitting to the $2\pi^0$ invariant mass spectrum . Since the aim of this thesis is to determine a differential cross section the data are split in several bins in beam energy and $\cos\theta_{\text{CM}}^K$ the cosine of the centre-of-mass angle of the K_S^0.

The maximum possible resolution in beam energy is limited by the tagger hodoscope. Its segmented structure of overlapping scintillators allows a resolution between 0.55% to 2.28% of the maximum beam energy. As statistics is very limited, larger energy bins are chosen, but their borders are such that they agree with the closest tagger bin. The data is split in nine bins with a width of approximately 100 MeV from 1 012 MeV to 1 900 MeV and two bins with an approximate width of 300 MeV and 400 MeV from 1 900 MeV to 2 195 MeV and from 2 195 MeV to 2 594 MeV respectively. The threshold of $\gamma n \longrightarrow K^0\Sigma^0$ assuming a target at rest is 1 040 MeV. As Fig. 4.3 shows the threshold is actually smeared out as the target neutron is not at rest. Therefore the lower limit of the first energy bin is starting below that value at 1 012 MeV. In $\cos\theta_{\text{CM}}^K$ four bins of $\Delta\cos\theta_{\text{CM}}^K = 0.3$ are chosen between $\cos\theta_{\text{CM}}^K = -0.7$ and $\cos\theta_{\text{CM}}^K = 0.5$.

To extract the K_S^0 yield different fitting methods are applied and compared. All methods include fitting the background. RooFit [50] is used to fit the total spectrum in each bin, the background is described either by simulating different background channels, or by using real data with relaxed selection cuts. This method is described in chapter 6.1 To get a measure of the quality of the fits different tests are performed and explained in chapter 6.2. A second method to determine the K_S^0 yield is fitting to the side bands outside the signal region and calculating the excess in the signal region as described in chapter 6.3. Finally the yield extracted with these methods from the binned data is compared to the yield determined from a larger angular range (chapter 6.4).

6.1 Fitting the data using RooFit

A useful tool to fit binned data in histograms as given here is Roots fitting library RooFit [50]. Different fitting algorithms are provided. Here a binned maximum likelihood fit is used. This has the disadvantage that the fit assumes the errors of the data set to always be $\sqrt{N}$ which is not the case here. However, the error of the fit results can be recalculated using the correct error, resulting in a correct display of the fits accuracy. Due to very limited statistics the usefulness of a χ^2 fit, which would work correctly with any error, is reduced, as the χ^2 distribution might not follow the expected behaviour. Therefore the maximum likelihood fit is more reliable. Different spectra are used

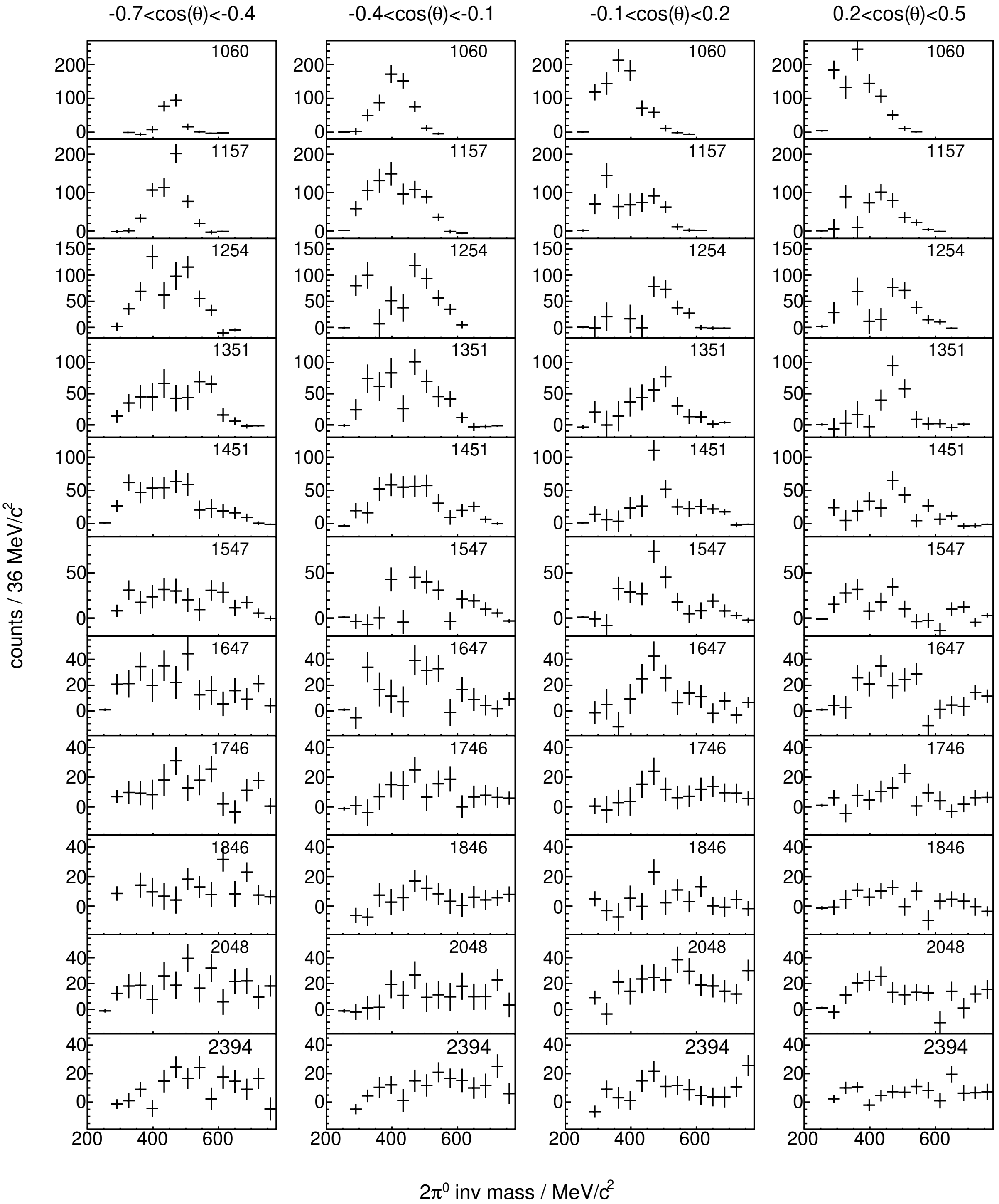

Figure 6.1: $2\pi^0$ invariant mass split in four bins in $\cos\theta^K_{\mathrm{CM}}$ and eleven bins in beam energy. Each column corresponds to the angular range labelled on top. The centre of each beam energy bin is given in the top right corner of each plot in MeV.

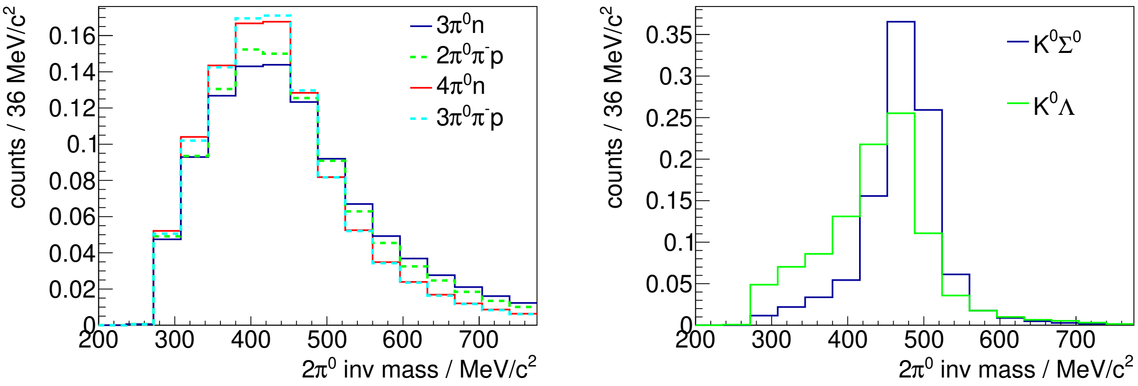

(a) $2\pi^0$ invariant mass spectrum of simulated $\gamma n \longrightarrow 3\pi^0 n$, $\gamma n \longrightarrow 2\pi^0\pi^- p$, $\gamma n \longrightarrow 4\pi^0 n$ and $\gamma n \longrightarrow 3\pi^0\pi^- p$. For comparison the integral of all shapes is normalized to one.

(b) $2\pi^0$ invariant mass spectrum of simulated $\gamma n \longrightarrow K^0\Sigma^0$ and $\gamma n \longrightarrow K^0\Lambda$. The integral of both shapes is normalized to one.

Figure 6.2: $2\pi^0$ invariant mass spectrum of different simulated background channels and the signal channel.

to describe background and signal and are scaled by the fit to describe the data. Two methods to provide these spectra for the background are used in this thesis. The first uses the shapes of several background channels determined in MC simulation from phase space (PS), the second uses real data with relaxed selection cuts (RD). In both cases the expected signal spectrum is generated from simulated $\gamma n \longrightarrow K^0\Sigma^0$.

Fig. 6.1 shows the $2\pi^0$ invariant mass spectrum of the real data in all four angular bins for all energies. Most plots have zero or negative entries left and right of the visible spectrum. The negative entries are caused by the subtraction of the hydrogen data set. Both are difficult to fit. Therefore the range that is fitted is chosen such, that it starts when the first data point is larger 1 and stops when the next data point is smaller 0. To ensure the signal region is included in the fit, the first four beam energy bins have to reach at least a $2\pi^0$ invariant mass of 500 MeV/c^2, all bins with higher beam energies have to reach at least a $2\pi^0$ invariant mass of 700 MeV/c^2.

6.1.1 Background shape described by background channels generated from phase-space (PS)

To describe the background with simulated spectra, the corresponding background channels need to be known. The dominating channels are:

- $\gamma n \longrightarrow \pi^0\pi^0\pi^0 n$
- $\gamma n \longrightarrow \pi^0\pi^0\pi^0\pi^0 n$
- $\gamma n \longrightarrow \pi^0\pi^0\pi^- p$
- $\gamma n \longrightarrow \pi^0\pi^0\pi^0\pi^- p$
- $\gamma n \longrightarrow \eta n$
- $\gamma n \longrightarrow K^0\Lambda$

Further channels may contribute, but it can be shown their contribution is negligible here. Additionally the number of fit parameters should be reduced to the smallest possible number as this increases the probability for the fit to converge.

Fig. 6.2(a) shows the shape of the $2\pi^0$ invariant mass spectrum of the MC simulated four multi-pion channels after passing the selection cuts explained in chapter 5, with the same binning as the data,

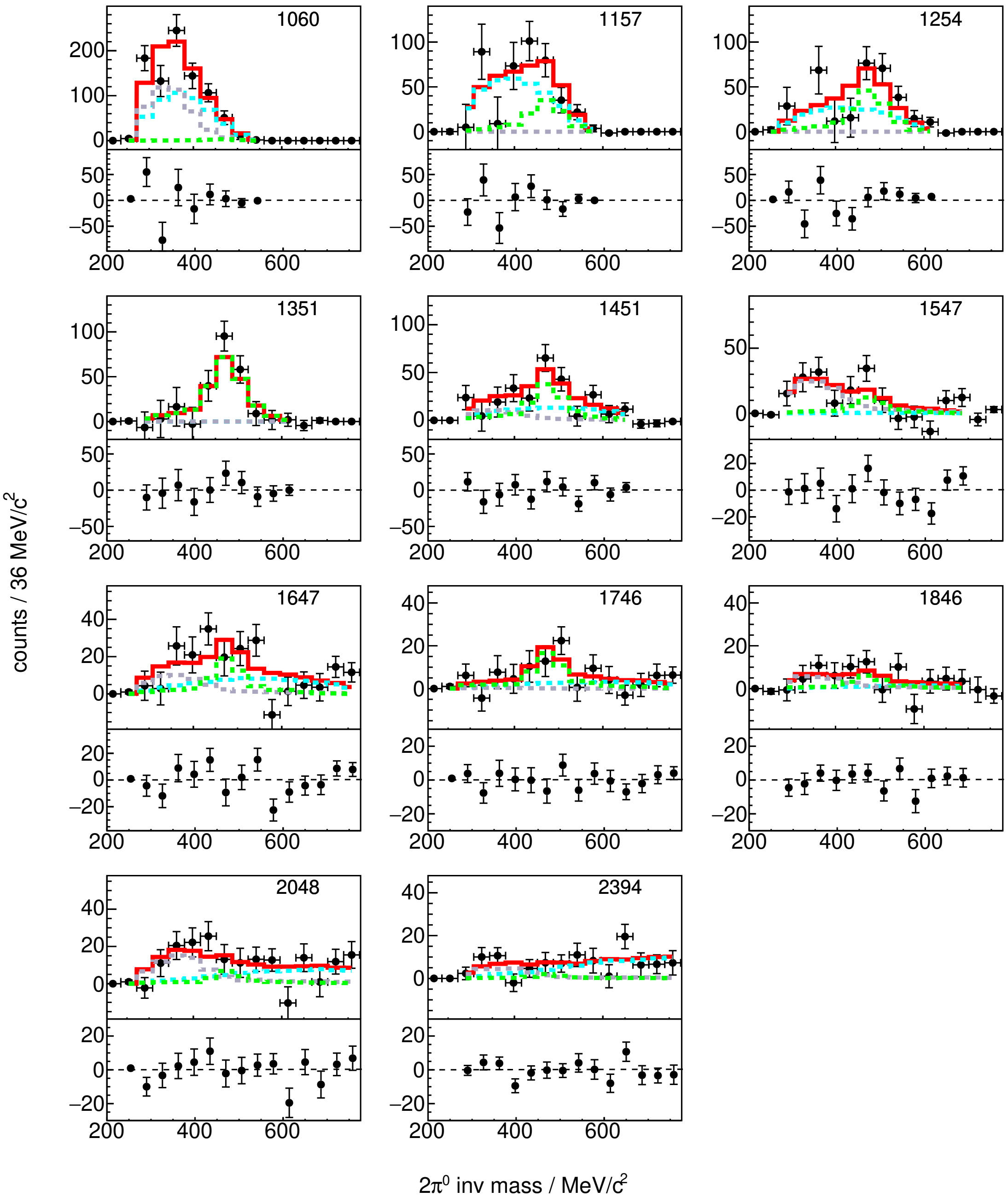

Figure 6.3: Fits for all energies in the angular range 0.2 <cos θ^K_{CM}< 0.5. The data is fitted with the expected signal spectrum $\gamma n \to K^0\Sigma^0$(green), $\gamma n \to \eta n$ (grey) and $\gamma n \to \pi^0\pi^0\pi^0 n$ (light blue). The full fit is shown in red. Underneath each fit the residuals are shown. The centre of each beam energy bin is given in the top right corner of each plot in MeV.

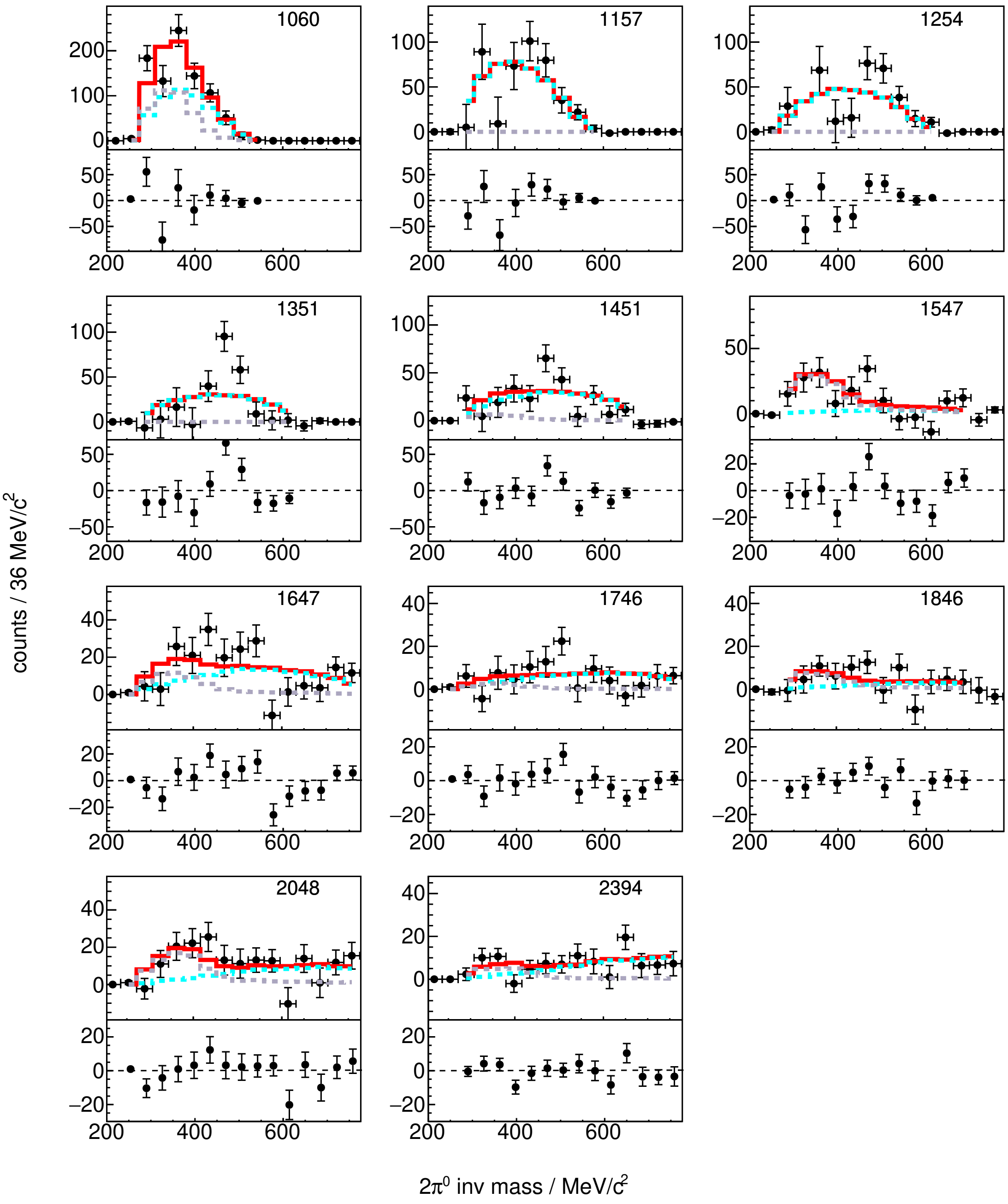

Figure 6.4: Fits for all energies in the angular range 0.2 $<\cos\theta^K_{\mathrm{CM}}< 0.5$. The data is fitted with the background channels only, namely $\gamma n \rightarrow \eta n$ (grey) and $\gamma n \rightarrow \pi^0\pi^0\pi^0 n$ (light blue). The full fit is shown in red. Underneath each fit the residuals are shown. The centre of each beam energy bin is given in the top right corner of each plot in MeV.

integrated over all four angular bins and all energies. To compare the shape the integral of all spectra is normalized to one. It is visible, that the shapes are very similar. Passing all four spectra to the fit will not provide new information. Within the available statistics it is not possible for the fit to differentiate between them. In contrast it would make converging of the fit more difficult, as the number of fit parameters is increased. To perform the fit the channel $\gamma n \rightarrow \pi^0\pi^0\pi^0 n$ is chosen as a representative for all multi-pion channels.

For the same reason the channel $\gamma n \rightarrow K^0\Lambda$ will not be included in the fit. Fig. 6.2(b) shows the shape of the $2\pi^0$ invariant mass spectrum of MC simulated $\gamma n \rightarrow K^0\Lambda$ and $\gamma n \rightarrow K^0\Sigma^0$ after passing the selection cuts explained in chapter 5. The integral of both spectra is normalized to one. The very similar shape makes it difficult to differentiate between them. However, the previous selection cuts suppressed the contribution from $\gamma n \rightarrow K^0\Lambda$ in the real data set. It will be determined in a later step. For the fits performed here, only $\gamma n \rightarrow K^0\Sigma^0$ is used to describe the expected signal spectrum. As a second background channel the MC simulated spectrum of $\gamma n \rightarrow \eta n$ is included in the fits.

Fig. 6.3 shows the fits in the angular bin $0.2 < \cos\theta_{\mathrm{CM}}^{K} < 0.5$ for all energies. If not stated otherwise in the following always this angular range is shown. Plots for all other angular ranges can be found in the appendix (Fig. A.1 to A.6). Underneath each plot the residual of the fit is shown. More detailed tests of the fit quality will be performed, but at first glance the fits appear to describe the data well. This is supported by the residuals. They are centred around 0 and show no unexpected structures. The signal yield is determined as the integral of the fitted $\gamma n \rightarrow K^0\Sigma^0$ spectrum. It is shown in Fig. 6.7.

To exclude the possibility that the data could be described as well with the background channels only, the fits are repeated with only these spectra. Fig. 6.4 shows the fits in the angular bin $0.2 < \cos\theta_{\mathrm{CM}}^{K} < 0.5$ for all energies where the expected signal spectrum was excluded from the fit. In direct comparison the fits without the expected signal spectrum appear to describe the data not as good as the ones including the expected signal spectrum. In some bins a peak structure is visible in the residuals.

6.1.2 Background shape described by real data (RD)

The second method to describe the remaining background is using real data with relaxed cuts. The shape of the background does not change much with the different selection cuts applied to enhance the signal, as was already shown in Fig. 5.10(a) where the $2\pi^0$ invariant mass spectrum was plotted after the different selection cuts. This can now be used to get a description of the background by relaxing the selection cuts. For the background distribution, five photons are required in the BGO, four of them are combined to $2\pi^0$ and have to fulfil the requirement to be within ±30 MeV of the π^0 mass. To suppress the signal channel the fifth photon must not pass the Σ^0 decay photon selection, thus it has to be outside of ±21 MeV of the decay photon energy of 74.42 MeV. Additionally up to two charged particles are allowed, but not required. The resulting spectrum is fitted to the data together with the same simulated expected signal spectrum as in Chapter 6.1.1.

The fits in the angular range $0.2 < \cos\theta_{\mathrm{CM}}^{K} < 0.5$ are shown in Fig. 6.5. The residuals are again shown underneath each plot. The fitted spectra look similar to those shown in Fig. 6.3. The fits appear to describe the data well, also the residuals are again centred around 0 and show no unexpected structures. As it was done in Chapter 6.1.1 the fit is repeated with only the background spectrum to test, whether this is enough to describe the data and the spectrum from $\gamma n \rightarrow K^0\Sigma^0$ is needed at all. These fits are shown in Fig. 6.6. Again it appears that the fits including signal describe the data better and show less structures in the residuals.

The extracted signal yield is shown in Fig. 6.7 together with the yield from chapter 6.1.1. Both spectra

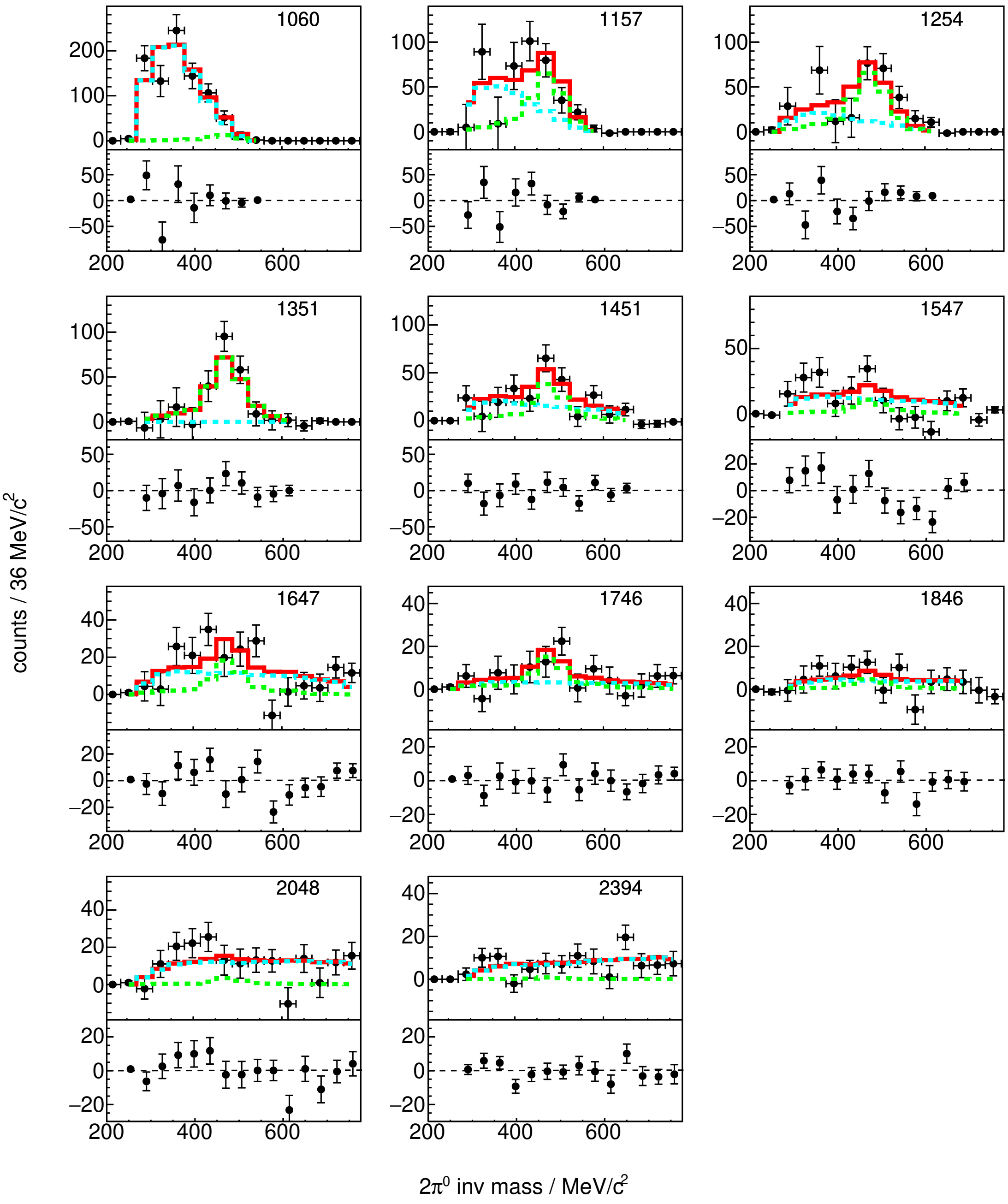

Figure 6.5: Fits for all energies in the angular range 0.2 $<\cos\theta^K_{\mathrm{CM}}< 0.5$. The data is fitted with the expected signal spectrum from simulated $\gamma n \to K^0\Sigma^0$ (green) and a background spectrum determined from real data with relaxed cuts (light blue). The full fit is shown in red. Underneath each fit the residuals are shown. The centre of each beam energy bin is given in the top right corner of each plot in MeV.

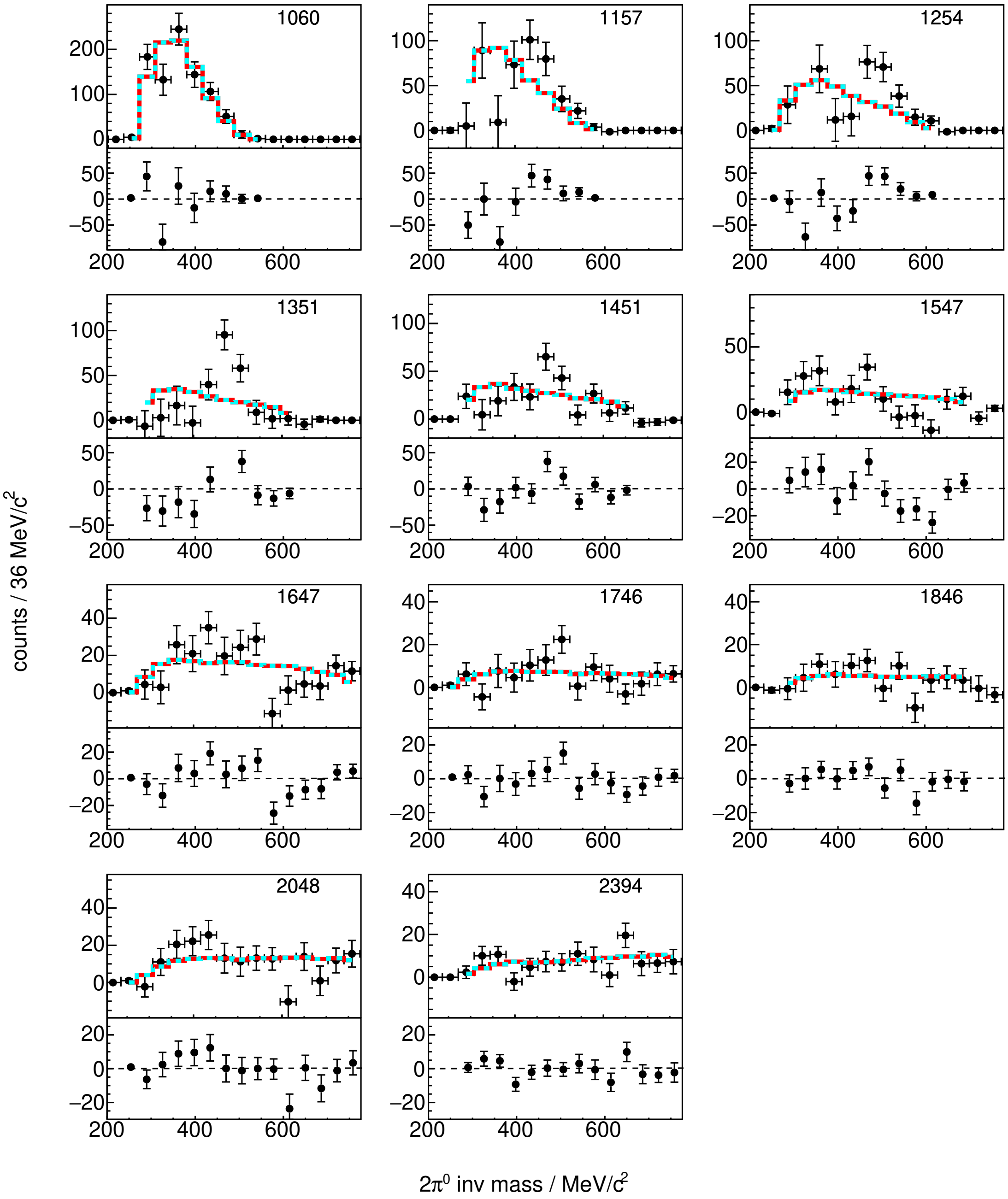

Figure 6.6: Fits for all energies in the angular range $0.2 < \cos\theta^K_{\mathrm{CM}} < 0.5$. The data is fitted with a background spectrum determined from real data with relaxed cuts (light blue). The full fit is shown in red. Underneath each fit the residuals are shown. The centre of each beam energy bin is given in the top right corner of each plot in MeV.

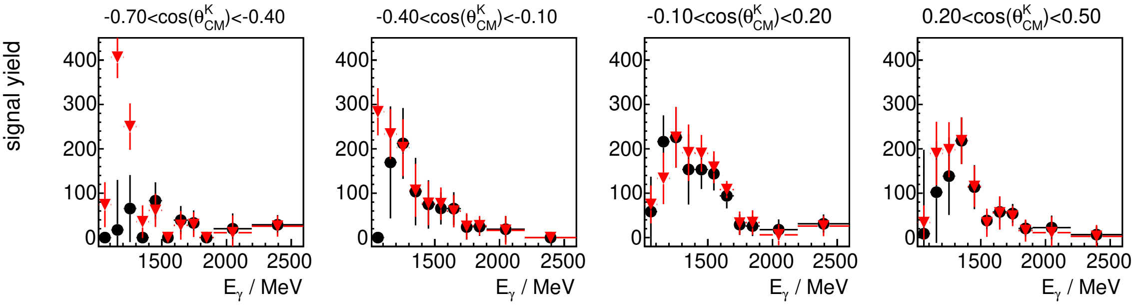

Figure 6.7: Signal yield extracted for both ways of describing the background (PS is shown in black, RD in red). Horizontal errors bars indicate the bin width.

agree very well in general. Only close to threshold the yield from the two methods differs. Fig. 6.8 shows the $2\pi^0$ invariant mass spectrum for $1\,109\,\mathrm{MeV} < E_\gamma < 1\,206\,\mathrm{MeV}$ and $-0.7 < \cos\theta^K_{\mathrm{CM}} < -0.4$, one of the bins where this happens. Fig. 6.8(a) shows the fit using the PS background description, Fig. 6.8(b) shows the one using real data with relaxed selection cuts (RD). The data show a peak like structure, by eye it is not possible to decide whether this peak is signal or background or a combination of both. Close to threshold the phase space is limited, the background has a similar shape as the signal. The PS method can describe the fitted spectrum almost entirely with one background channel, the signal contribution is very small. The RD method on the other hand uses real data with relaxed selection cuts. For these data the phase space is not that limited which results in a slightly broader shape. To describe the fitted spectrum a large contribution from the expected signal spectrum is included. These two effects cause the difference in the yield, the PS method can not differentiate between background and signal and the background shape used for the RD method does not describe the actual background very well that close to threshold. Though at first glance the PS method appears to describe the fitted spectrum better, it will become obvious in later steps, that it must underestimate the signal contribution. More statistics and a finer binning in the $2\pi^0$ invariant mass might help with this in the future.

These differences occur only in a few bins directly at threshold and in backwards direction. At higher beam energies and more forward angles the agreement between the two methods is very good, background and signal shape are more distinctive there and the fitted spectrum is as broad as the RD background shape, as can also be seen in Fig. A.7 to A.12. The agreement between the two methods shows, the reduced selection of background channels in chapter 6.1.1 was sufficient to describe the background shape. If a significant channel would be missing, this would be visible as a difference in the extracted signal yield. It is clear, however, that in most bins the K^0_S signal is at the statistical edge of being observable. To investigate whether the fits including the expected signal spectrum actually describe the data better than the ones using only background, several tests are performed and described in Chapter 6.2.

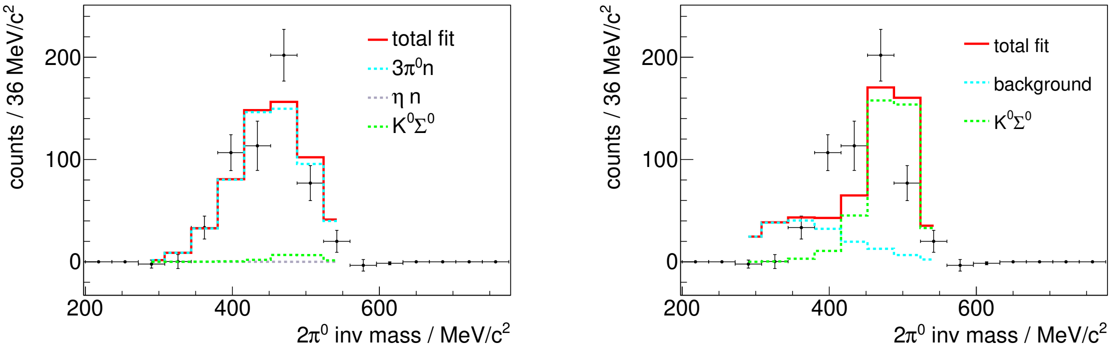

(a) Fit using PS background description.

(b) Fit using real data with relaxed cuts to describe the background.

Figure 6.8: Fit to the $2\pi^0$ invariant mass spectrum in the angular range $-0.7 < \cos\theta^K_{\mathrm{CM}} < -0.4$ and for beam energies $1\,109\,\mathrm{MeV} < E_\gamma < 1\,206\,\mathrm{MeV}$. The labelling of the different contributions is given in the figure.

6.2 Fit Quality Tests

The very limited statistics make it necessary to check whether and to what extent the reaction $\gamma n \to K^0\Sigma^0$ is needed to describe the data, as the expected peak is not always clearly visible. Therefore several tests of the fit quality are performed. The most common value to describe the quality of a fit is χ^2. As this requires a certain amount of statistics, a Kolmogorov-Smirnov test and a hypothesis test are performed in addition. The former is intended for unbinned data, the bias created by using it on binned data should cancel out however in the comparison of two results. The latter allows to specify a probability for an agreement with a certain hypothesis. Giving an exact limit for this agreement requires an exact description of the hypothesis model to compare the data with. Here the test will be used to qualitatively compare fits including and excluding the signal spectrum and is used together with the results of the other tests to give an indication as to whether the reaction $\gamma n \to K^0\Sigma^0$ is needed to describe the present data set.

6.2.1 χ^2/ndf

An often used value to give the quality of a fit is χ^2/ndf, where

$$\chi^2 = \sum_{\text{bins}} \left(\frac{N_{\text{fit, bin}} - N_{\text{data, bin}}}{\Delta N_{\text{data, bin}}} \right)^2 \tag{6.1}$$

with $N_{\text{fit, bin}}$ and $N_{\text{data, bin}}$ being the number of events in each bin of the fitted spectrum for the fitted function and the data respectively and $\Delta_{\text{data, bin}}$ the error of the data in the corresponding bin. ndf is the number of degrees of freedom. However this value does only follow the expected distribution if the statistics of the data are high enough[1]. This is not always given here, some bins have very few or even no entries.

---

[1] Often at least 5 entries per bin are considered as necessary

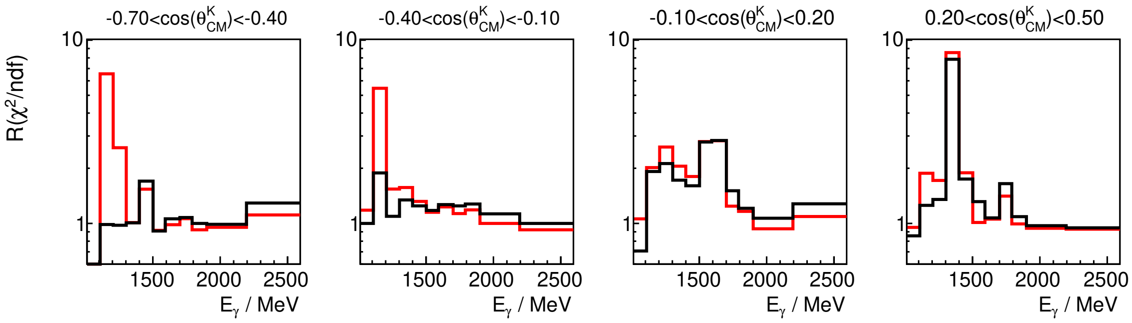

Figure 6.9: Ratio of χ^2/ndf values for fits without and with signal. Shown is the spectrum where the background is determined with the PS-method in black and the spectrum where the background is determined from real data (RD) in red. Note the logarithmic scale of the y-axis.

Still the values will be looked at. The full tables with all values can be found in Tables B.1 and B.2. Many fits have a χ^2/ndf value around 1 but there are also some bins with χ^2/ndf values significantly below one. To reduce possible effects coming from too little statistics the ratio

$$\mathrm{R}(\chi^2/\mathrm{ndf}) = \frac{\chi^2/\mathrm{ndf(Background)}}{\chi^2/\mathrm{ndf(Background + Signal)}} \tag{6.2}$$

is an interesting value. This ratio of the values for fits without and with the signal spectrum is shown in Fig. 6.9 for both methods to describe the background. Both spectra have a similar shape and are larger 1 for many bins. This shows, the value for fits including the signal is smaller than the value for fits without the signal indicating that fits including the signal spectrum describe the data better than the ones without. Note especially the second peak in the most forward angular bin. This region will become important later.

As some bins have very low χ^2/ndf no final statement can be made about the quality of the fits on the basis of this and further tests have to be performed.

6.2.2 Kolmogorov-Smirnov Test

The second test to investigate whether the $\gamma n \to K^0\Sigma^0$ contribution is needed for the fits is a Kolmogorov-Smirnov test [51]. This test is intended to compare two unbinned functions and give a probability how alike their shape is. As the data here is given in bins the test has to be treated with care. Root provides the test as a function for binned histograms with three remarks:

"Therefore, we believe that for all practical purposes, the probability value PROB is calculated correctly provided the user is aware that:

1. The value of PROB should not be expected to have exactly the correct distribution for binned data.

2. The user is responsible for seeing to it that the bin widths are small compared with any physical phenomena of interest.

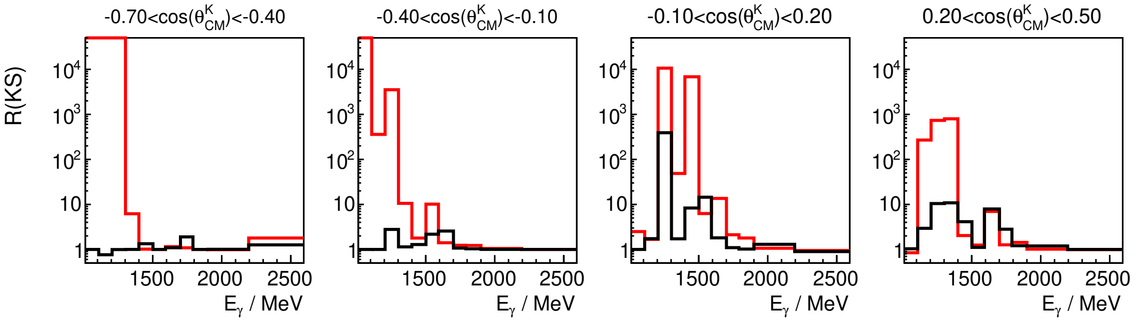

Figure 6.10: Ratio of the probability KS given by the Kolmogorov-Smirnov Test for fits with and without signal. Shown is the spectrum where the background is determined with the PS-method in black and the spectrum where the background is determined from real data (RD) in red.

3. The effect of binning (if any) is always to make the value of PROB slightly too big. That is, setting an acceptance criterion of (PROB>0.05 will assure that at most 5% of truly compatible histograms are rejected, and usually somewhat less." [52]

The second point is not true in this case, therefore the test will not be used to give a probability of one fit describing the data, but as a comparison of two results. The data is fitted once with background and signal and once with background only. The test is performed for each fit and gives a probability of the compatibility of the fitted function and the data. One means identical, a value much smaller than one means not compatible. If the fit including the signal describes the data better than the one without, the probability KS given by the Kolmogorov-Smirnov Test will be closer to one. The resulting probability values can be found in table B.3 for the PS and B.4 for the RD method. When looking at the ratio R(KS) of the probabilities

$$\mathrm{R(KS)} = \frac{\mathrm{KS(Signal+Background)}}{\mathrm{KS(Background)}} \tag{6.3}$$

possible binning effects should cancel out. Compared to Eqn. 6.2 this ratio is the inverse, this way the two results are better to compare. If the value KS(Signal+Background) is closer to one than KS(Background) the ratio R(KS) is larger one. Fig. 6.10 shows R(KS) for both ways of describing the background (PS and RD). The ratio is larger 1 in many bins, indicating that fits including the $\gamma n \to K^0\Sigma^0$ spectrum indeed describe the data better than the ones without. Again, notice the second peak in the most forward angular bin, hinting at a significant signal contribution in this energy region. As a few bins have very small values of KS and the test is not originally intended for binned data further tests are performed.

6.2.3 Hypothesis Test

The very limited statistics make it sometimes difficult to identify the signal peak by eye and makes other tests of the quality of fits difficult to interpret. As a third check that the data could not be fitted as well by only background, a hypothesis test is performed. The hypothesis H_0 here is: The measured data is only background. This hypothesis is tested by creating and fitting a Monte Carlo toy model from which a probability distribution of the data being only background can be determined.

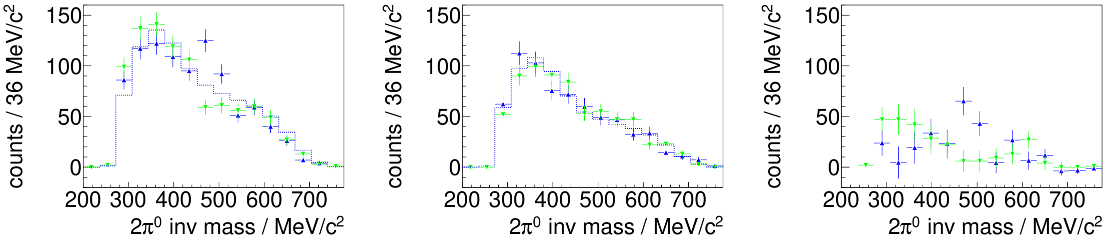

(a) $2\pi^0$ invariant mass spectrum off deuterium before subtracting hydrogen data.

(b) $2\pi^0$ invariant mass spectrum off hydrogen data.

(c) Remaining neutron component of the $2\pi^0$ invariant mass spectrum after hydrogen was subtracted from deuterium.

Figure 6.11: Example of the $2\pi^0$ invariant mass spectrum. Shown in blue is the measured real data spectrum. The dashed blue line is the background only fit to the real data from which a random sample is generated (green). For details see text.

The simplest way would be fitting the data with background only and generating random toy samples from this distribution. However these toy samples would have wrong errors. Due to the subtraction of hydrogen data the error is not $\sqrt{N}$ but more complex. The solution to this is fitting the deuterium data before subtraction, generating a toy sample from this and subtracting a second toy sample generated from a fit to the hydrogen data. Each sample is generated to have the same number of events as the real data. This is a good approximation, an example is shown in Fig. 6.11. The subtracted MC toy sample is then treated as if it were measured data and fitted as described in Chapters 6.1.1 and 6.1.2. Each sample is fitted twice, once with background and expected signal distribution and once with the background distribution only. For each fit

$$\zeta^2 = \sum_{\text{bins}} \left(\frac{N_{\text{fit, bin}} - N_{\text{data, bin}}}{\Delta N_{\text{data, bin}}} \right)^2 \tag{6.4}$$

is calculated, with $N_{\text{fit, bin}}$ and $N_{\text{data, bin}}$ being the number of events in each bin of the fitted spectrum for the fitted function and the data respectively and $\Delta N_{\text{data, bin}}$ its corresponding error. ζ^2 is a measure of how well the fit describes the data. If fit and data were in 100% agreement, ζ^2 would be 0. The larger the value the smaller the agreement.

For each sample the difference

$$\Delta\zeta^2 = \zeta^2(\text{Background}) - \zeta^2(\text{Signal+Background}) \tag{6.5}$$

is calculated. A positive value means the fit including the expected signal distribution agrees better to the data then the one without. $\Delta\zeta^2$ can not be negative, if the signal contribution does not improve the fit, this contribution is 0 and the fit is the same as the one without signal contribution. In this case $\Delta\zeta^2$ is 0. This is repeated 10000 times for every energy and $\cos\theta^K_{\text{CM}}$ range.

The resulting distribution of $\Delta\zeta^2$ under the hypothesis H_0 is called $g(\Delta\zeta^2|H_0)$. $g(\Delta\zeta^2|H_0)$ is expected to peak at 0 with a tail in positive direction. This tail is created by samples that by chance appear to have a signal peak.

An example for the distributions $g(\Delta\zeta^2|H_0)$ is shown in Fig. 6.12. The integral is normalized to

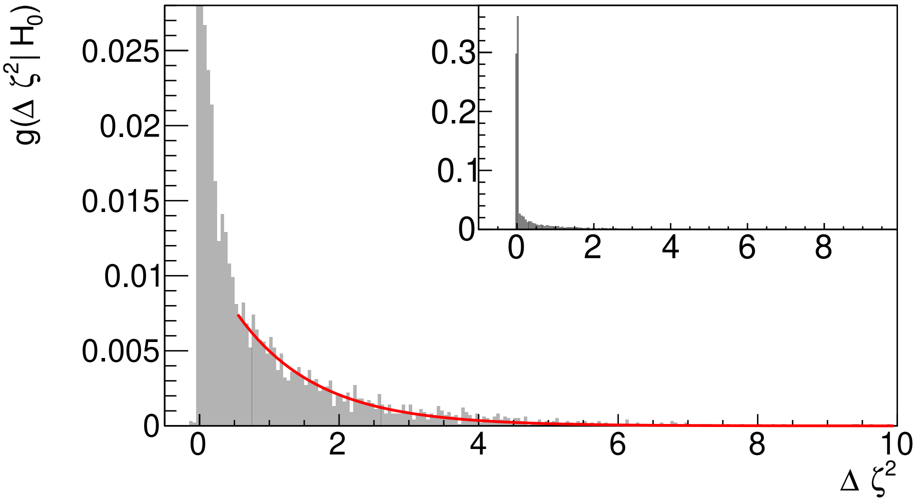

Figure 6.12: Example of $g(\Delta\zeta^2|H_0)$. Shown is the distribution of 10000 values of $\Delta\zeta^2$ under the hypothesis H_0. The integral is normalized to 1. To extend the accessible region the tail is fitted with an exponential function. The top right corner shows the full distribution, the large plot is zoomed in on the y-axis to show the tail and the function fitted to it.

one. $g(\Delta\zeta^2|H_0)$ looks as expected with a peak at 0 and a tail towards positive values. Even though 10000 samples were used to generate the spectrum the tail only contains few events and stops at lower values of $\Delta\zeta^2$ than will be needed in later steps. To get a description of $g(\Delta\zeta^2|H_0)$ at higher values, either a very large amount of samples can be generated or, as it is done in this case, the tail is fitted with an exponential function to extend the accessible region of $\Delta\zeta^2$. This has the disadvantage, that the distribution will never be 0. Therefore an upper limit has to be chosen. Here the upper limit is chosen at $\Delta\zeta^2 = 10000$. This value is high enough that all values of $\Delta\zeta^2_{\text{real}}$ are in the covered range. $\Delta\zeta^2_{\text{real}}$ is calculated as in Eqn. 6.4 and 6.5 but after fitting to the real data instead of the MC samples.

This then allows to calculate

$$p = \int_{\Delta\zeta^2_{\text{real}}}^{\infty} g(\Delta\zeta^2|H_0). \tag{6.6}$$

p describes the probability for $\Delta\zeta^2$ having a value equal or higher than the one observed with the real data, so p is a measure for the compatibility with H_0. $p = 1$ means the measured real data is 100% compatible with the hypothesis of them originating from only the given background distributions. The smaller p, the less likely this is.

This statement can not be reversed however. A small value of p does not mean, that the expected signal distribution is true. Additionally the use of approximations in the model and in the determination of p might introduce a bias in the results. Therefore, here the test is performed to get a qualitative impression whether including the signal spectrum in the fit gives an improvement, not a quantitative limit.

Fig. 6.13 shows p for all energies and angles for both ways of describing the background. The general shape of the p-Value distribution agrees for both methods. Many bins have a very small p,

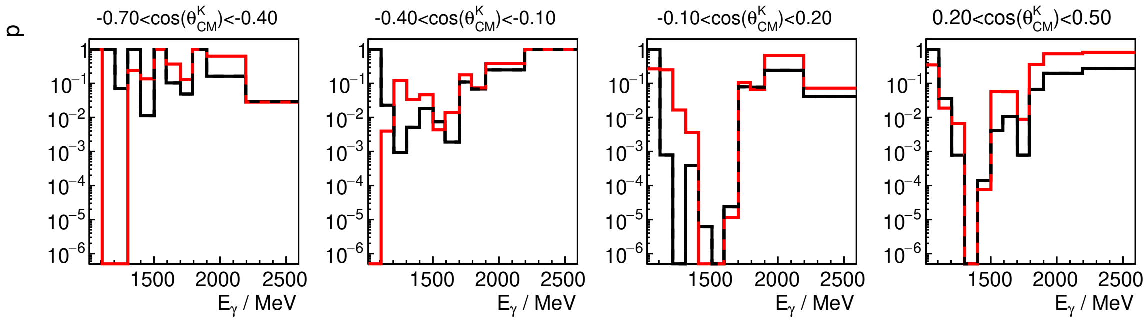

Figure 6.13: Spectrum of p-Values for both background models (PS black, RD red). The spectrum is cut off at $5 \cdot 10^{-7}$. A table of all values can be found in the appendix.

indicating that in these bins the background distributions alone are not sufficient to describe the data. All values of $\Delta\zeta^2_{\text{real}}$ with the corresponding p-Value can be found in tables B.5 and B.6.

A comparison of the p-Value distributions with the results of the Kolmogorov and χ^2 test shows a similar behaviour. In the first two angular bins all three tests show many energy bins with results in a region that might be compatible with a background only distribution and might not need a signal distribution to describe the data. When going to the third angular bin the values go further away from the region that indicates compatibility with a background only distribution. In the most forward angular bin $0.2 < \cos\theta^K_{\text{CM}} < 0.5$ all three tests show two regions where the fits including the expected signal distribution appear to describe the data better. The extracted yield shows similar structures. This is taken as a clear indication, that the extracted signal yield is not just a statistical fluctuation of background, but real. To verify this from a different perspective, further methods to extract the signal yield are performed.

6.3 Sideband Subtraction

In addition to the complex RooFit method a more simple side band fitting technique is performed to extract the signal yield. While RooFit has the advantage of being able to describe the entire spectrum, the shape of the signal spectrum has to be assumed and the yield is extracted on this assumption. When using a side band fit, only the position and an estimate of the width of the signal peak is required and only the background outside of this peak is fitted and interpolated into the signal region.

The expected position and width of the K^0_S peak in the $2\pi^0$ invariant mass spectrum is determined from simulated $\gamma n \to K^0\Sigma^0$. The region outside approximately $\pm 1.5\sigma$ of the K^0_S peak is fitted with a polynomial of 3^{rd} degree. The limits are chosen to lie at a bin border of the histogram of the $2\pi^0$ invariant mass spectrum at 416 MeV and 525 MeV. Fig. 6.14 shows the fits in the angular range $0.2 < \cos\theta^K_{\text{CM}} < 0.5$ for all energies. All other fits can be found in the appendix (Fig. C.1 to C.3). The polynomial function is evaluated at each data point in the region within $\pm 1.5\sigma$ of the K^0_S peak and then subtracted from the value of the corresponding data point. The integral of the remaining entries over all points within the region of the K^0_S peak is the K^0_S yield shown in Fig. 6.15 (brown stars). Close to threshold and in the more backwards angular regions there are several negative entries. Most are consistent with 0 within the statistical uncertainty, only two data points directly at threshold are

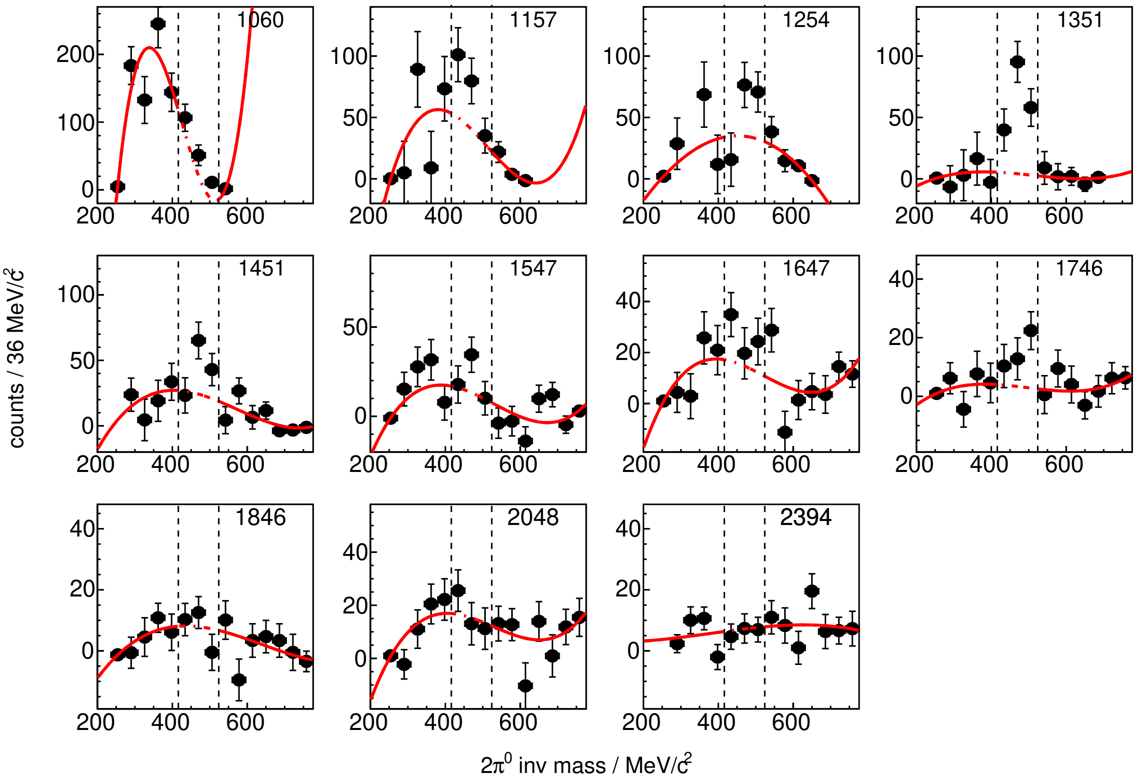

Figure 6.14: $2\pi^0$ invariant mass spectrum in the angular range $0.2 < \cos\theta^K_{\mathrm{CM}} < 0.5$. The region within the black dashed lines is identified as signal region. A polynomial of 3^{rd} degree is fitted to the data outside this region (red line). The fitted function is interpolated to the signal region (red dashed line). The centre of each energy bin is given in each bin in MeV.

not compatible. Directly at threshold the fitted spectrum is relatively narrow due to limited phase space. Only few data points can be fitted outside the signal region which is not enough to get a good description of the spectrum. Data points with negative yield can not lead to a physical cross section. As there are only two of them they will still be shown in later steps.

To check the consistency of the fits, the background yield is also regarded, it should follow a smooth distribution. Fig. 6.16 shows the background yield within $\pm 1.5\sigma$ of the signal region determined from the fitted function (brown stars). While the shape is relatively smooth in the first two angular bins it becomes less so in the angular range from $-0.1 < \cos\theta^K_{\mathrm{CM}} < 0.2$. The last angular range from $0.2 < \cos\theta^K_{\mathrm{CM}} < 0.5$ shows a smooth behaviour in general with two bins lying away from the others[2]. These outliers in the background may have an effect on the K_S^0 yield and thus on the determined cross section. Therefore the yield is determined again after averaging the background over neighbouring energy bins.

Averaging the background means, that for each data point of the $2\pi^0$ invariant mass spectrum outside the K_S^0 peak an average is calculated from the value itself and the values of the same data point in the neighbouring energy bins. Where neighbouring energy bins have different width the entries are

---

[2] The last two energy bins are larger than the others, and are therefore expected to have a higher background yield.

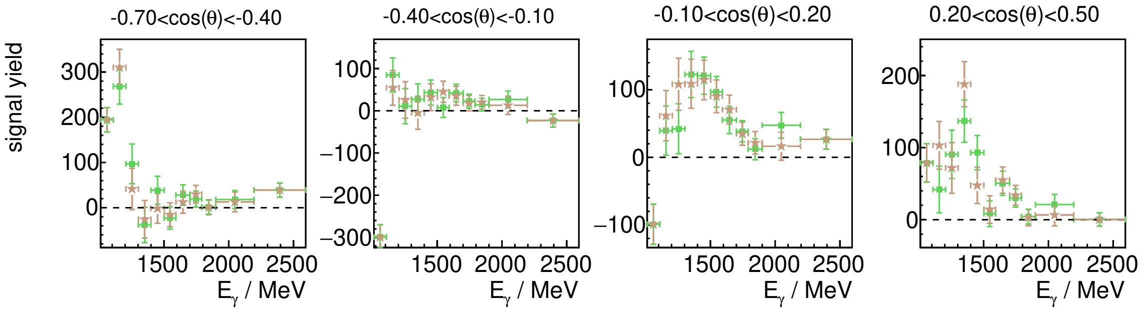

Figure 6.15: Signal yield determined from a fit to the sidebands (brown). Also shown is the yield after averaging the background distribution (green, explanation see text). Horizontal errors bars indicate the bin width.

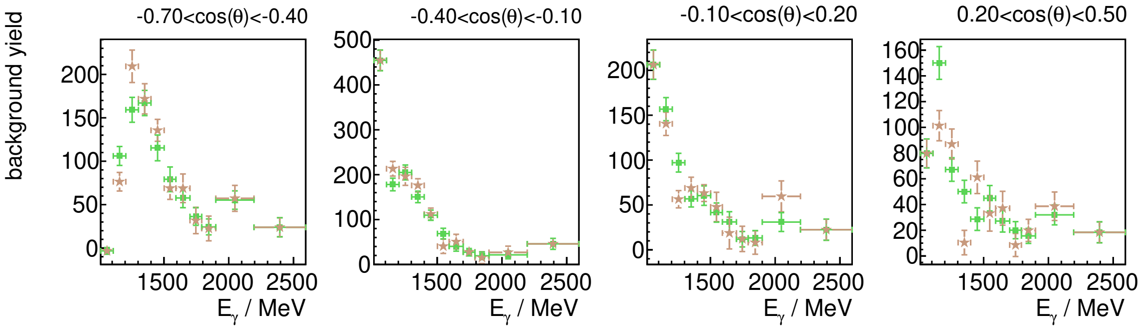

Figure 6.16: Background yield determined from a fit to the sidebands (brown). Also shown is the yield after averaging the background distribution (green, explanation see text). Horizontal errors bars indicate the bin width.

weighted by the bin width. This is done for all bins that have a neighbour at higher and lower energy.

The resulting $2\pi^0$ invariant mass spectra are fitted again with the polynomial function of 3^{rd} degree. The fits are shown in Fig. C.4 to C.7. Fig. 6.16 shows the background distribution after averaging (green squares). The outliers have disappeared and all shapes are smoother than before. The resulting K_S^0 yield is also shown in Fig. 6.15 (green squares). While averaging the background distribution smoothed the background distribution, only minor changes in the signal yield are visible, the difference remains within the statistical uncertainty.

As the yield extracted with this method only covers around 80% (approximately $\pm 1.5\sigma$ of the signal yield) it can not be directly compared to the yield extracted in chapter 6.1. This comparison is only possible, after the cross section is determined, where this is corrected for.

As a final test, the yield is extracted by fitting to the data in a larger angular range and that result is compared to the sum of the yield in the smaller angular bins in Chapter 6.4.

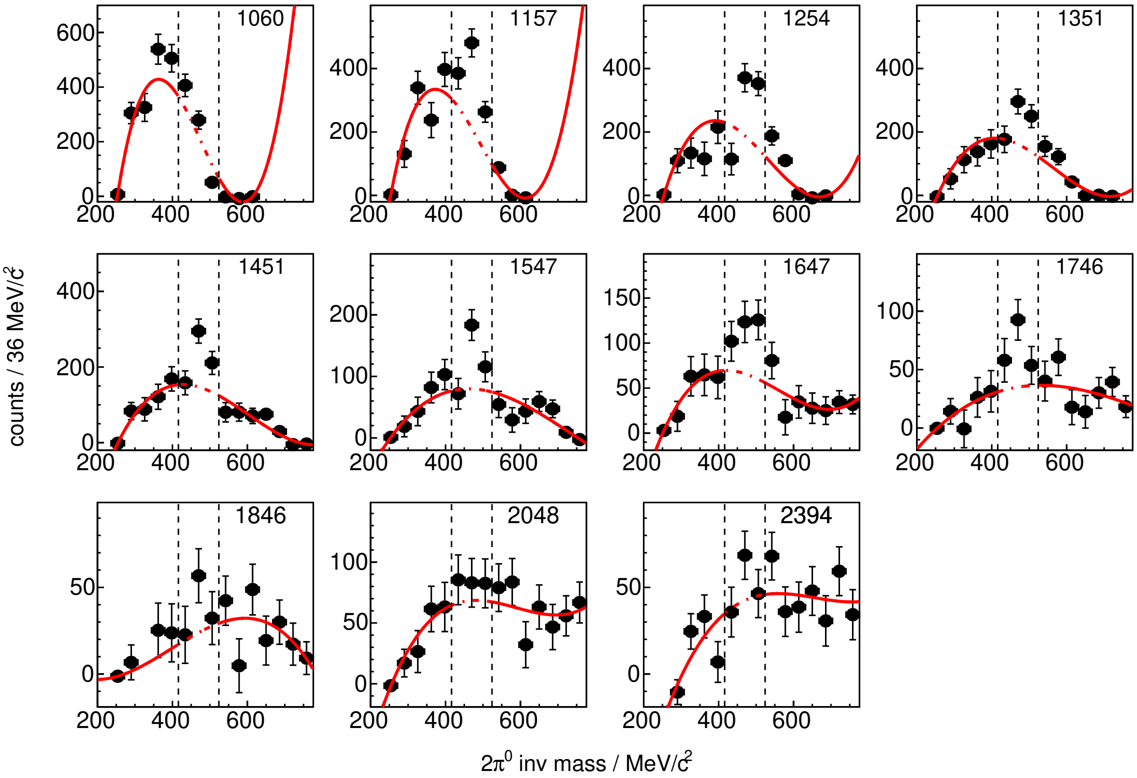

Figure 6.17: $2\pi^0$ invariant mass spectrum in the angular range $-0.7 < \cos\theta_{\mathrm{CM}}^{K} < 0.5$. The region within the black dashed lines is identified as signal region. In this large angular region a peak is visible within the signal region. A polynomial of 3^{rd} degree is fitted to the data outside this region (red line). The fitted function is interpolated to the signal region (red dashed line). The centre of each energy bin is given in each bin in MeV.

6.4 Comparing yield in larger bin

To test whether the yield extracted from the previous fits is in the right order of magnitude, all fits are repeated with only one large angular bin from $-0.7 < \cos\theta_{\mathrm{CM}}^{K} < 0.5$. This is done for the fits performed with RooFit and for the fits to the side bands. In this larger angular range the signal peak is clearly visible in most energy bins. The data is shown in Fig. 6.17 exemplary with the side band fit. All other fits (PS, RD and side band fit to averaged background) can be found in the appendix in Fig. D.1 to D.3. The yield extracted from this is labelled *total yield* and compared to the sum of the yields extracted from the four smaller bins.

If the fits to the smaller angular bins describe the data well, the sum of the extracted yield has to be the same as the one extracted from the larger angular bin. This comparison is done per energy bin and shown in Fig. 6.18. The upper plots show the extracted yields, the lower plots show the difference summed yield − total yield. In most cases the summed yield agrees very well to the yield extracted from the larger bin. The difference is consistent with 0. Only close to the threshold, where difficulties in the fitting were already observed, discrepancies can be seen.

While all previous fits and tests individually might not give unambiguous evidence that the fitted signal is true, they all give independent indications all directing towards a real signal. The comparison made in this chapter is again an indication that, even though the signal peak is not always visible by eye, the fits describe it well. When putting all this together the extracted signal yield appears reliable. In chapter 7 this yield is used to determine the differential cross section of the reaction $\gamma n \rightarrow K^0\Sigma^0$.

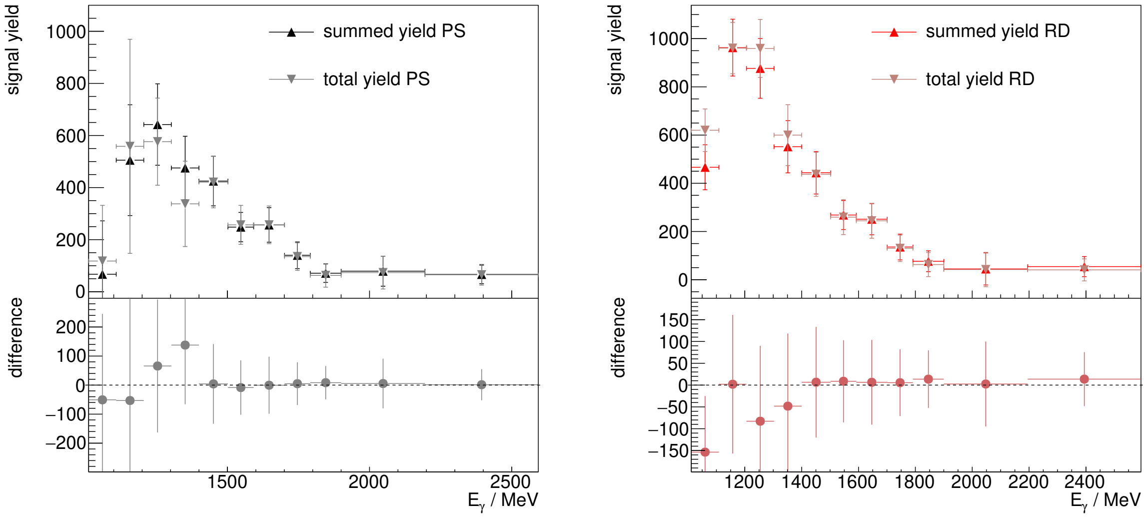

(a) Yield of the RooFit fit method determined from PS background description.

(b) Yield of the RooFit fit method determined from RD background description.

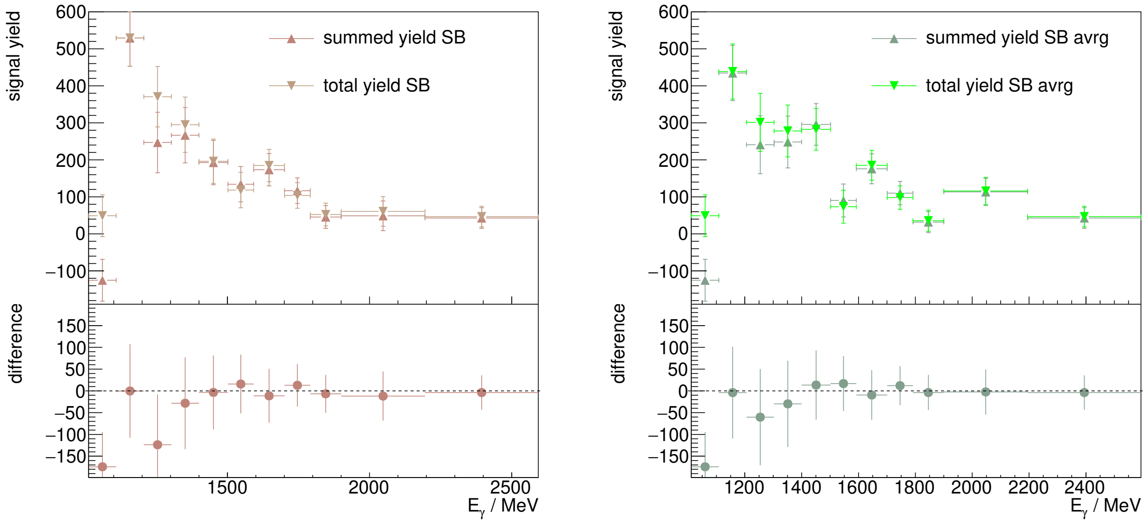

(c) Yield of the sideband subtraction.

(d) Yield of the sideband subtraction with averaged background.

Figure 6.18: Comparison of the summed yield of all four angular ranges with the yield determined from fits to the larger angular range $-0.7 < \cos\theta^K_{\mathrm{CM}} < 0.5$ (upper plots) for the four different fitting methods. The lower plots show the difference summed yield − total yield. Horizontal errors bars indicate the bin width.

CHAPTER 7

$\gamma n \to K^0\Sigma^0$ differential cross section

In this chapter the differential cross section of $\gamma n \to K^0\Sigma^0$ is determined from the K_S^0 yield extracted from the data in chapter 6. The yield is normalized by the reaction independent factors flux, target area density and the solid angle. It is also normalized by the reconstruction efficiency which describes the percentage of events of this specific reaction that can be observed in the detector, as described in chapter 7.1. As the fit to the $2\pi^0$ invariant mass can not differentiate between different sources of K_S^0 the extracted yield is contaminated with $\gamma n \to K^0\Lambda$, this contribution has to be removed (chapter 7.2). In chapter 7.3 the $\gamma n \to K^0\Sigma^0$ differential cross section is determined from the yield extracted with the different fits performed in chapter 6 and sources of uncertainties are discussed. Finally the measured cross section is compared to the theoretical predictions by T. Mart [30, 53] and by A. Ramos and E. Oset [28] (chapter 7.4).

7.1 Reconstruction Efficiency

To determine the differential cross section the yield has to be scaled by several factors namely the photon flux, the target area density, the reconstruction efficiency and the solid angle. The photon flux and the reconstruction efficiency depend on the beam energy, the reconstruction efficiency is additionally a function of $\cos\theta_{\mathrm{CM}}^K$. The former is determined from the number of photons measured in the tagging and flux monitoring system as explained in Ref. [45]. The latter is determined from simulated $\gamma n \to K^0\Sigma^0$ events.

The reconstruction efficiency *RE* describes the fraction of events that is actually measured in the detector and is determined by generating a number of events from Monte Carlo simulation and counting the number of events that are observed in the detector and pass all selection cuts as a function of beam energy and $\cos\theta_{\mathrm{CM}}^K$

$$RE(E_\gamma, \cos\theta_{\mathrm{CM}}^K) = \frac{N_{\mathrm{detected}}(E_\gamma, \cos\theta_{\mathrm{CM}}^K)}{N_{\mathrm{generated}}(E_\gamma, \cos\theta_{\mathrm{CM}}^K)}. \tag{7.1}$$

Fig. 7.1 shows the reconstruction efficiency for the $2\pi^0$ invariant mass spectrum that was used for the fits with Roofit in chapter 6.1 and for the one used for the side band fits in chapter 6.3. While the former uses to full $2\pi^0$ invariant mass spectrum to determine the K_S^0 yield, the latter only considers the region within approximately $\pm 1.5\sigma$ of the K_S^0 peak as signal region. Therefore, the reconstruction

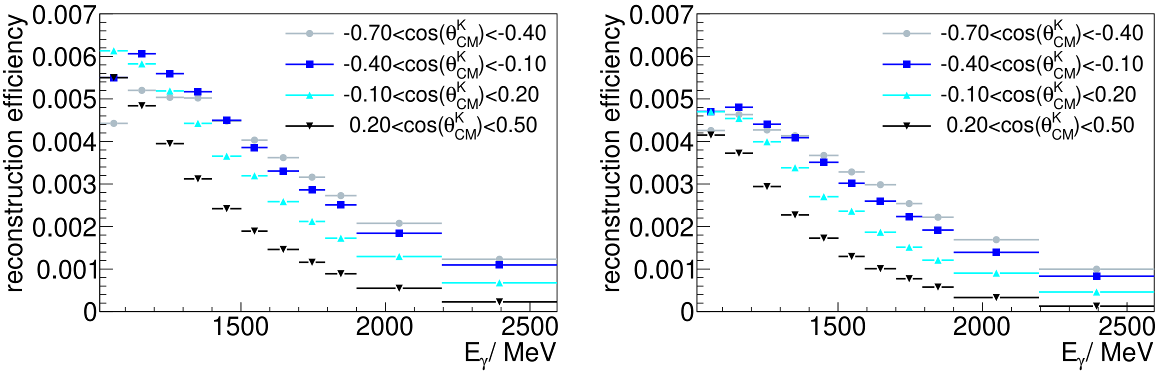

(a) Reconstruction efficiency of the reaction $\gamma n \to K^0\Sigma^0$ for the full $2\pi^0$ invariant mass spectrum.

(b) Reconstruction efficiency of the reaction $\gamma n \to K^0\Sigma^0$ for the $2\pi^0$ invariant mass spectrum approximately $\pm 1.5\sigma$ around the K^0_S peak used in chapter 6.3 for the side band fit.

Figure 7.1: Reconstruction efficiency of the reaction $\gamma n \to K^0\Sigma^0$ from threshold to 2 594 MeV in four bins in $\cos\theta^K_{\mathrm{CM}}$. Horizontal errors bars indicate the bin width.

efficiency has to be determined from this reduced spectrum.

The reconstruction efficiency includes the branching ratios of the K^0 eigenstates K^0_L and K^0_S and the detected K^0_S and Λ decay modes, which limits it to ≈10%. Requesting 5 γ in the BGO calorimeter reduces it below 1%. In case of the side band fits it is further reduced by about 20% which is expected as it covers only approximately $\pm 1.5\sigma$ of the signal peak. In all cases the efficiency decreases towards higher beam energy and shows no jumps or any other structures that would cause a structure in the cross section.

7.2 $\gamma n \to K^0\Lambda$ contamination of the K^0_S yield

The fitting to the $2\pi^0$ invariant mass spectrum can not differentiate between different sources of K^0_S. Therefore, the K^0_S yield extracted in chapter 6 is a mixture of $\gamma n \to K^0\Sigma^0$ and $\gamma n \to K^0\Lambda$. However, the selection cuts strongly suppressed the contribution from $\gamma n \to K^0\Lambda$. The reconstruction efficiency of $\gamma n \to K^0\Lambda$ shown in Fig. 7.2 is a factor 10 smaller then the one of $\gamma n \to K^0\Sigma^0$shown in Fig. 7.1. The $\gamma n \to K^0\Lambda$ differential cross section has been measured by N. Compton et al. [54]. From this and the reconstruction efficiency the contribution from $\gamma n \to K^0\Lambda$ to the measured K^0_S yield can be calculated as

$$\mathrm{yield}_{K^0\Lambda} = \frac{d\sigma_{K^0\Lambda}}{d\Omega} \cdot RE_{K^0\Lambda} \cdot F \cdot \rho \cdot \Delta\Omega \tag{7.2}$$

with the Flux F, the target area density ρ, the solid angle $\Delta\Omega$ and the reconstruction efficiency $RE_{K^0\Lambda}$ of the reaction $\gamma n \to K^0\Lambda$. For the cross section $d\Sigma_{K^0\Lambda}/d\Omega$ the data points where energy and $\cos\theta^K_{\mathrm{CM}}$ are closest to the bin centre used in this thesis are taken from Ref. [54]. Fig. 7.3 shows the extracted K^0_S yield together with the contribution from $\gamma n \to K^0\Lambda$ calculated from Eqn. 7.2. This contribution is highest directly at threshold with maximum 55 events and drops rapidly. At a beam energy of

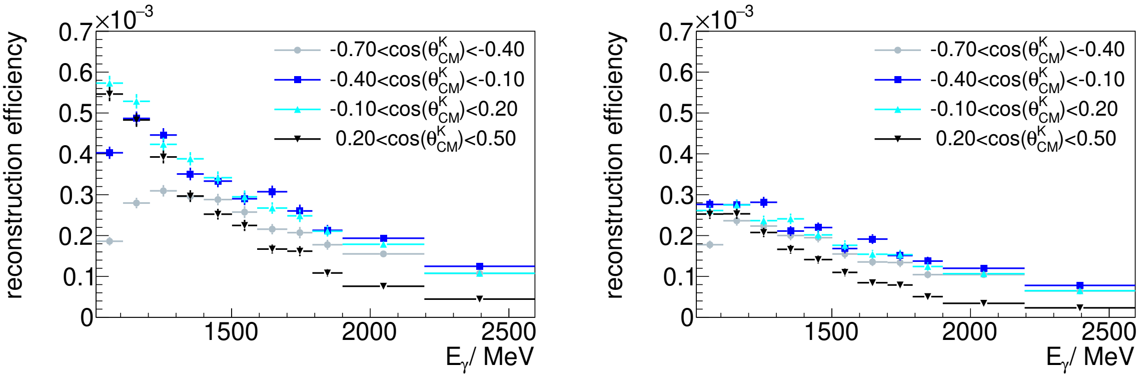

(a) Reconstruction efficiency of the reaction $\gamma n \rightarrow K^0\Lambda$ for the full $2\pi^0$ invariant mass spectrum.

(b) Reconstruction efficiency of the reaction $\gamma n \rightarrow K^0\Lambda$ for the $2\pi^0$ invariant mass spectrum approximately $\pm 1.5\sigma$ around the K^0_S peak used in chapter 6.3 for the side band fit.

Figure 7.2: Reconstruction efficiency of the reaction $\gamma n \rightarrow K^0\Lambda$ from threshold to 2 594 MeV in four bins in $\cos\theta^K_{\mathrm{CM}}$. Horizontal errors bars indicate the bin width.

1 500 MeV only few events from $\gamma n \rightarrow K^0\Lambda$ contribute to the measured K^0_S yield. In most bins the contribution of $\gamma n \rightarrow K^0\Lambda$ is only an effect of a few percent.

To determine the $\gamma n \rightarrow K^0\Sigma^0$ differential cross section a clean yield of only $\gamma n \rightarrow K^0\Sigma^0$ events is needed. To achieve this, the contribution from $\gamma n \rightarrow K^0\Lambda$, calculated from Eqn. 7.2, is subtracted from the measured K^0_S yield, denoted yield_{K^0X}, and only the contribution from $\gamma n \rightarrow K^0\Sigma^0$ remains

$$\mathrm{yield}_{K^0\Sigma^0} = \mathrm{yield}_{K^0X} - \mathrm{yield}_{K^0\Lambda}. \tag{7.3}$$

In some bins the contamination from $\gamma n \rightarrow K^0\Lambda$ is actually larger than the measured K^0_S yield. This will results in negative values for the $\gamma n \rightarrow K^0\Sigma^0$ yield which is of course unphysical. However, in most bins a $\gamma n \rightarrow K^0\Sigma^0$ yield equal or larger 0 is still consistent within the statistical uncertainty. Where this is not the case, already the measured K^0_S yield was negative as it happened when fitting the side bands (See chapter 6.3), or 0, as it happened when using the PS background description. As discussed in chapter 6.1.1, in these bins at least one reaction channel used to describe the background peaks at the same $2\pi^0$ invariant mass as the expected signal distribution and the fitted spectrum can be described using only background. This is the case for example directly at threshold, where the phase space is small. This makes the fitting difficult and it is possible that the fit underestimates the contribution from the expected signal distribution. These data points can not give a valid cross section value. As there are few of them and for sake of completeness they are still shown in later steps.

7.3 Determination of $\gamma n \rightarrow K^0\Sigma^0$ differential cross section

After subtracting the contamination from $\gamma n \rightarrow K^0\Lambda$ the K^0_S yield is pure $\gamma n \rightarrow K^0\Sigma^0$ and the differential cross section of the reaction $\gamma n \rightarrow K^0\Sigma^0$ can be determined. Fig. 7.4(a) shows the cross section in four different angular intervals as a function of beam energy from threshold to a beam

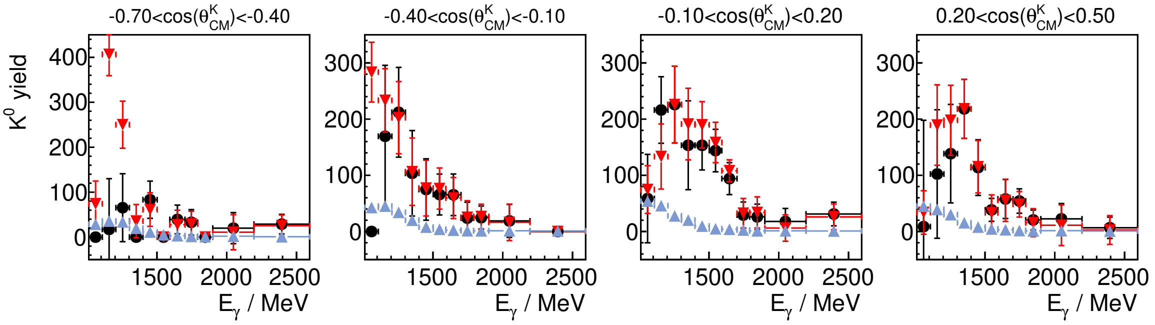

(a) K^0_S yield determined with fits using Roofit for two different methods of describing the background (PS black circles, RD red triangles). The contribution from $\gamma n \to K^0\Lambda$ is shown as blue triangles.

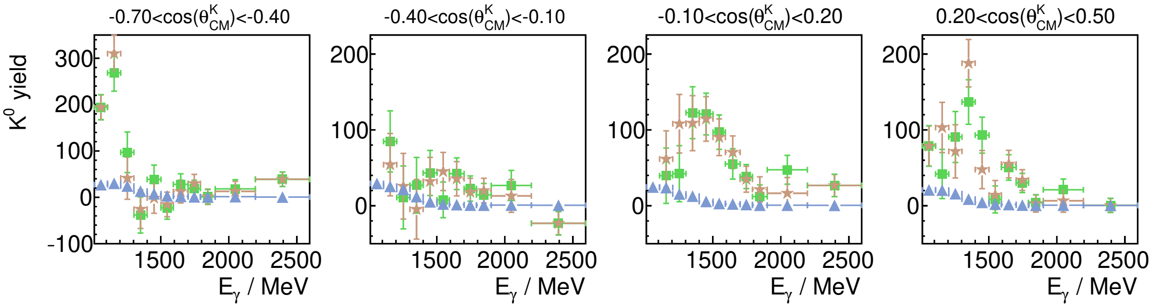

(b) K^0_S yield determined from a fit to the side bands (brown stars) and to the averaged side bands (green squares). The contribution from $\gamma n \to K^0\Lambda$ is shown as blue triangles. The plots are zoomed in to show the contribution from $\gamma n \to K^0\Lambda$. The first data point in the angular ranges $-0.4 < \cos\theta^K_{\mathrm{CM}} < -0.1$ and $-0.1 < \cos\theta^K_{\mathrm{CM}} < 0.2$ lies outside the shown range. The full range can be seen in Fig. 6.15.

Figure 7.3: K^0_S yield and the contribution from $\gamma n \to K^0\Lambda$ for different methods of fitting the $2\pi^0$ invariant mass spectrum. Horizontal errors bars indicate the bin width.

energy of 2 594 MeV. Plotted are the results determined from fits using Roofit together with the results from side band fits.

In the most backward angular bin, the cross section rises directly at threshold before dropping again. Only the cross section determined using the PS background description remains below 0.05 μb/sr. This method also produced data points below 0. Directly at threshold the limited phase space causes the background to peak at the same position as the expected signal. This makes it difficult to separate background and signal and causes the observed discrepancy between the different methods as well as the negative entries (see chapters 6.1 and 7.2). At beam energies higher than 1 300 MeV all methods are consistent within the statistical uncertainty and remain below 0.05 μb/sr.

In the second angular bin $-0.4 < \cos\theta^K_{\mathrm{CM}} < -0.1$ the cross section is mostly flat and remains below 0.1 μb/sr. Close the threshold there is again a discrepancy between the different methods. The reason is the same as before, close to threshold it is difficult to separate background and signal. This problem occurs less when going to more forward directions. In the angular bin $-0.1 < \cos\theta^K_{\mathrm{CM}} < 0.2$ it is only visible in the very first data point. The cross section in this bin rises up to 0.1 μb/sr at a beam energy

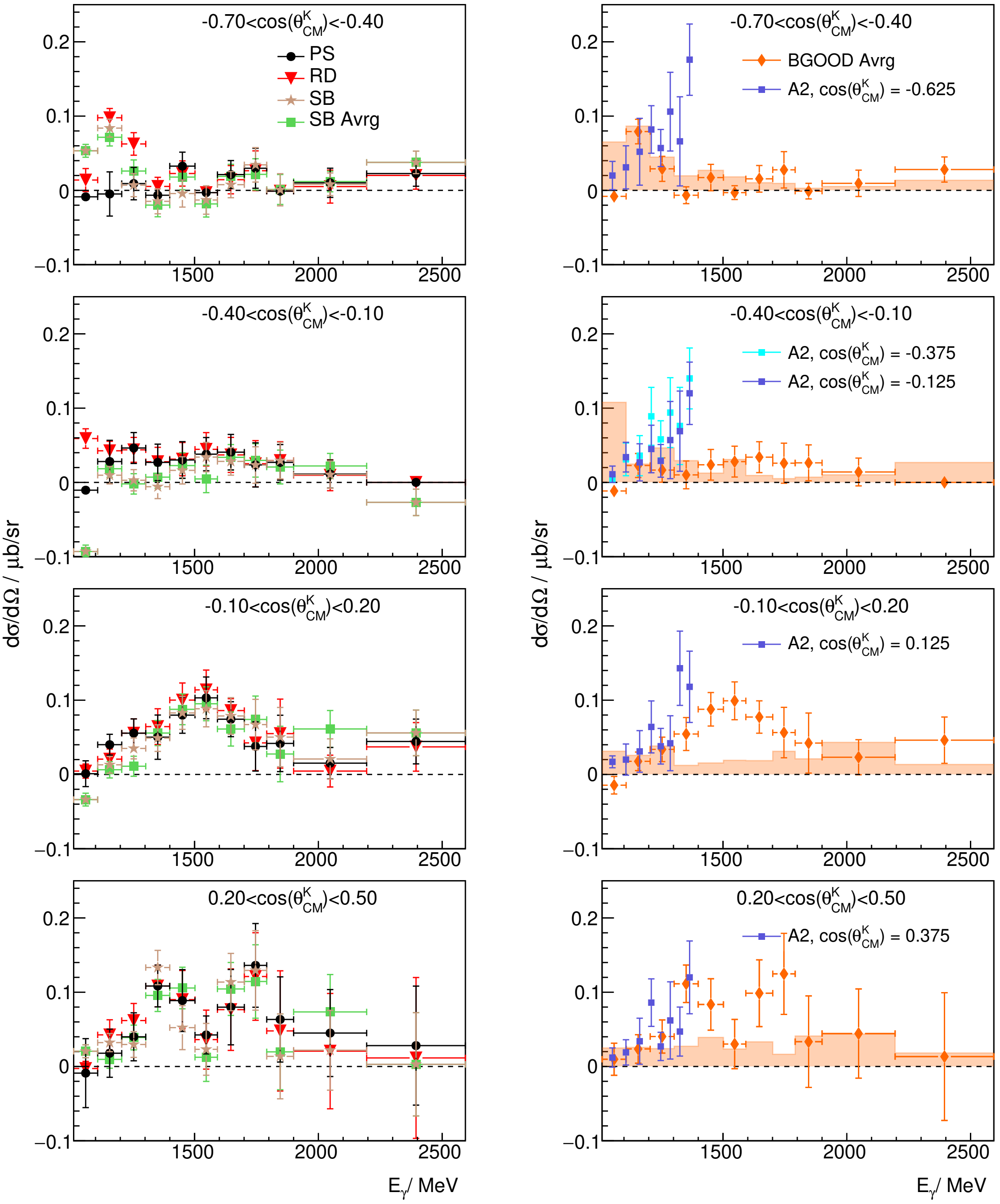

(a) Results of four different methods to fit to the data (PS black circles, RD red triangles, side band fits brown stars, fits to averaged side bands green squares).

(b) Error weighted average of the four different methods to fit to the data (orange triangles). The difference to the four different methods is summed in quadrature and shown as orange bars. In addition to the results of this thesis previous data from Akondi *et al.*(A2 Collaboration) [30] (blue squares) are shown.

Figure 7.4: Differential cross section of $\gamma n \rightarrow K^0\Sigma^0$ in four different bins of $\cos\theta^K_{\mathrm{CM}}$ as a function of beam energy. The respective polar angle is labelled in the figure. Horizontal errors bars indicate the bin width.

of 1 550 MeV before decreasing again. In the most forward angular bin $0.2 < \cos\theta^K_{\mathrm{CM}} < 0.5$ the first rise is steeper up to a beam energy of 1 350 MeV and a second peak becomes visible at a beam energy of 1 750 MeV where the cross section rises to approximately 0.14 μb/sr.

The general agreement between the four data sets is very good. Fig. 7.4(b) shows an average calculated from the four different results. Each value is weighted with its corresponding error. In some bins the data points of the fits to the side bands and to the averaged side bands are identical (This is the case when there was no second neighbour to do the averaging, see chapter 6.3). In this case the data point is only used once. As the four results are not statistically independent, the errors of the average cross section are not smaller, but the arithmetic average of the errors of the data points used to calculate the average cross section. As a measure for the systematic uncertainty the difference to the data points used to calculate the average is summed in quadrature and also shown in Fig. 7.4(b).

The structures described before are even more visible now. Especially the rise and drop in the angular range $-0.1 < \cos\theta^K_{\mathrm{CM}} < 0.2$ and the second enhancement in the most forward angular bin become more pronounced.

Additionally shown are data from Akondi *et al.* (A2 Collaboration) [30]. This data covers the energy range from threshold to a centre-of-mass energy of 1 855 MeV which corresponds to a beam energy of 1 365 MeV[1]. As these data are split in different and smaller angular bins as the data in this thesis, sometimes more than one data set is shown. The respective angle is labelled in the figure. The data from Akondi show a steep rise over the shown energy range. The first two angular ranges of this thesis do not show this behaviour, though within the statistical uncertainty there is still reasonable agreement. Only at the highest beam energy the data from Akondi lie significantly higher. When going to more forward directions, the agreement becomes better. The data from this thesis also shows a rise. In the angular range $-0.1 < \cos\theta^K_{\mathrm{CM}} < 0.2$ there is still a small discrepancy between the data sets, but much smaller than in the first two angular ranges. In the most forward angular range $0.2 < \cos\theta^K_{\mathrm{CM}} < 0.5$ the agreement is very good. A closer look at the differences will be taken in chapter 7.4.

Systematic uncertainties

For a better readability Fig. 7.4(a) shows only statistical errors. In Fig. 7.5 the systematic uncertainties are shown for the different fitting techniques using Roofit and side band fits. The systematic uncertainties are divided into the *scaling* uncertainties, which scale the entire cross section without changing the shape, and the *fitting* uncertainties which allow every data point to move individually.

The scaling uncertainties are summarized in table 7.1. The uncertainty on photon flux, target length, beam energy and triggers are reaction independent, the corresponding values were determined in Ref. [55] and assumed to be the same here. All other uncertainties are specific to this analysis. The systematic uncertainties of π^0 identification, decay γ identification, selection of the missing (Σ^0) mass and charged particle identification are estimated by varying the selection cuts of the respective analysis step and comparing the resulting K^0_S yield normalized by reconstruction efficiency. To determine the systematic uncertainty of the subtraction of the hydrogen background, the systematic uncertainty of the hydrogen data set is calculated, which is the quadratic sum of the previous mentioned scaling uncertainties and then scaled by luminosity.

---

[1] To correctly determine the centre-of-mass energy W the Fermi momentum of the target particle needs to be known event by event. As this is not possible, this thesis uses the beam energy E_γ instead. Where E_γ and W have to be compared the target is assumed at rest.

Source	% error
Photon flux	4
Target length	1
Beam energy calibration	1
Modelling of hardware triggers	1
π^0 identification	3
$\Sigma^0 \to \gamma\Lambda$ identification	6
Selection of the missing (Σ^0) mass	3
Charged particle identification	4
Subtraction of hydrogen background	5
$K_S^0\Lambda$ subtraction	1
Summed in quadrature	11

Table 7.1: Sources and values of systematic (scaling) uncertainties.

The systematic uncertainty of the $K_S^0\Lambda$ subtraction was estimated from the systematic uncertainty[2] of the $\gamma p \to K_S^0\Lambda$ cross section. The normalized K_S^0 yield can be calculated to

$$\text{normalized yield} = \frac{\text{yield}_{K\Sigma} + \text{yield}_{K\Lambda}}{RE_{K\Sigma} \cdot F \cdot \rho \cdot \Delta\Omega}. \tag{7.4}$$

From Eqn. 7.2 follows:

$$\text{normalized yield} = \frac{\text{yield}_{K\Sigma}}{RE_{K\Sigma} \cdot F \cdot \rho \cdot \Delta\Omega} + \frac{\frac{d\sigma_{K^0\Lambda}}{d\Omega} \cdot RE_{K^0\Lambda} \cdot F \cdot \rho \cdot \Delta\Omega}{RE_{K\Sigma} \cdot F \cdot \rho \cdot \Delta\Omega}, \tag{7.5}$$

which can also be written as

$$\text{normalized yield} = \frac{d\sigma_{K\Sigma}}{d\Omega} + \frac{d\sigma_{K\Lambda}}{d\Omega} \cdot \frac{RE_{K\Lambda}}{RE_{K\Sigma}}. \tag{7.6}$$

The first summand is the $\gamma n \to K^0\Sigma^0$ cross section, the second summand is the contamination from $\gamma n \to K^0\Lambda$ that is subtracted. Its systematic uncertainty is calculated as

$$\Delta_{\text{systematic}}\left(\frac{d\sigma_{K\Lambda}}{d\Omega} \cdot \frac{RE_{K\Lambda}}{RE_{K\Sigma}}\right) = \Delta_{\text{systematic}}\left(\frac{d\sigma_{K\Lambda}}{d\Omega}\right) \cdot \frac{RE_{K\Lambda}}{RE_{K\Sigma}} \tag{7.7}$$

$\Delta_{\text{systematic}}\left(\frac{d\sigma_{K\Lambda}}{d\Omega}\right)$ is the systematic uncertainty given in Ref. [54] and of the order of 10%. Multiplied with the ratio of reconstruction efficiencies $\frac{RE_{K\Lambda}}{RE_{K\Sigma}}$ the systematic uncertainty of the $K_S^0\Lambda$ subtraction is about 1%.

The fitting uncertainty is determined for each data point as the difference between the cross section values determined from the different background descriptions to the average value shown in Fig. 7.4(b).

---

[2] The statistical uncertainties are already included when subtracting the $\gamma n \to K^0\Lambda$ contribution (chapter 7.2).

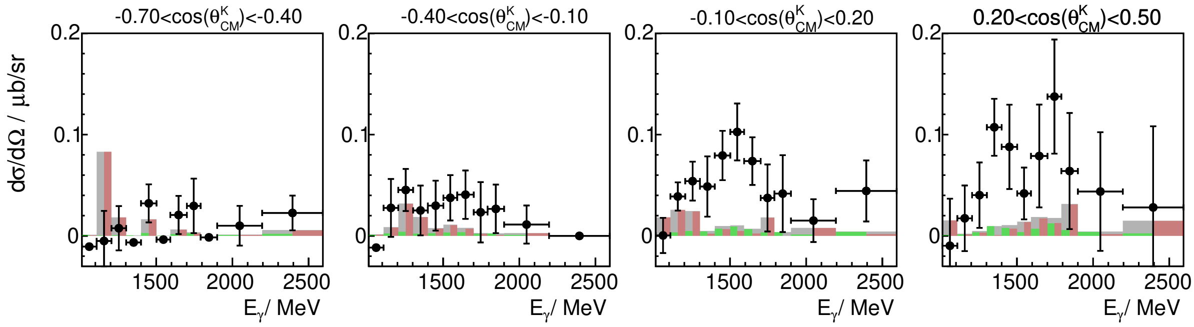

(a) $\gamma n \to K^0\Sigma^0$ differential cross section determined using PS background description.

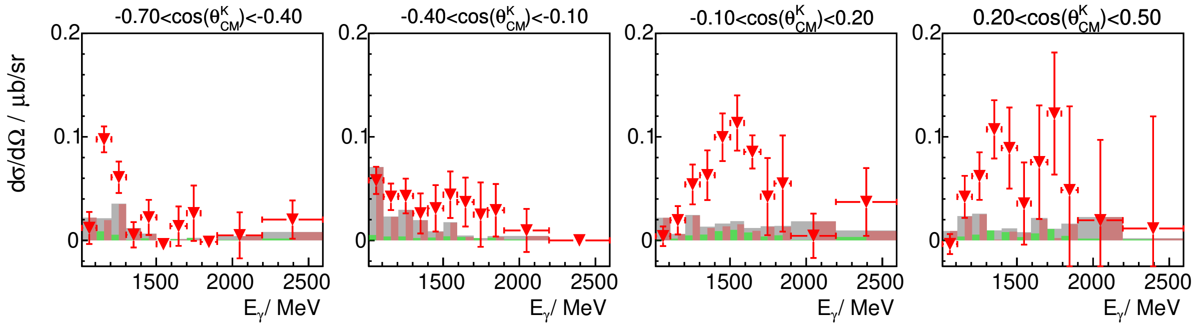

(b) $\gamma n \to K^0\Sigma^0$ differential cross section determined using RD background description.

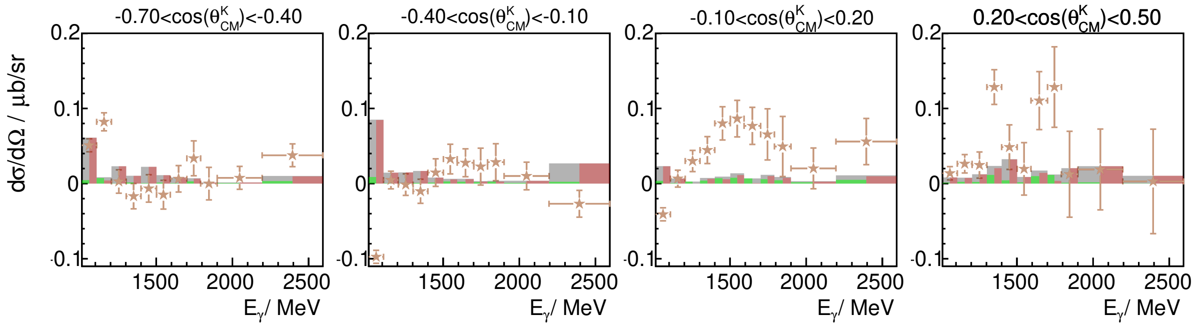

(c) $\gamma n \to K^0\Sigma^0$ differential cross section determined using fits to the side bands.

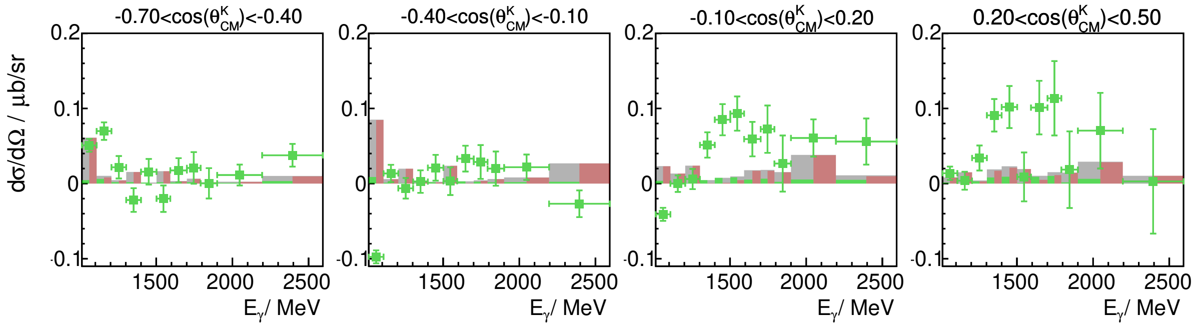

(d) $\gamma n \to K^0\Sigma^0$ differential cross section determined using fits to averaged side bands.

Figure 7.5: $\gamma n \to K^0\Sigma^0$ differential cross section with systematic uncertainties. On the left half of each bin, the scaling uncertainties are shown as green bars. On the right half, the fitting uncertainties are shown as red bars. The quadratic sum of both is shown as grey bars over the full bin width.

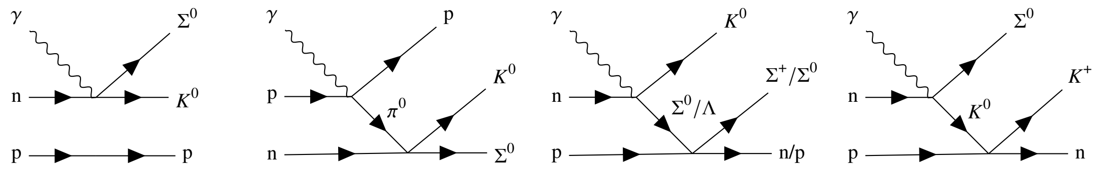

(a) Quasi-free reaction without interacting with the spectator proton.

(b) Final state is produced via an intermediate π^0.

(c) Σ^0/Λ interacting with spectator proton.

(d) K^0 interacting with the spectator proton.

Figure 7.6: Diagrams of possible interactions affecting the extracted signal yield. Shown is the quasi-free production without any interaction with the spectator nucleon (7.6(a)) and three lowest order diagrams of final-state-interaction (7.6(b) - 7.6(d)).

In Fig. 7.5 the scaling uncertainty is shown as grey bars on the left half of each bin, the fitting uncertainty is shown as red bars on the right half. The quadratic sum of both is shown as blue bars over the full bin.

Final-State-Interaction (FSI)

Final-State-Interaction (FSI) could potentially affect a cross section measurement on a deuterium target, by the final state particles interacting with the spectator nucleon. This can increase or decrease the measured cross section depending on whether FSI produces the final state that is detected or the interaction with the spectator nucleon causes the expected final state to change to a different one. Fig. 7.6 shows first order diagrams of possible interactions which could affect the $\gamma n \rightarrow K^0\Sigma^0$ cross section.

A full calculation of possible FSI would lead too far for this thesis, however an estimation of the size of FSI can be made by looking at Isospin partner reactions. Studies to FSI in K^+ photoproduction on the deuteron [56, 57] show effects mostly below 10% of the respective cross sections[3]. Effects of similar size can be assumed for this reaction. With the available statistical accuracy such FSI can not be resolved. At this point FSI is considered negligible for this work, once statistics is improved a more detailed investigation of FSI may become necessary.

7.4 Comparing experimental data and theory

In this chapter the measured $\gamma n \rightarrow K^0\Sigma^0$ differential cross section is compared to two different theoretical calculations. For the threshold region isobar-model predictions for the differential cross section of $\gamma n \rightarrow K^0\Sigma^0$ were made by Mart [30, 53]. For the beam energy range between approximately 1 300 MeV and 2 100 MeV a peak structure originating from vector meson-baryon interaction was predicted by Ramos and Oset [28] in the total cross section.

Fig. 7.7(a) shows the data of this thesis in the four beam energy bins closest to threshold as a function of $\cos\theta^K_{\mathrm{CM}}$. Also plotted in Fig. 7.7(a) is the data from Akondi *et al.* (A2 Collaboration) together with the respective predictions as given in Ref. [30]. The energy bins used in this thesis are larger than the ones used by Akondi *et al.*, therefore several of those data sets are shown in one plot. The data of

---

[3] Where the relative effect is larger, the absolute value is very small.

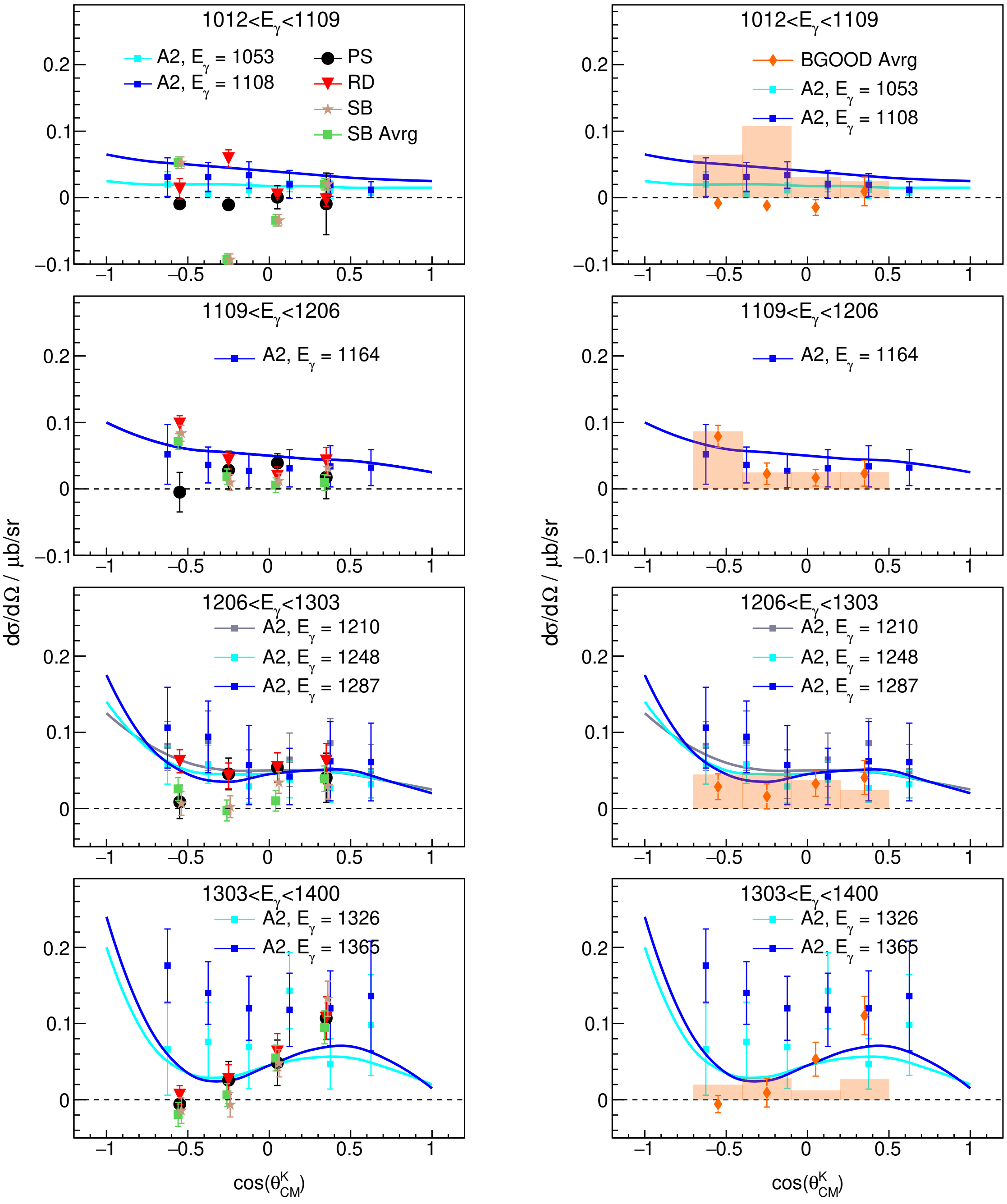

(a) Results of four different methods to fit to the data (PS black circles, RD red triangles, side band fits brown stars, fits to averaged side bands green squares).

(b) Error weighted average of the four different extraction methods shown in Fig. 7.7(a). The difference to the four different methods is summed in quadrature and shown as orange bars.

Figure 7.7: $\gamma n \rightarrow K^0\Sigma^0$ cross section as a function of $\cos\theta^K_{\mathrm{CM}}$ in the first four energy bins from threshold. Plotted are the results from this thesis together with data from Akondi *et al.*(A2 Collaboration) [30] (blue squares) and theoretical predictions by Mart [30, 53] (blue lines). Due to a different binning, several data sets from Akondi *et al.* and the respective predictions are plotted together in the larger energy bins used in this thesis, the respective energies are labelled in each plot. All energies are given in MeV.

this thesis and the data from Akondi *et al.* are generally in good agreement with the exception of the highest energy bin. The theoretical calculation from Mart also describes the data generally well. In the highest energy bin the agreement between the data of this thesis and the prediction is significantly better than between the data from Akondi *et al.* and the respective prediction.

The general shape of the data is reflected in the predictions even though not all data points agree within the statistical uncertainty. Especially in the first energy bin directly at threshold the fluctuations from point to point are large. The agreement between experimental results and prediction is best for the RD background description. The two side band fit data sets and the PS data set contain some data points that are negative. The fits leading to these data points have difficulties describing the background directly at threshold. This was explained in chapters 6.1 and 6.3, and is reflected in the systematic (fitting) uncertainty. These difficulties in the fitting disappear when going to higher beam energies. With increasing beam energy the agreement between the four data sets is getting much better, and the predictions describe the data very well.

Fig. 7.7(b) shows the error weighted average of the cross section together with the data from Akondi *et al.*(A2 Collaboration) and the respective predictions from Mart.

Again, the general shape of measured cross section and prediction agree, though not all data points agree with the predictions individually within the statistical uncertainty. The agreement between the data from Akondi *et al.* and the average cross section from this thesis is within the statistical uncertainty for most energies. Directly at threshold the average value is dominated by the negative data points due to their small statistical error. Considering the systematic uncertainties however, the average cross section is in reasonable agreement with the data from Akondi *et al.* also in this energy range.

The comparison with the results from Akondi *et al.*(A2 Collaboration) [30] shows a good agreement and confirms that determination and normalization of the $\gamma n \to K^0\Sigma^0$ yield work well. The important aim of this thesis is to extend the measurement across the K^* threshold and to test whether the peak predicted by Ramos and Oset [28] can be observed in the measured cross section. Fig. 7.8 shows the most forward angular bin $0.2 < \cos\theta^K_{\mathrm{CM}} < 0.5$. The upper plot shows the results of the four different methods to describe and fit background and signal. The lower plot shows the averaged cross section. In both plots the predicted total cross section is overlayed scaled to approximately match the height of the data. All four different methods to describe and fit background and signal are consistent within the statistical uncertainty and indeed show a peak at 1 750 MeV, as does the average cross section. However, given the limited statistics this peak being a statistical fluctuation can not be ruled out entirely.

Nevertheless, within the statistical precision, position and width of the measured peak is consistent with the enhancement predicted by Ramos and Oset. It has to be noted, that the prediction is a total cross section. A theoretical calculation for the differential cross section as a function of $\cos\theta^K_{\mathrm{CM}}$ is unfortunately not yet available. Though a final claim for this peak being actually the one predicted can not yet be made, there is a remarkable agreement between measured data and prediction. Similar to the cusp in $\gamma p \to K^0\Sigma^+$, which is more pronounced in forward direction, this peak can only be observed in the most forward accessible bin. It is possible, the peak also becomes more pronounced in more forward directions.

The model, that predicts a peak in the $\gamma n \to K^0\Sigma^0$ cross section to originate from interferences between $K^*\Lambda$ and $K^*\Sigma$ intermediate states, magnified by the $N^*(2030)$, a vector meson-baryon dynamically generated $K^*\Sigma$ resonance, is the same model that predicted the P_C states in the c-quark sector observed at LHCb [7–9]. The observation of this peak is a strong indication for such

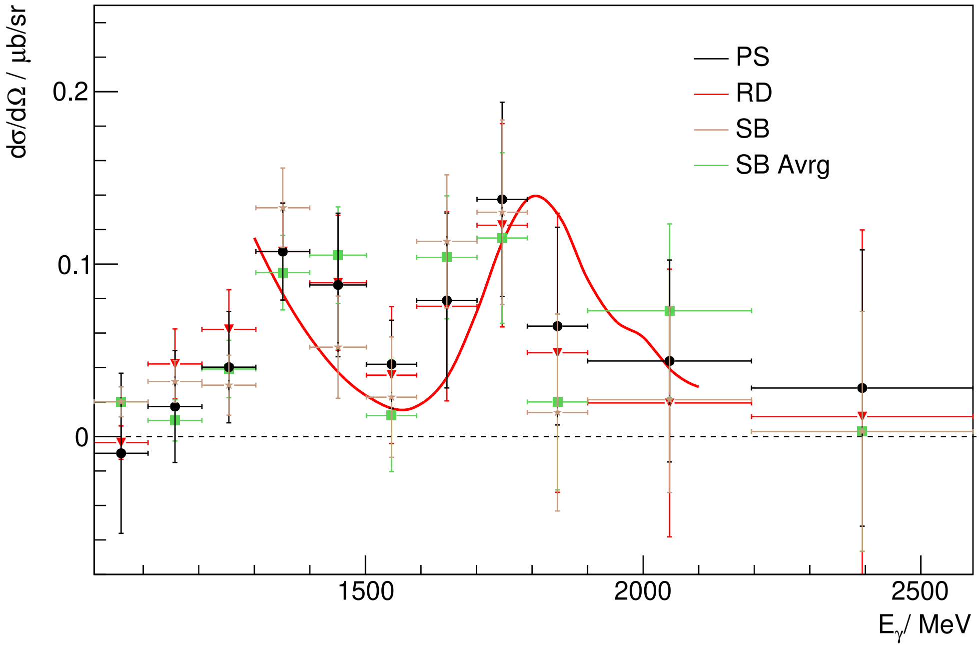

(a) Results of four different methods to fit to the data (PS black circles, RD red triangles, side band fits brown stars, fits to averaged side bands green squares).

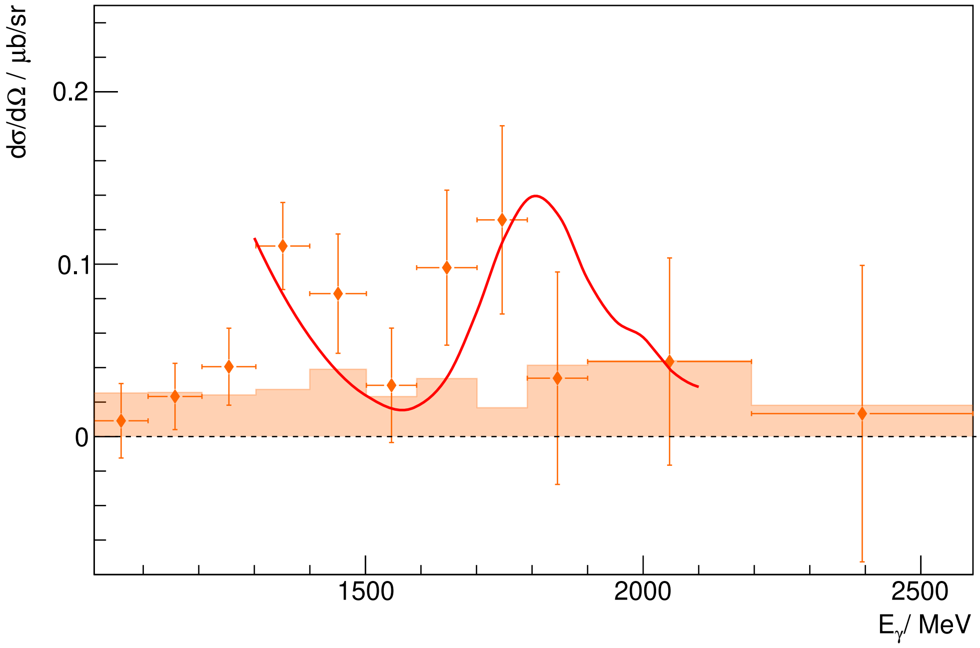

(b) Error weighted average of the four different extraction methods shown in Fig. 7.7(a). The difference to the four different methods is summed in quadrature and shown as orange bars.

Figure 7.8: $\gamma n \rightarrow K^0\Sigma^0$ differential cross section in the angular range $0.2 < \cos\theta^K_{\mathrm{CM}} < 0.5$. Overlayed is the predicted total cross section from Ramos and Oset [28] scaled to approximately match the height of the data (red line). The zero value is indicated as a dashed line. Horizontal errors bars indicate the bin width.

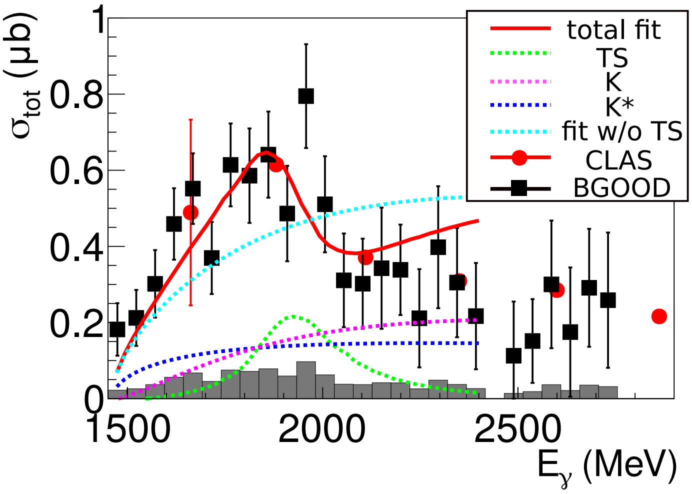

Figure 7.9: $\gamma p \longrightarrow K^+\Lambda(1405)$ cross section. The superimposed lines are results from the model of E. Wang *et al.* [58] fitted to the CLAS data. The red line is the fit including production via K^* and K exchange and via the triangle singularity mechanism shown in Fig. 7.10. The cyan dashed line is a fit without including the triangle singularity mechanism. The figure was taken from [59].

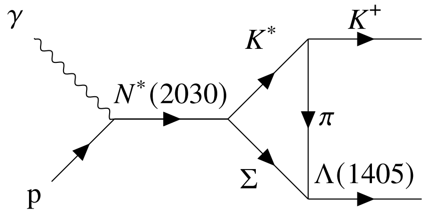

Figure 7.10: Possible diagram of $\Lambda(1405)$ photo-production via a triangle process [58].

meson-baryon type pentaquark resonances to exist in the s-quark sector.

Further support for the observed structure to be real seems to come from a different side, namely the reaction $\gamma p \longrightarrow K^+\Lambda(1405)$ [59]. This cross section shows a similar drop as in the reaction $\gamma p \longrightarrow K^0\Sigma^+$ (Fig. 7.9). It can be explained with a contribution from a triangle diagram (Fig. 7.10) which is fed by the very same $N^*(2030)$ vector meson-baryon dynamically generated $K^*\Sigma$ resonance [58], which would be responsible for the peak observed in this thesis. Included in Fig. 7.9 are calculations with and without the triangle singularity. The one including a contribution from $N^*(2030)$ describes the data much better. The necessity of the $N^*(2030)$ to describe the $\gamma p \longrightarrow K^+\Lambda(1405)$ cross section is a strong hint, that the peak observed in the $\gamma n \longrightarrow K^0\Sigma^0$ cross section originates from an interference of $K^*\Lambda$ and $K^*\Sigma$ intermediate states, which is magnified by the same $N^*(2030)$ resonance.

To finally establish this, more statistics are essential. Only by reducing the statistical uncertainty it is possible to verify the existence of the observed peak and allow a more accurate measurement of position and width. How much more statistic is needed can be determined by estimating the significance of the observed peak. By describing the shape of the cross section underneath the peak the excess can be calculated. In Fig. 7.11 three different shapes are fitted to the average cross section in the angular bin $0.2 < \cos\theta^K_{CM} < 0.5$, excluding the two data points at 1 647 MeV and 1 746 MeV. These shapes are a phase space distribution determined from MC simulation, a constant line and an exponential function, similar to the shape described by the prediction by Ramos and Oset[28]. For all three shapes the significance of the peak is calculated, by calculating the probability for the two data points at 1 647 MeV and 1 746 MeV to be shifted to lie on the fitted shapes. Assuming the error bars shown in Fig. 7.11 are 1σ, the probability can be given as multiples of σ. It ranges from 2.9σ (exponential) over 2.3σ (constant line) to 1.8σ (phase space). To speak of evidence of this peak, at

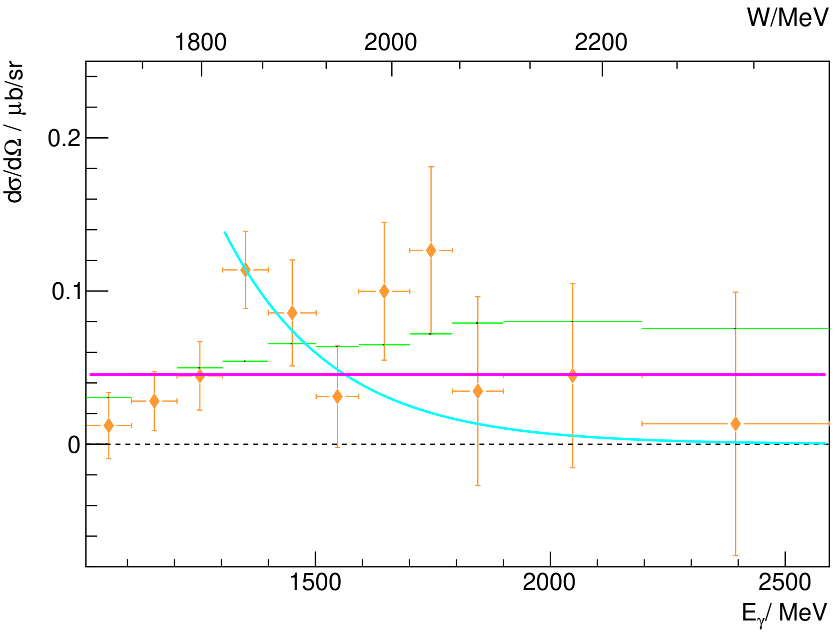

Figure 7.11: Different shapes fitted to the average cross section to estimate the significance of the peak at 1 700 MeV. Green: phase space distribution determined from MC simulation, pink: constant line, blue: exponential.

least 3σ are necessary[4]. Depending on the model at least doubling the statistics, better tripling it, is necessary to reach this level of significance.

Additionally the covered angular range has to be extended to more forward directions. The cusp observed in the $\gamma p \longrightarrow K^0\Sigma^+$ cross section was strongest in forward direction. Also in the $\gamma n \longrightarrow K^0\Sigma^0$ cross section measured in this thesis, the peak could only be observed in the most forward accessible bin. It is possible, that it becomes more pronounced in more forward direction. To access the angular region $\cos\theta^K_{\mathrm{CM}}>0.5$ the charged decay of the $K^0_S \longrightarrow \pi^+\pi^-$ will be helpful. In contrast to the photons of the neutral decay $K^0_S \longrightarrow \pi^0\pi^0 \longrightarrow (\gamma\gamma)(\gamma\gamma)$ the charged pions can be observed in the Forward Spectrometer and the intermediate detectors. Once the detector setup is completed and the two missing detectors (MWPC and MRPC) are fully operational it will be possible to detect and identify charged particles over the full angular range and measure a total $\gamma n \longrightarrow K^0\Sigma^0$ cross section.

At this stage a theoretical calculation of the $\gamma n \longrightarrow K^0\Sigma^0$ differential cross section would be interesting. Though the peak predicted for the total cross section is consistent with the observation in the differential cross section, it could only be observed in one angular bin. A theoretical prediction of the cross section as a function of angle would help to understand this and make it possible to not only compare position and width of the observed enhancement, but also the absolute value of the differential cross section.

---

[4] Conventionally 3σ are required for evidence, 5σ are called a discovery.

CHAPTER 8

Summary

History of physics is characterised by the search for structures and the rules which these structures follow. Be it the internal structure of an atom or the quark content of hadrons. One of the biggest successes is the standard model of particle physics. This model can describe most observations in particle and hadron physics. One aspect of it is the strong colour interaction among the quarks as the building blocks of matter. Prior to the standard model already, the constituent quark model proved successful to order the vast amount of hadronic states based on flavour symmetry. However in the past years more and more hadronic states have been discovered that appear not to follow the rules of the constituent quark model, but can be explained by introducing multi-quark structures beyond the quark content of qqq or $q\overline{q}$.

So far these unconventional states have only been observed in the charm and bottom quark sector. Further investigation is necessary to understand their nature, different models including compact colour bound objects or meson-meson or meson-baryon type systems are employed to describe their inner structure. However, if the underlying structure principle was meson-meson or meson-baryon interaction, this could work in the strange quark sector as well as in the charm and bottom quark sector.

This is supported by recent results to the internal structure of the $\Lambda(1405)$. On its discovery it was already considered a molecule of a kaon and a nucleon. With the invention of the quark model it was explained as an excited state of a baryon with quark content uds. Newer results show it must have a large contribution of a $\overline{K}N$ structure [10], indicating that meson-baryon type “pentaquark” structures exist in the strange quark sector too.

Actually the same theoretical model, that used meson-baryon interaction to predict the LHCb pentaquark candidates [29], was extended to describe a cusp in the $\gamma p \to K^0\Sigma^+$ cross section [11, 28]. The very same model predicts an enhancement in the cross section of $\gamma n \to K^0\Sigma^0$ [28] in the energy region of the K^* threshold. An observation of this enhancement would be a smoking gun signal for such an unconventional state to exist also in the strange quark sector.

In this thesis the differential cross section of the reaction $\gamma n \to K^0\Sigma^0$ was determined. The signal yield was extracted from a deuterium data set by applying different selection cuts. Background from reactions on the proton was removed by repeating the analysis with a hydrogen data set and subtracting the resulting spectrum. Fermi motion was taken into account and luminosity properly scaled. The remaining background was removed by fitting to the $2\pi^0$ invariant mass spectrum. The extracted K^0_S yield contained a contribution from $\gamma n \to K^0\Lambda$, which was determined from the known $\gamma n \to K^0\Lambda$ [54] cross section and subtracted. Finally the differential cross section was determined from threshold up to a beam energy of 2 594 MeV in four angular bins from $\cos\theta_{\mathrm{CM}}^{K}= -0.7$ to $\cos\theta_{\mathrm{CM}}^{K}= 0.5$.

In backward direction the cross section shows a small rise directly at threshold. Above 1 300 MeV it is mostly flat and remains below 0.05 μb/sr. In the second angular bin the cross section is mostly flat and below 0.1 μb/sr. When going more forward, the cross section rises to 0.1 μb/sr before dropping again. In the most forward accessible angular bin ($0.2 < \cos\theta_{\mathrm{CM}}^{K} < 0.5$) a peak becomes visible at 1 750 MeV, i.e. in the region of the K^* threshold, where the cross section rises to approximately 0.14 μb/sr. At threshold the measured differential cross section is compared to existing data from Akondi *et al.*(A2 Collaboration) [30] and theoretical predictions from T. Mart [53]. Within the statistical accuracy the two data sets and the prediction agree.

Due to the limited statistics it can not be strictly ruled out, the enhancement observed in the angular bin ($0.2 < \cos\theta_{\mathrm{CM}}^{K} < 0.5$) is caused by statistical fluctuation. However, this peak was compared to the structure predicted by Oset and Ramos [28]. Position and width agree within the statistical uncertainty. It has to be noted, that the prediction is a total cross section that was compared to a differential cross section. Unfortunately a theoretical prediction of the differential cross section is not yet available. At this stage no final claim can be made, but the agreement between data and prediction is very good, which is a strong indication for the presence of a vector meson-baryon dynamically generated $K^*\Sigma$ resonance, the $N^*(2030)$.

This is supported by recent results for the production mechanism of the before mentioned $\Lambda(1405)$. Calculations have shown, that a triangle singularity fed by the very same vector meson-baryon dynamically generated resonance $N^*(2030)$ is necessary to describe the shape of the $\gamma p \rightarrow K^+\Lambda(1405)$ cross section [58, 59].

In analogy to the P_C states observed at LHCb, this resonance can not be explained with the conventional quark model, but it is an indication for unconventional hadrons beyond the quark content of qqq or $q\overline{q}$ in the strange quark sector.

To finally verify the observation of an enhancement in the $\gamma n \rightarrow K^0\Sigma^0$ cross section, an increase of statistics is essential. Additionally the accessible angular region should be extended to more forward regions. The cusp in the $\gamma p \rightarrow K^0\Sigma^+$ was strongest in most forward direction, it is possible, the peak in the $\gamma n \rightarrow K^0\Sigma^0$ behaves similar. Once the two foreseen further tracking detectors of the BGOOD experiment (MWPC and MRPC) are fully operational this will be possible by investigating the charged decay of $K_S^0 \rightarrow \pi^+\pi^-$. In contrast to the photons of the neutral decay, which were used in this thesis, the charged particles could be observed in the intermediate detectors and the forward spectrometer, and would allow access to more forward angular regions. Furthermore, a theoretical calculation of the differential cross section would be helpful to understand in which angular regions the predicted peak is actually expected.

Bibliography

[1] J. J. Thomson, *Cathode rays*, Phil. Mag. Ser. 5 **44**, 1897 293 (cit. on p. 1).

[2] E. Rutherford,
The scattering of alpha and beta particles by matter and the structure of the atom,
Phil. Mag. Ser. 6 **21**, 1911 669 (cit. on p. 1).

[3] N. Bohr, *On the Constitution of Atoms and Molecules*, Phil. Mag. Ser. 6 **26**, 1913 1 (cit. on p. 1).

[4] *UZH -Physik-Institut - Standard Model*, 2020, URL: `https://www.physik.uzh.ch/en/researcharea/lhcb/outreach/StandardModel.html` (visited on 26/08/2021) (cit. on p. 2).

[5] P. A. Zyla et al., *Review of Particle Physics*, PTEP **2020**, 2020 083C01 (cit. on p. 4).

[6] S.-K. Choi, S. L. Olsen et al.,
Observation of a Narrow Charmoniumlike State in Exclusive $B^{\pm} \rightarrow K^{\pm}\pi^{+}\pi^{-}J/\psi$ *Decays*,
Phys. Rev. Lett. **91**, 2003 262001,
URL: `https://link.aps.org/doi/10.1103/PhysRevLett.91.262001` (cit. on pp. 4, 8).

[7] R. Aaij et al., *Observation of* $J/\psi p$ *Resonances Consistent with Pentaquark States in* $\Lambda_b^0 \rightarrow J/\psi K^- p$ *Decays*, Phys. Rev. Lett. **115**, 2015 072001,
URL: `https://link.aps.org/doi/10.1103/PhysRevLett.115.072001`
(cit. on pp. 4, 9, 71).

[8] Burns, T. J., *Phenomenology of* $P_c(4380)^+$, $P_c(4450)^+$ *and related states*,
Eur. Phys. J. A **51**, 2015 152, URL: `https://doi.org/10.1140/epja/i2015-15152-6`
(cit. on pp. 4, 9, 71).

[9] R. Aaij et al., *Observation of a Narrow Pentaquark State,* $P_c(4312)^+$*, and of the Two-Peak Structure of the* $P_c(4450)^+$, Phys. Rev. Lett. **122**, 2019 222001,
URL: `https://link.aps.org/doi/10.1103/PhysRevLett.122.222001`
(cit. on pp. 4, 9, 71).

[10] J. M. M. Hall et al.,
Lattice QCD Evidence that the $\Lambda(1405)$ *Resonance is an Antikaon-Nucleon Molecule*,
Phys. Rev. Lett. **114**, 2015 132002, arXiv: `1411.3402 [hep-lat]` (cit. on pp. 4, 75).

[11] R. Ewald et al.,
Anomaly in the $K_S^0\Sigma^+$ *photoproduction cross section off the proton at the* K^* *threshold*,
Phys. Lett. B **713**, 2012 180, arXiv: `1112.0811 [nucl-ex]` (cit. on pp. 4, 10, 11, 75).

[12] S. L. Olsen, *A New Hadron Spectroscopy*, Front. Phys. (Beijing) **10**, 2015 121,
arXiv: `1411.7738 [hep-ex]` (cit. on pp. 7, 9).

[13] B. Aubert et al., *Observation of the decay* $B \to J/\psi\eta K$ *and search for* $X(3872) \to J/\psi\eta$, Phys. Rev. Lett. **93**, 2004 041801, arXiv: `hep-ex/0402025` (cit. on p. 8).

[14] R. Aaij et al., *Observation of* $X(3872)$ *production in* pp *collisions at* $\sqrt{s} = 7$ *TeV*, Eur. Phys. J. C **72**, 2012 1972, arXiv: `1112.5310 [hep-ex]` (cit. on p. 8).

[15] K. Toms, *The* $X(3872)$ *and the search for its bottomonium counterpart at the LHC*, PoS **ICHEP2016**, 2016 641 (cit. on p. 8).

[16] E. S. Swanson, *Short range structure in the X(3872)*, Phys. Lett. B **588**, 2004 189, arXiv: `hep-ph/0311229` (cit. on p. 8).

[17] C.-Y. Wong, *Molecular states of heavy quark mesons*, Phys. Rev. C **69**, 2004 055202, arXiv: `hep-ph/0311088` (cit. on p. 8).

[18] F. E. Close and P. R. Page, *The* D^{*0} *anti-*D^0 *threshold resonance*, Phys. Lett. B **578**, 2004 119, arXiv: `hep-ph/0309253` (cit. on p. 8).

[19] N. A. Tornqvist,
Comment on the narrow charmonium state of Belle at 3871.8-MeV as a deuson, 2003, arXiv: `hep-ph/0308277` (cit. on p. 8).

[20] L. Maiani et al., *Diquark-antidiquarks with hidden or open charm and the nature of X(3872)*, Phys. Rev. D **71**, 2005 014028, arXiv: `hep-ph/0412098` (cit. on p. 8).

[21] H.-X. Chen et al., *The hidden-charm pentaquark and tetraquark states*, Phys. Rept. **639**, 2016 1, arXiv: `1601.02092 [hep-ph]` (cit. on p. 9).

[22] Y.-R. Liu et al., *Pentaquark and Tetraquark states*, Prog. Part. Nucl. Phys. **107**, 2019 237, arXiv: `1903.11976 [hep-ph]` (cit. on p. 9).

[23] S. K. Choi et al., *Observation of a resonance-like structure in the* $\pi^{\pm}\psi'$ *mass distribution in exclusive* $B \to K\pi^{\pm}\psi'$ *decays*, Phys. Rev. Lett. **100**, 2008 142001, ed. by D. Son and S. K. Oh, arXiv: `0708.1790 [hep-ex]` (cit. on p. 9).

[24] R. Aaij et al., *Observation of the resonant character of the* $Z(4430)^-$ *state*, Phys. Rev. Lett. **112**, 2014 222002, arXiv: `1404.1903 [hep-ex]` (cit. on p. 9).

[25] Z. Q. Liu et al.,
Study of $e^+e^- \to \pi^+\pi^- J/\Psi$ *and Observation of a Charged Charmoniumlike State at Belle*, Phys. Rev. Lett. **110**, 2013 252002, [Erratum: Phys.Rev.Lett. 111, 019901 (2013)], arXiv: `1304.0121 [hep-ex]` (cit. on p. 9).

[26] M. Ablikim et al.,
Observation of a Charged Charmoniumlike Structure in $e^+e^- \to \pi^+\pi^-$ *J/ψ at* $\sqrt{s}$ *=4.26 GeV*, Phys. Rev. Lett. **110**, 2013 252001, arXiv: `1303.5949 [hep-ex]` (cit. on p. 9).

[27] H. Schmieden, *private communication* (cit. on p. 9).

[28] A. Ramos and E. Oset, *The role of vector-baryon channels and resonances in the* $\gamma p \to K^0\Sigma^+$ *and* $\gamma n \to K^0\Sigma^0$ *reactions near the* $K^*\Lambda$ *threshold*, Phys. Lett. B **727**, 2013 287, arXiv: `1304.7975 [nucl-th]` (cit. on pp. 10, 11, 61, 69, 71–73, 75, 76).

[29] J.-J. Wu et al., *Prediction of narrow* N^* *and* Λ^* *resonances with hidden charm above 4 GeV*, Phys. Rev. Lett. **105**, 2010 232001, arXiv: `1007.0573 [nucl-th]` (cit. on pp. 11, 75).

[30] C. Akondi et al., *Experimental study of the* $\gamma p \to K^0\Sigma^+$*,* $\gamma n \to K^0\Lambda$*, and* $\gamma n \to K^0\Sigma^0$ *reactions at the Mainz Microtron*, Eur. Phys. J. A **55**, 2019 202, arXiv: `1811.05547 [nucl-ex]` (cit. on pp. 11, 61, 65, 66, 69–71, 76).

[31] S. Alef et al., *The BGOOD experimental setup at ELSA*, Eur. Phys. J. A **56**, 2020 104, arXiv: `1910.11939 [physics.ins-det]` (cit. on pp. 13, 17, 18).

[32] W. Hillert, *The Bonn electron stretcher accelerator ELSA: Past and future*, Eur. Phys. J. A **28S1**, 2006 139, ed. by H. Arenhoevel et al. (cit. on p. 14).

[33] W. Hillert et al., *Beam and spin dynamics in the fast ramping storage ring ELSA: Concepts and measures to increase beam energy, current and polarization*, EPJ Web Conf. **134**, 2017 05002, ed. by F. Klein, U.-G. Meißner and U. Thoma (cit. on p. 14).

[34] Andreas Bella, *Linearly polarised photon beams at the BGO-OD experiment at ELSA*, PhD thesis: Rheinische Friedrich-Wilhelms-Universität Bonn, 2016, URL: `http://hdl.handle.net/20.500.11811/6897` (cit. on pp. 15, 16).

[35] B.-E. Reitz, *Construction of an additional hodoscope for the BGO-OD experiment consisting of scintillator fibres (ARGUS) together with simple* π^0 *analysis*, MA thesis: Universität Bonn, 2015 (cit. on p. 16).

[36] S. Alef, *Development of a scintillating fibre hodoscope (ARGUS) for the tagging system of the BGO-OD experiment*, MA thesis: Universität Bonn, 2015 (cit. on p. 16).

[37] F. Ghio et al., *The GRAAL high resolution BGO calorimeter and its energy calibration and monitoring system*, Nucl. Instrum. Meth. A **404**, 1998 71, arXiv: `physics/9709027` (cit. on p. 16).

[38] G. Scheluchin, *Meson photoproduction on the proton using the BGO-OD detector complemeted by a new Scintillating Ring (SciRi)*, MA thesis: Universität Bonn, 2015 (cit. on p. 18).

[39] Sabine Böse, *Aufbau und Test eines Szintillationsfaser-Detektors für das neue Vorwärtsspektrometer an ELSA*, PhD thesis: Rheinische Friedrich-Wilhelms-Universität Bonn, 2016, URL: `http://hdl.handle.net/20.500.11811/6728` (cit. on p. 18).

[40] T. Frese, *In situ field measurement of the Open Dipole magnet at the BGO-OD experiment*, MA thesis: Universität Bonn, 2012 (cit. on p. 20).

[41] D. Hammann, *Test und Inbetriebnahme der Prototyp-Driftkammer für das B1-Spektrometer*, MA thesis: Universität Bonn, 2008 (cit. on p. 20).

[42] T. Schwan, *Test und Inbetriebnahme der Driftkammern für das BGO-OD-Spektrometer*, MA thesis: Universität Bonn, 2010 (cit. on p. 20).

[43] O. Freyermuth, *Studies of* ω *Photoproduction off Proton at the BGO-OD Experiment*, PhD thesis: Rheinische Friedrich-Wilhelms-Universität Bonn, 2017, URL: `http://hdl.handle.net/20.500.11811/7263` (cit. on pp. 20, 23).

[44] R. Brun and F. Rademakers, *ROOT: An object oriented data analysis framework*, Nucl. Instrum. Meth. A **389**, 1997 81, ed. by M. Werlen and D. Perret-Gallix (cit. on p. 23).

[45] Georg Scheluchin, *Λ(1405) photoproduction with the BGO-OD experiment*, PhD thesis: Rheinische Friedrich-Wilhelms-Universität Bonn, 2020 (cit. on pp. 23, 61).

[46] J. Allison et al., *Recent developments in Geant4*, Nucl. Instrum. Meth. A **835**, 2016 186 (cit. on p. 23).

[47] M. Tanabashi et al., *Review of Particle Physics*, Phys. Rev. D **98**, 2018 030001, URL: `https://link.aps.org/doi/10.1103/PhysRevD.98.030001` (cit. on pp. 25, 29).

[48] M. Lacombe et al., *Parametrization of the Paris n n Potential*, Phys. Rev. C **21**, 1980 861 (cit. on pp. 25, 26, 38).

[49] R. Machleidt, *The High precision, charge dependent Bonn nucleon-nucleon potential (CD-Bonn)*, Phys. Rev. C **63**, 2001 024001, arXiv: `nucl-th/0006014` (cit. on pp. 25, 26).

[50] W. Verkerke and D. P. Kirkby, *The RooFit toolkit for data modeling*, eConf **C0303241**, 2003 MOLT007, ed. by L. Lyons and M. Karagoz, arXiv: `physics/0306116` (cit. on p. 41).

[51] A. Kolmogorov, *Sulla determinazione empirica di una legge di distribuzione*, Giornale dell Istituto Italiano degli Attuari **4**, 1933 8391 (cit. on p. 51).

[52] *"Root Reference Guide, KolmogorovTest"*, 2021, URL: `https://root.cern.ch/doc/master/classTH1.html#aeadcf087afe6ba203bcde124cfabbee4` (visited on 12/03/2021) (cit. on p. 52).

[53] T. Mart, *Electromagnetic production of $K\Sigma$ on the nucleon near threshold*, Phys. Rev. C **90**, 2014 065202, URL: `https://link.aps.org/doi/10.1103/PhysRevC.90.065202` (cit. on pp. 61, 69, 70, 76).

[54] N. Compton et al., *Measurement of the differential and total cross sections of the $\gamma d \to K^0\Lambda(p)$ reaction within the resonance region*, Phys. Rev. C **96**, 2017 065201, URL: `https://link.aps.org/doi/10.1103/PhysRevC.96.065201` (cit. on pp. 62, 67, 75).

[55] S. Alef et al., *$K^+\Lambda$ photoproduction at forward angles and low momentum transfer*, Eur. Phys. J. A **57**, 2021 80, arXiv: `2006.12350 [nucl-ex]` (cit. on p. 66).

[56] A. Salam and H. Arenhovel, *Interaction effects in K+ photoproduction on the deuteron*, Phys. Rev. C **70**, 2004 044008, arXiv: `nucl-th/0407098` (cit. on p. 69).

[57] K. Miyagawa et al., *Polarization observables in exclusive kaon photoproduction on the deuteron*, Phys. Rev. C **74**, 2006 034002, arXiv: `nucl-th/0608052` (cit. on p. 69).

[58] E. Wang et al., *Role of a triangle singularity in the $\gamma p \to K^+\Lambda(1405)$ reaction*, Phys. Rev. C **95**, 2017 015205, arXiv: `1610.07117 [hep-ph]` (cit. on pp. 73, 76).

[59] G. Scheluchin et al., *Photoproduction of $K^+\Lambda(1405) \to K^+\pi^0\Sigma^0$ extending to forward angles and low momentum transfer*, 2021, arXiv: `2108.12235 [nucl-ex]` (cit. on pp. 73, 76).

APPENDIX A

Roofit Fits

On the following pages all Roofit fits to the $2\pi^0$ invariant mass spectrum are shown that were not plotted in chapter 6.1. Two different methods to describe the background were used, either simulated background channels, or real data with relaxed cuts. Each spectrum is fitted twice, once with background and signal and once with the background distribution only.

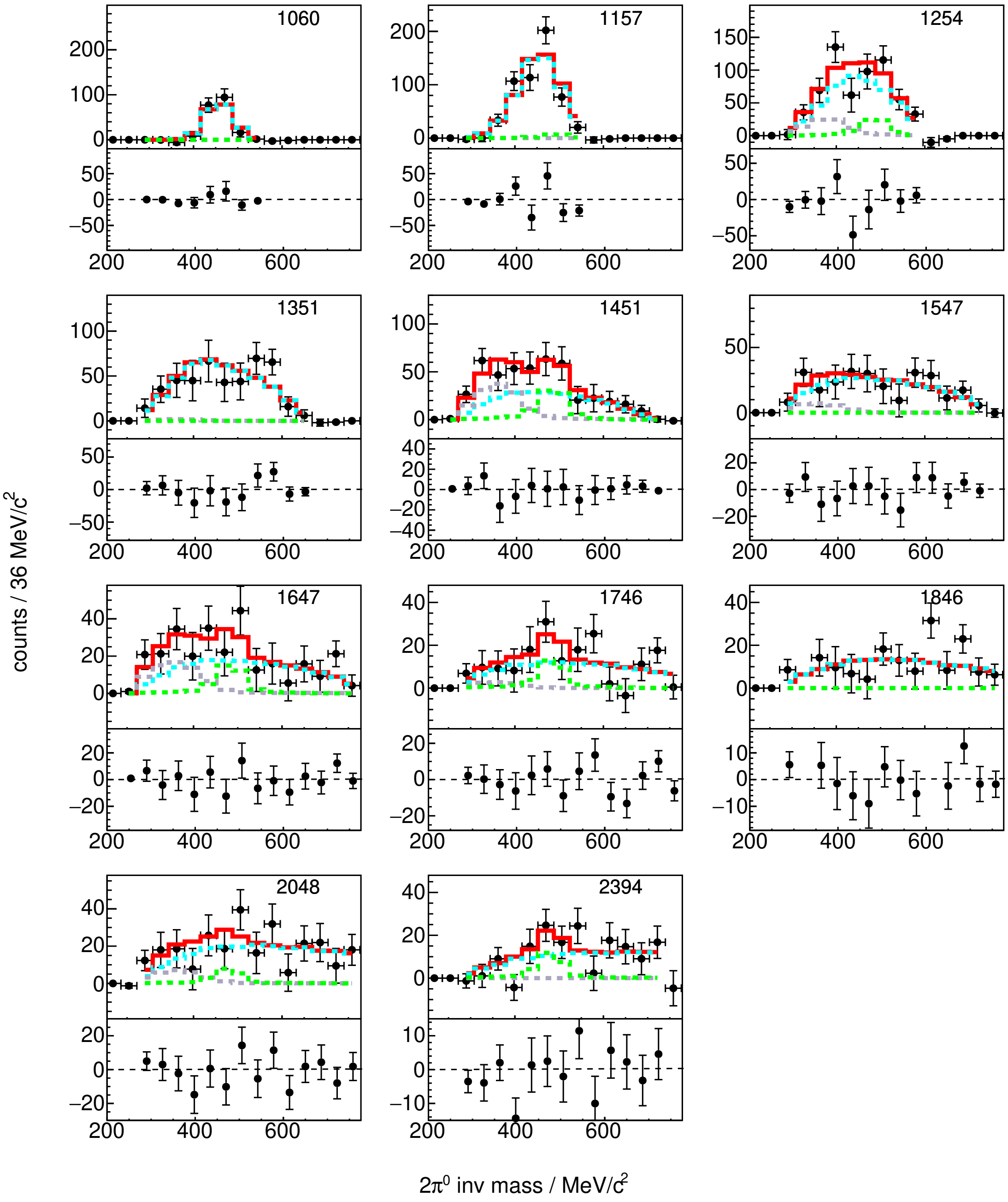

Figure A.1: Fits for all energies in the angular range $-0.7 < \cos\theta^{K}_{\mathrm{CM}} < -0.4$. The data is fitted with the expected signal spectrum $\gamma n \longrightarrow K^0\Sigma^0$(green), $\gamma n \longrightarrow \eta n$ (grey) and $\gamma n \longrightarrow \pi^0\pi^0\pi^0 n$ (light blue). The full fit is shown in red. Underneath each fit the residuals are shown.

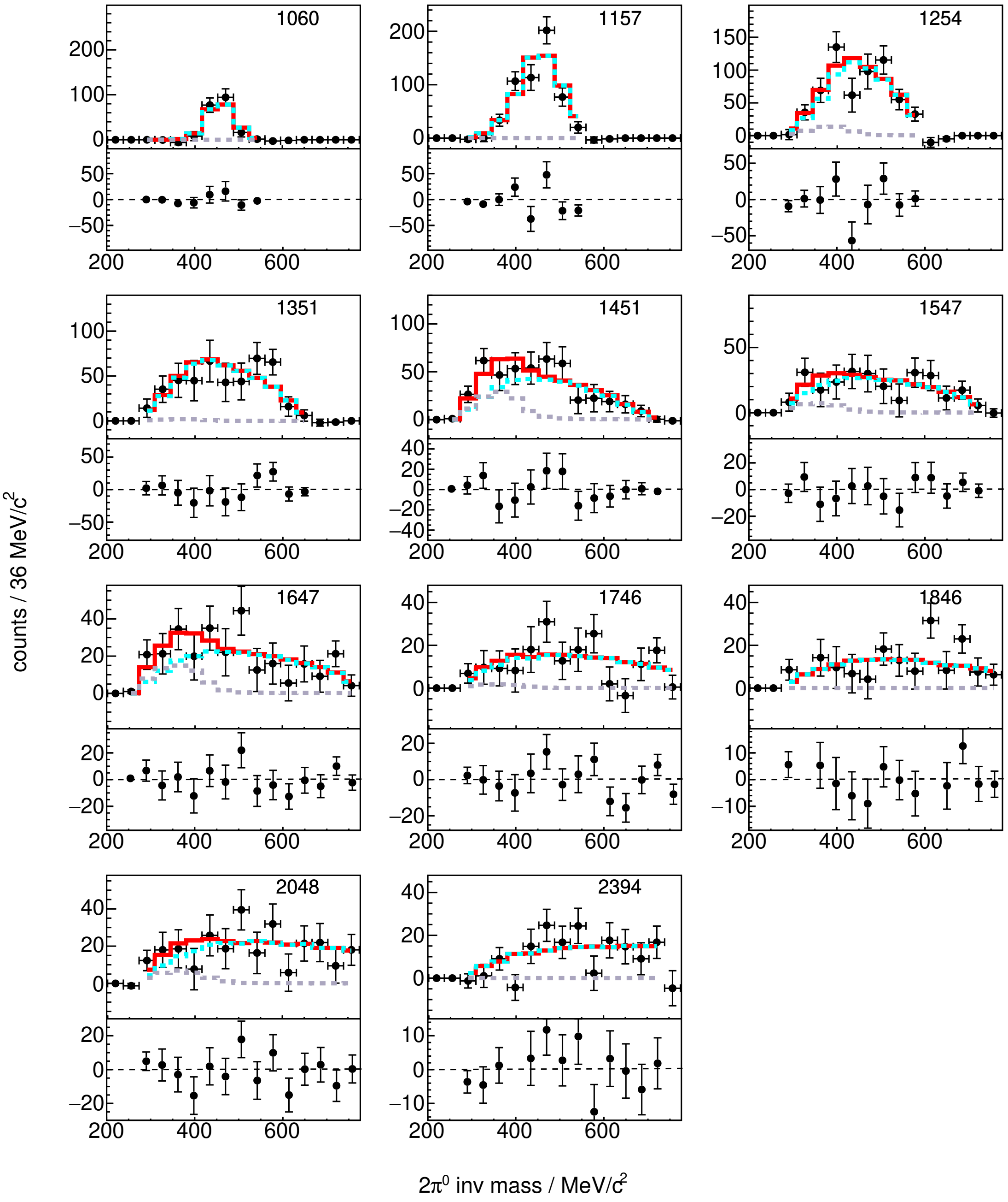

Figure A.2: Fits for all energies in the angular range $-0.7 < \cos\theta^K_{\mathrm{CM}} < -0.4$. The data is fitted with the background channels only, namely $\gamma n \to \eta n$ (grey) and $\gamma n \to \pi^0\pi^0\pi^0 n$ (light blue). The full fit is shown in red. Underneath each fit the residuals are shown.

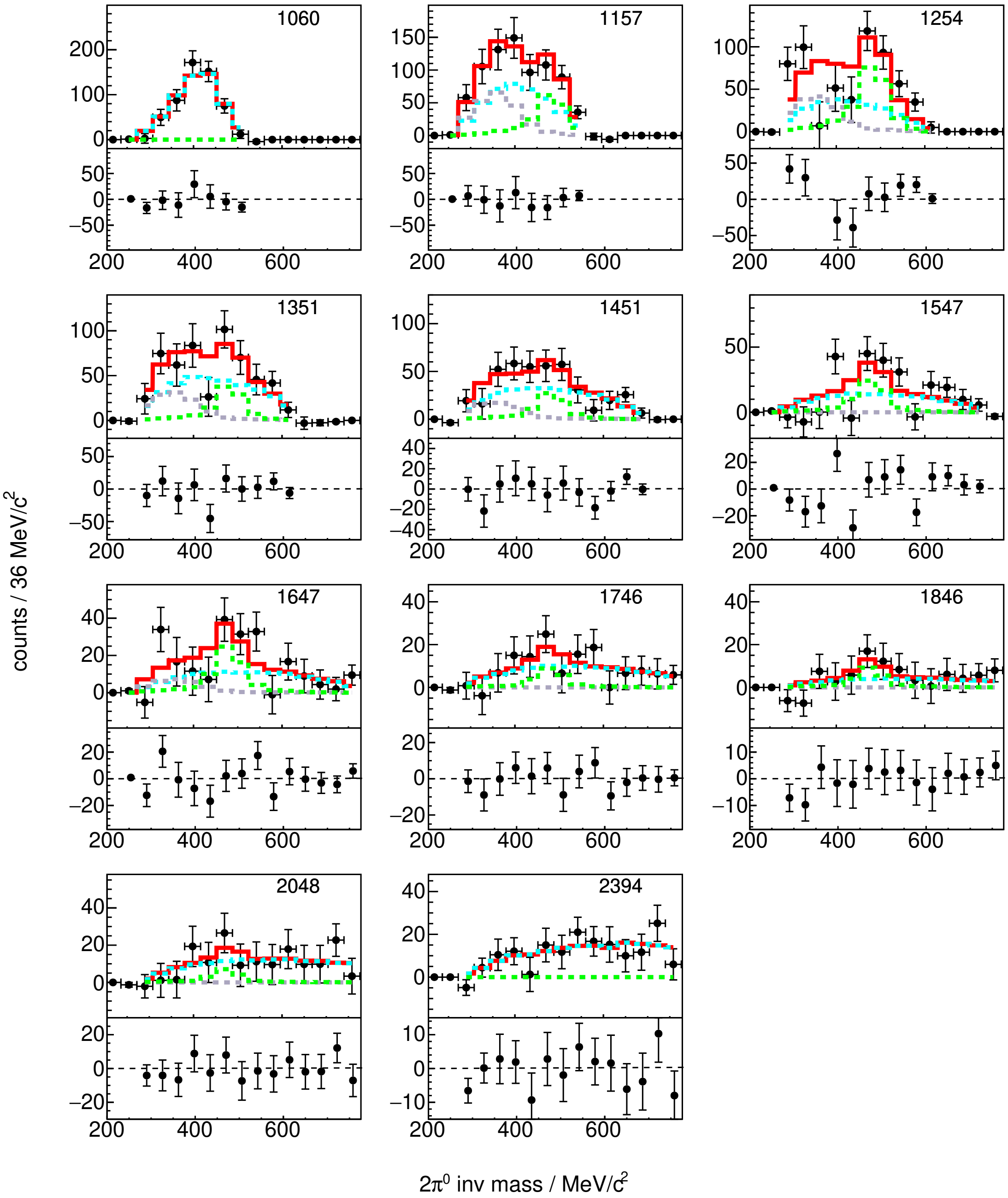

Figure A.3: Fits for all energies in the angular range $-0.4 < \cos\theta^{K}_{\mathrm{CM}} < -0.1$. The data is fitted with the expected signal spectrum $\gamma n \to K^0\Sigma^0$(green), $\gamma n \to \eta n$ (grey) and $\gamma n \to \pi^0\pi^0\pi^0 n$ (light blue). The full fit is shown in red. Underneath each fit the residuals are shown.

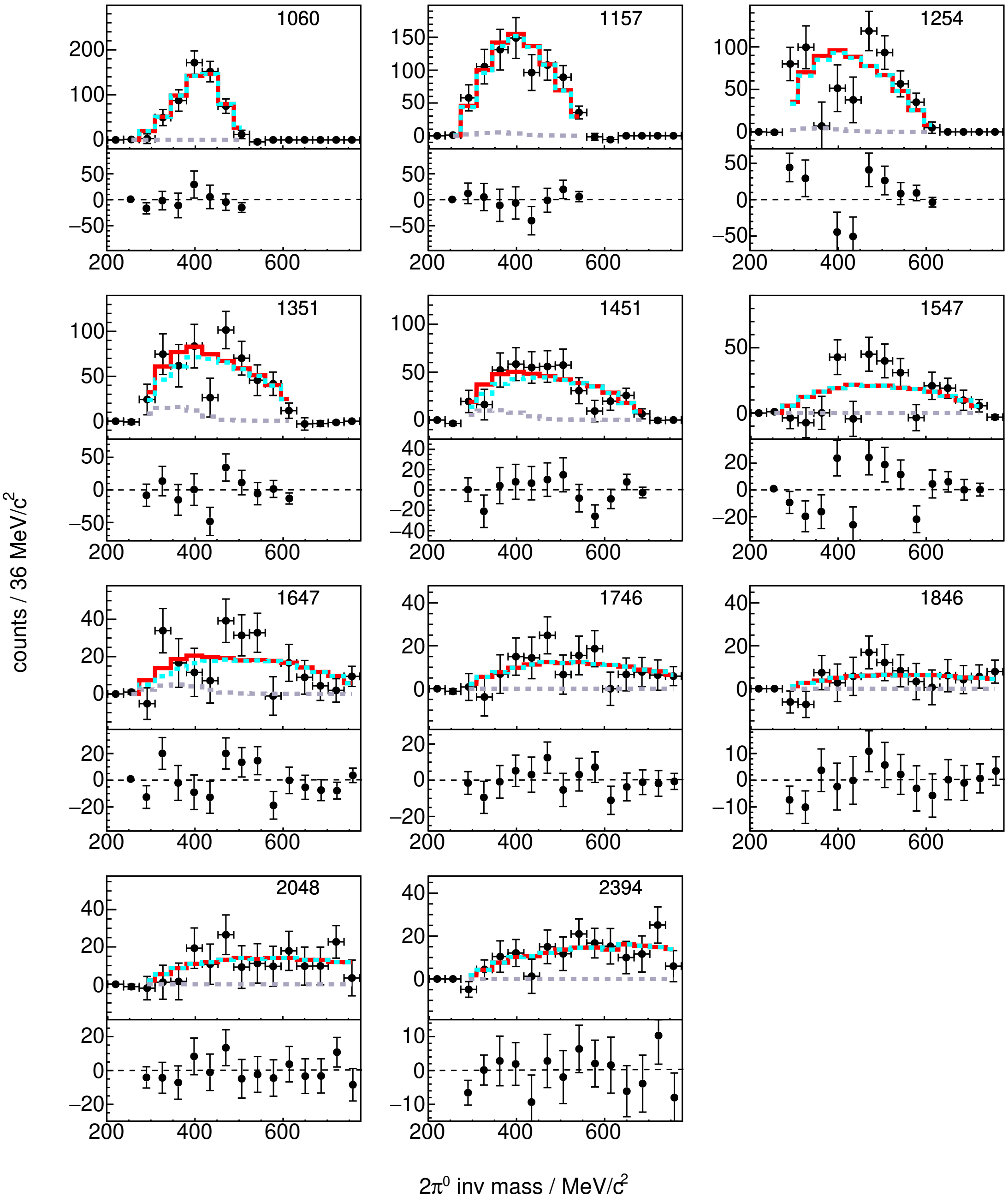

Figure A.4: Fits for all energies in the angular range $-0.4 < \cos\theta^K_{\mathrm{CM}} < -0.1$. The data is fitted with the background channels only, namely $\gamma n \rightarrow \eta n$ (grey) and $\gamma n \rightarrow \pi^0\pi^0\pi^0 n$ (light blue). The full fit is shown in red. Underneath each fit the residuals are shown.

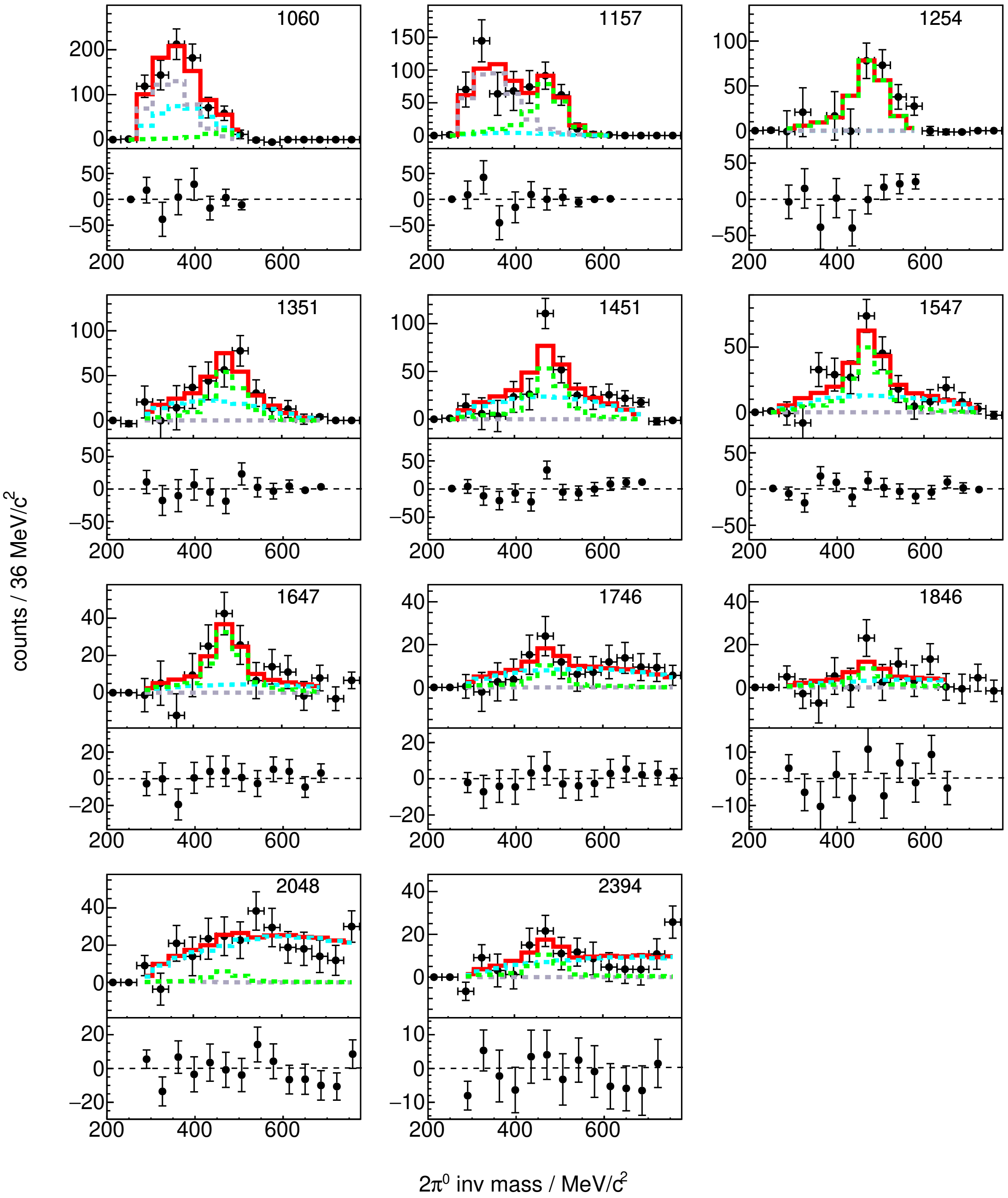

Figure A.5: Fits for all energies in the angular range $-0.1 \cos\theta^K_{\mathrm{CM}} < 0.2$. The data is fitted with the expected signal spectrum $\gamma n \rightarrow K^0\Sigma^0$(green), $\gamma n \rightarrow \eta n$ (grey) and $\gamma n \rightarrow \pi^0\pi^0\pi^0 n$ (light blue). The full fit is shown in red. Underneath each fit the residuals are shown.

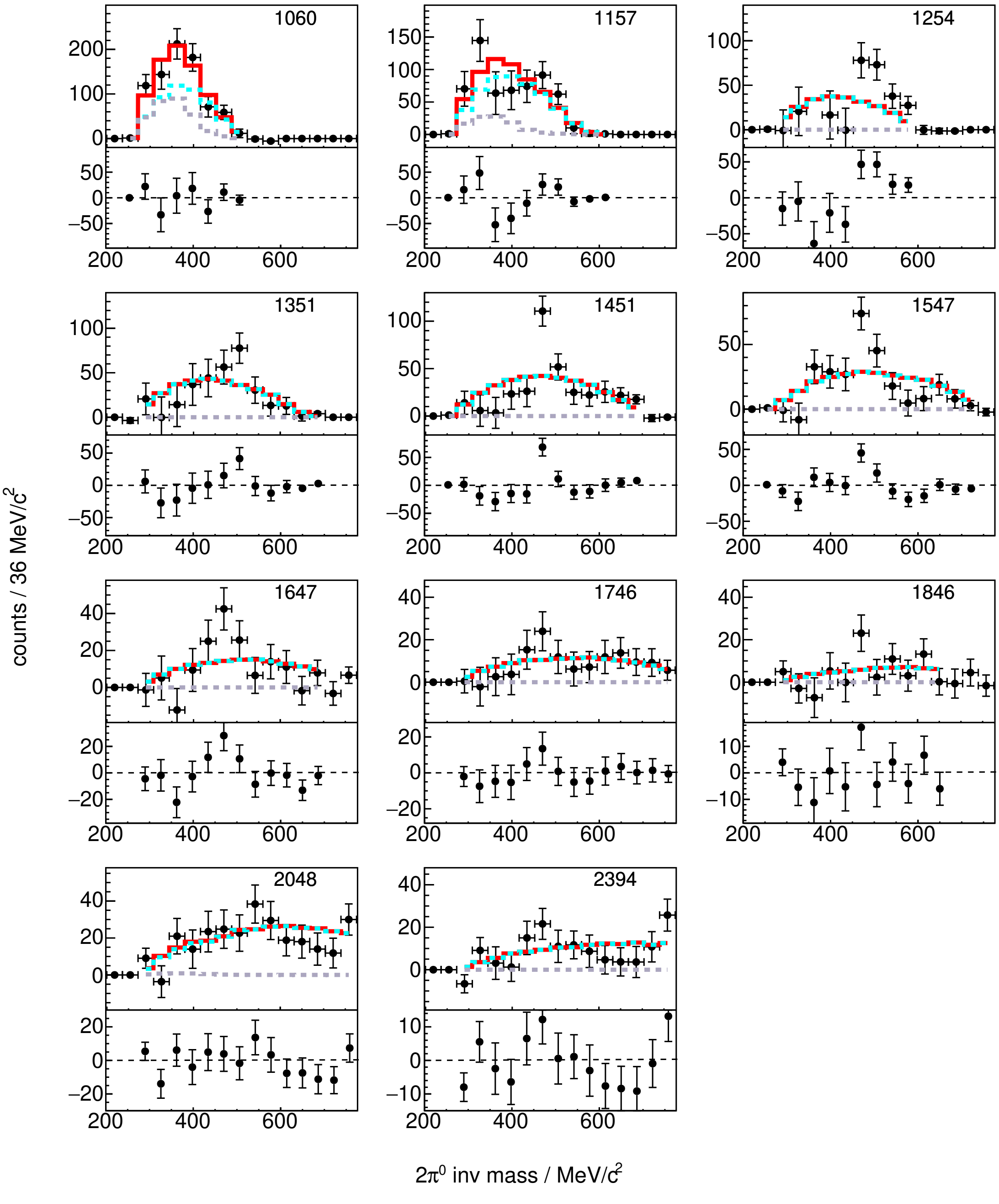

Figure A.6: Fits for all energies in the angular range $-0.1 < \cos\theta^{K}_{\mathrm{CM}} < 0.2$. The data is fitted with the background channels only, namely $\gamma n \rightarrow \eta n$ (grey) and $\gamma n \rightarrow \pi^0\pi^0\pi^0 n$ (light blue). The full fit is shown in red. Underneath each fit the residuals are shown.

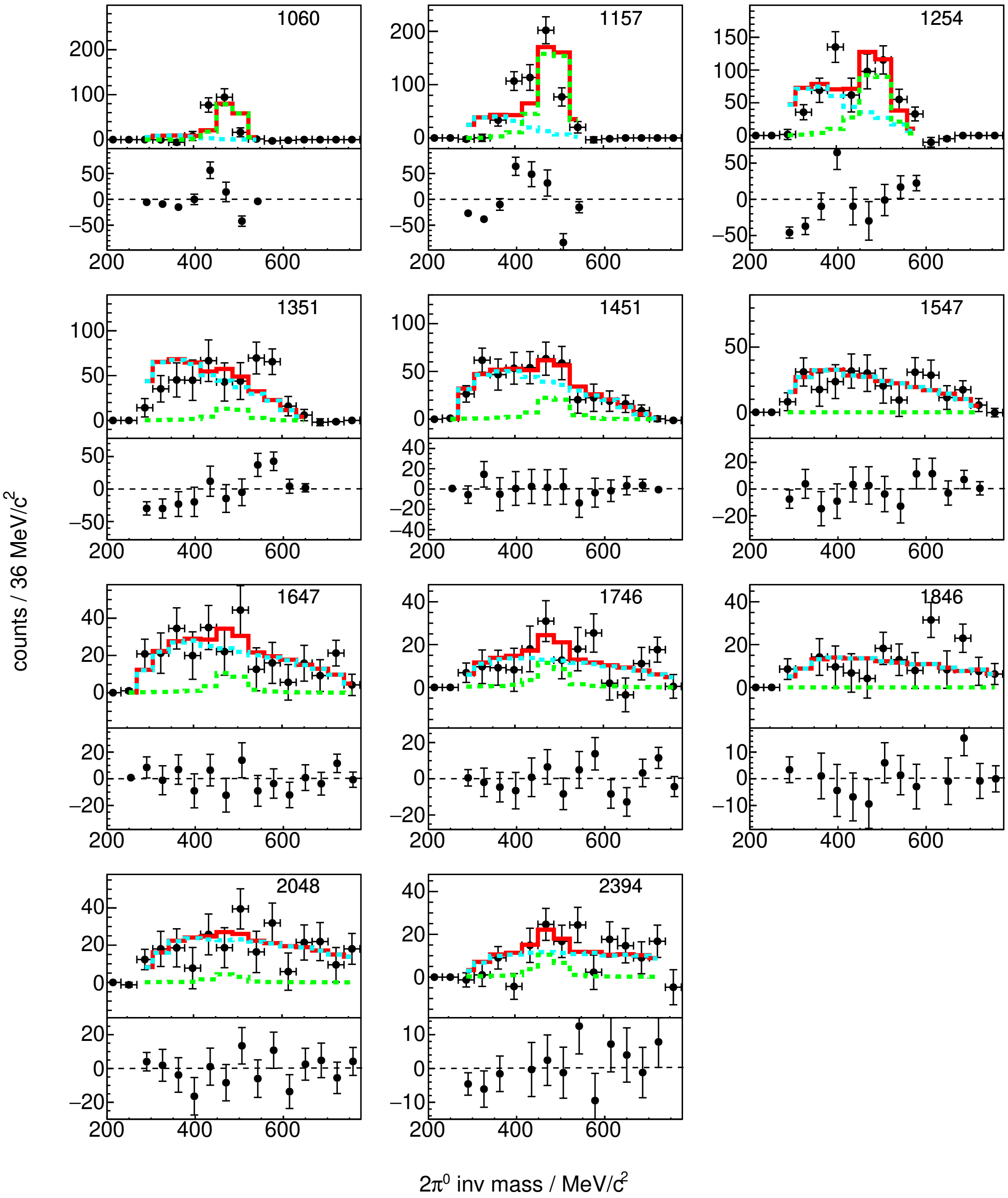

Figure A.7: Fits for all energies in the angular range $-0.7 < \cos\theta^{K}_{\mathrm{CM}} < -0.4$. The data is fitted with the expected signal spectrum from simulated $\gamma n \rightarrow K^0\Sigma^0$ (green) and a background spectrum determined from real data with relaxed cuts (light blue). The full fit is shown in red. Underneath each fit the residuals are shown.

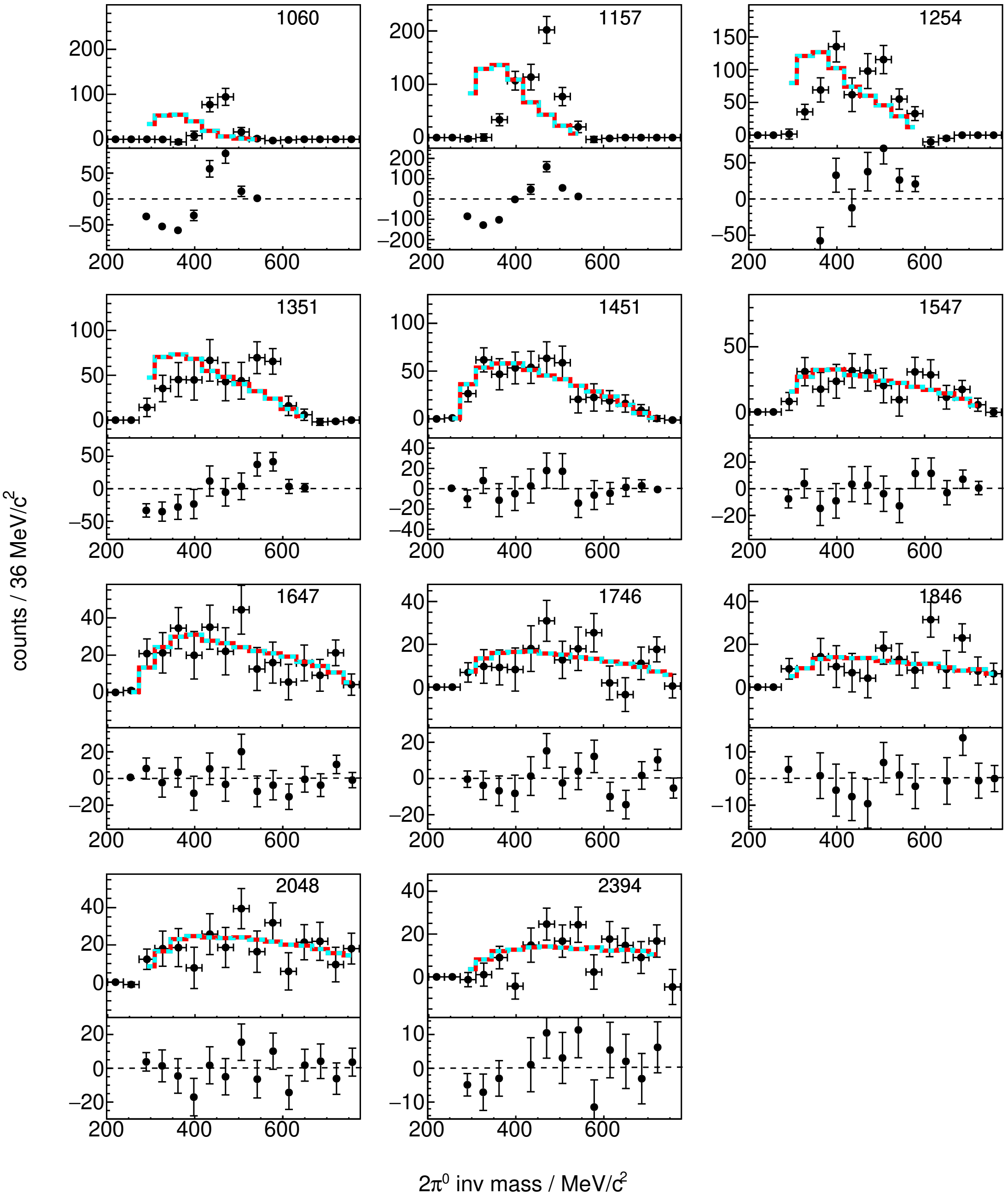

Figure A.8: Fits for all energies in the angular range $-0.7 < \cos\theta^K_{\mathrm{CM}} < -0.4$.The data is fitted with a background spectrum determined from real data with relaxed cuts (light blue). The full fit is shown in red. Underneath each fit the residuals are shown.

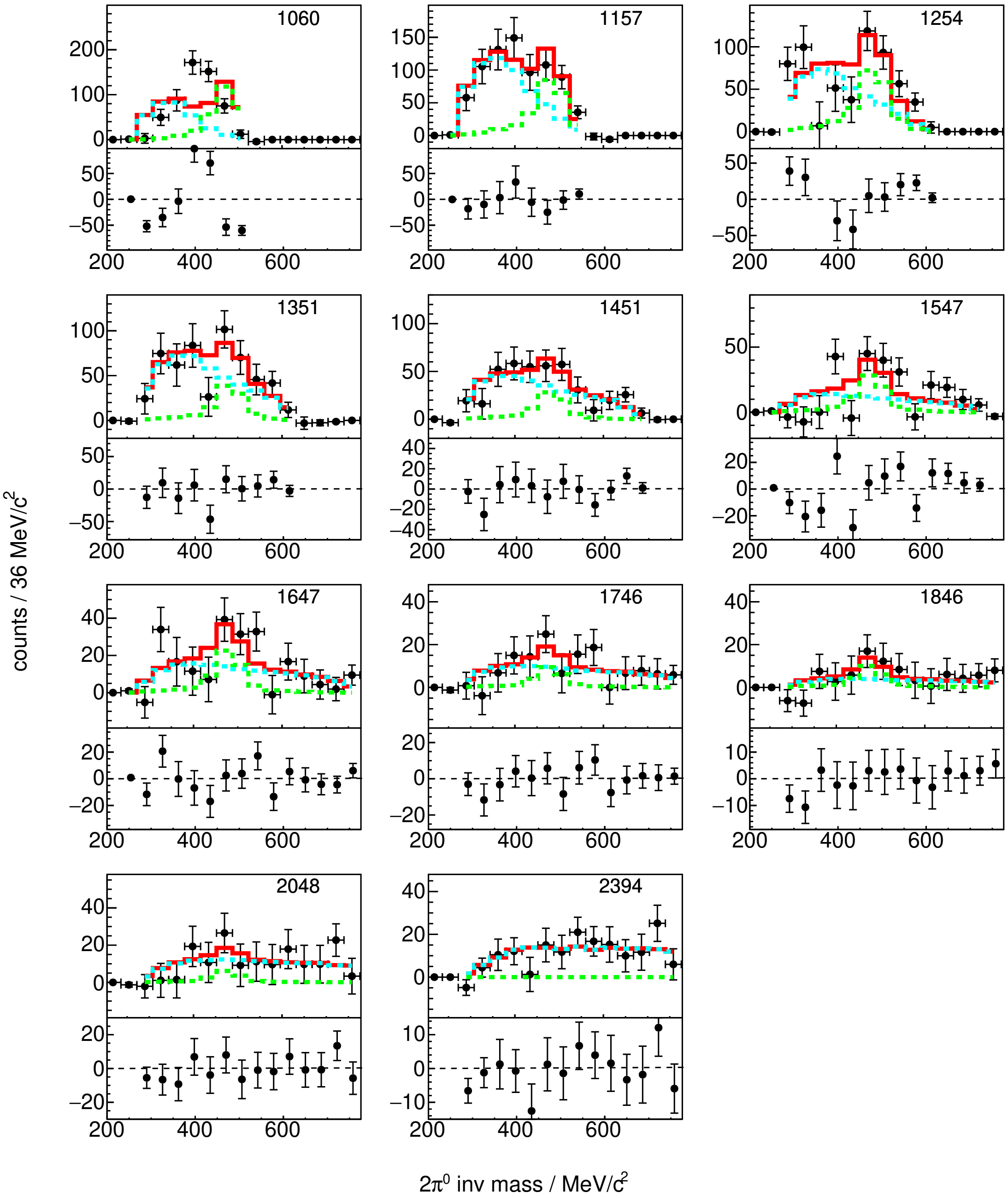

Figure A.9: Fits for all energies in the angular range $-0.4 < \cos\theta^K_{\mathrm{CM}} < -0.1$. The data is fitted with the expected signal spectrum from simulated $\gamma n \to K^0\Sigma^0$ (green) and a background spectrum determined from real data with relaxed cuts (light blue). The full fit is shown in red. Underneath each fit the residuals are shown.

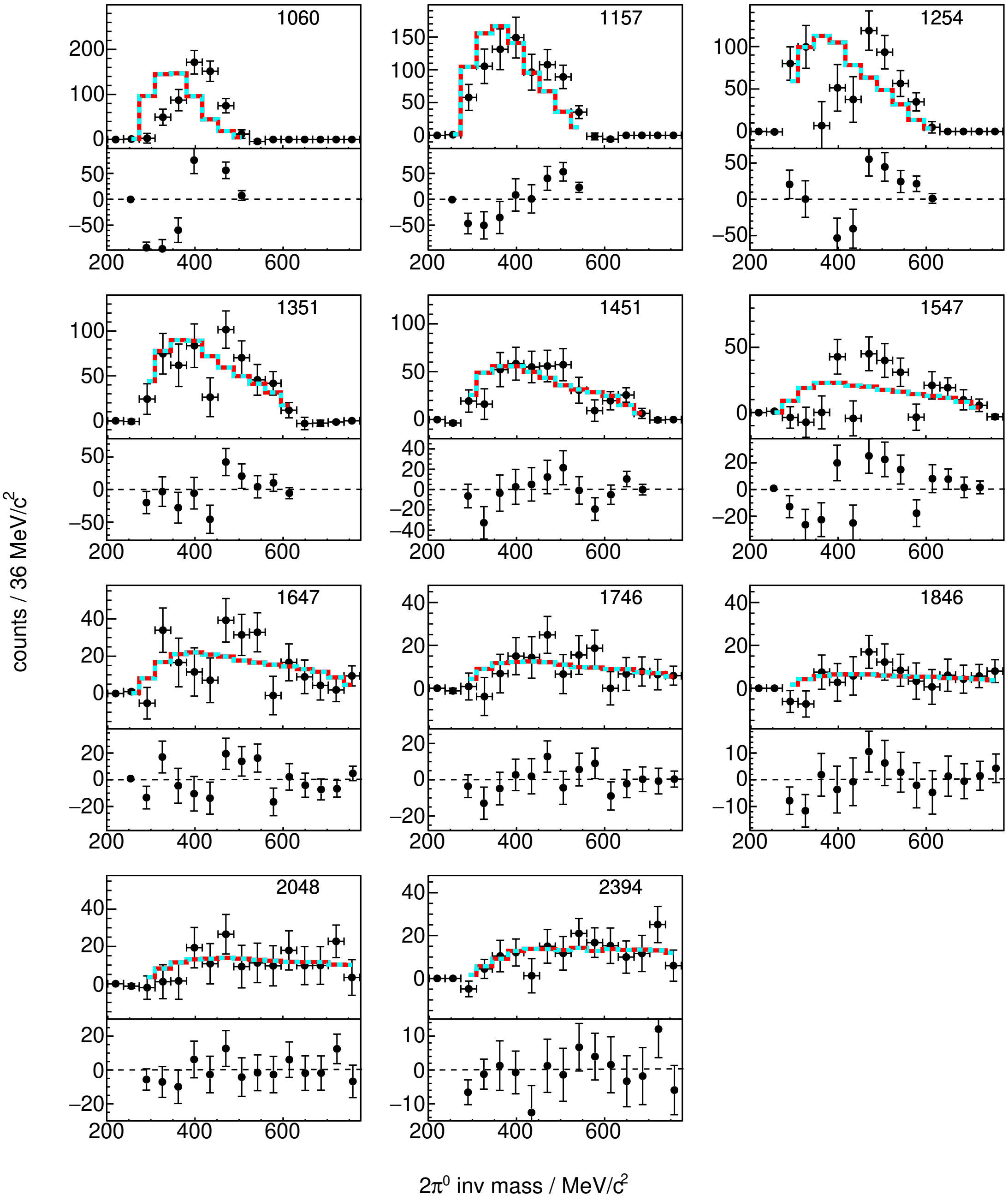

Figure A.10: Fits for all energies in the angular range $-0.4 < \cos\theta^K_{\mathrm{CM}} < -0.1$.The data is fitted with a background spectrum determined from real data with relaxed cuts (light blue). The full fit is shown in red. Underneath each fit the residuals are shown.

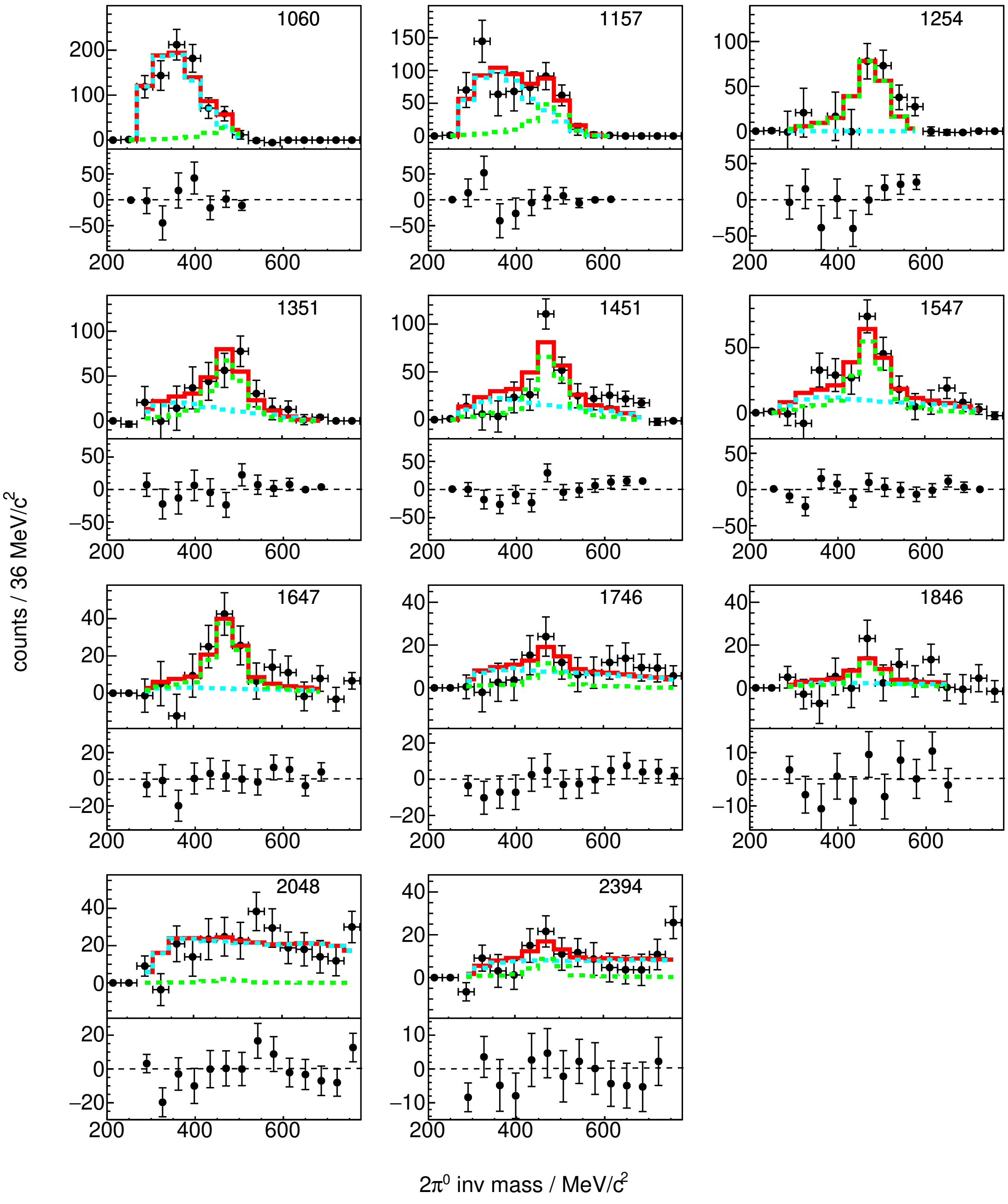

Figure A.11: Fits for all energies in the angular range $-0.1\cos\theta^{K}_{\mathrm{CM}} < 0.2$. The data is fitted with the expected signal spectrum from simulated $\gamma n \to K^0\Sigma^0$ (green) and a background spectrum determined from real data with relaxed cuts (light blue). The full fit is shown in red. Underneath each fit the residuals are shown.

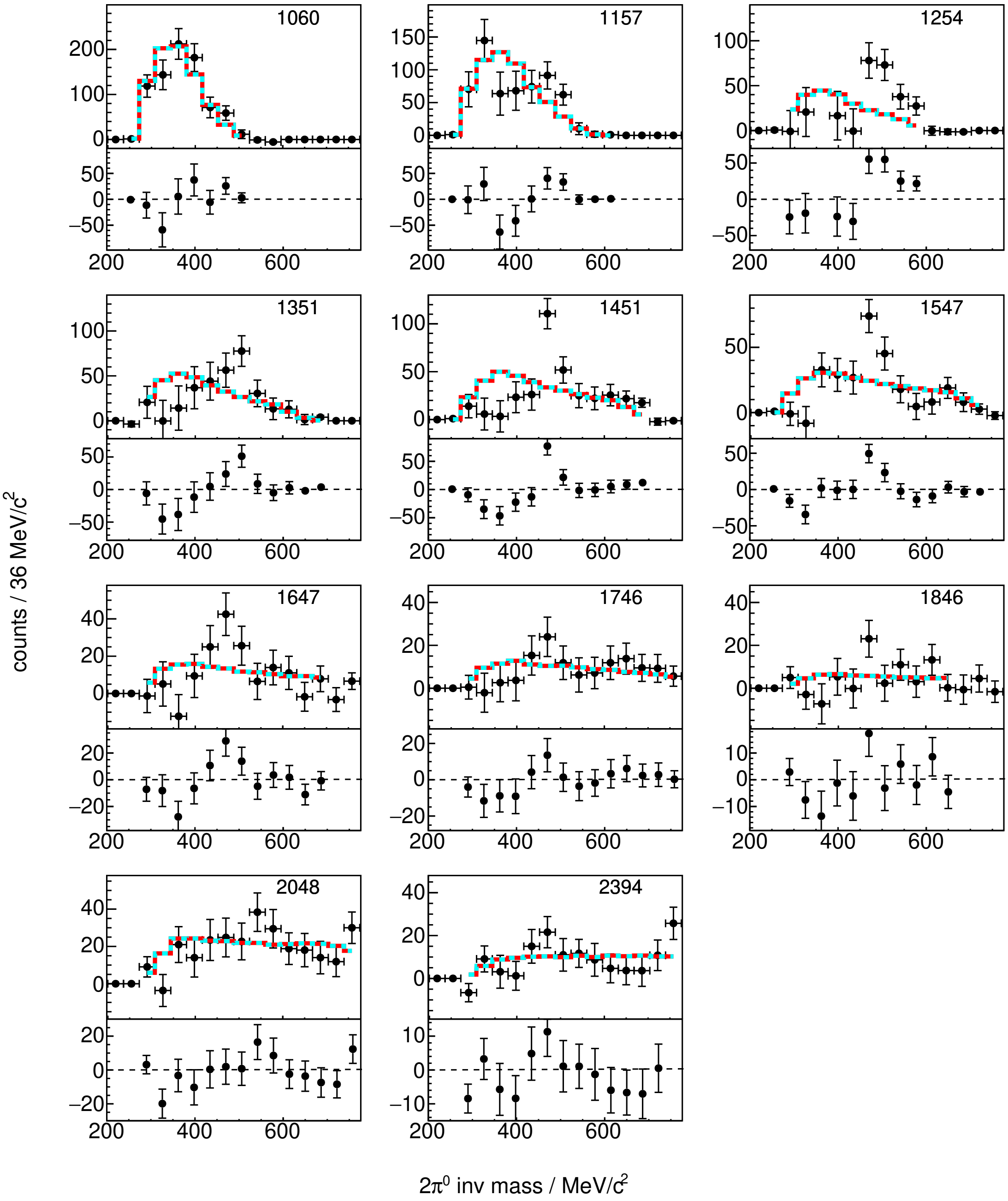

Figure A.12: Fits for all energies in the angular range $-0.1 < \cos\theta^K_{\mathrm{CM}} < 0.2$. The data is fitted with a background spectrum determined from real data with relaxed cuts (light blue). The full fit is shown in red. Underneath each fit the residuals are shown.

APPENDIX B

Values of Fit Quality Tests

The following pages give all values for the different fit quality tests performed in chapter 6.2.

	$-0.7 < \cos\theta^{K}_{\text{CM}} -0.4$			$-0.4 < \cos\theta^{K}_{\text{CM}} -0.1$			$-0.1 < \cos\theta^{K}_{\text{CM}} 0.2$			$0.2 < \cos\theta^{K}_{\text{CM}} 0.5$		
E_{γ}/MeV	BG+S	BG	$\frac{\text{BG}}{\text{BG+S}}$	BG+S	BG	$\frac{\text{BG}}{\text{BG+S}}$	BG+S	BG	$\frac{\text{BG}}{\text{BG+S}}$	BG+S	BG	$\frac{\text{BG}}{\text{BG+S}}$
1050	0.00	0.00	-	1.23	1.23	1.00	0.99	0.70	0.71	1.92	1.64	0.86
1150	2.70	2.67	0.99	0.35	0.66	1.89	0.70	1.34	1.92	1.25	1.57	1.25
1250	1.44	1.41	0.98	3.15	3.44	1.09	1.71	3.62	2.12	1.58	2.13	1.35
1350	0.89	0.90	1.01	1.08	1.45	1.34	0.73	1.26	1.72	0.48	3.77	7.86
1450	0.39	0.67	1.70	0.90	1.12	1.25	1.79	2.88	1.60	1.17	2.04	1.75
1550	0.58	0.53	0.91	1.85	2.18	1.18	0.87	2.41	2.78	1.54	2.02	1.32
1650	0.79	0.84	1.06	1.25	1.58	1.27	0.56	1.60	2.84	2.09	2.25	1.07
1750	1.21	1.30	1.08	0.49	0.61	1.25	0.27	0.41	1.51	0.86	1.41	1.65
1850	1.87	1.87	1.00	0.57	0.73	1.28	0.90	1.08	1.21	0.97	1.06	1.09
2050	0.88	0.87	0.99	0.48	0.54	1.13	0.98	1.04	1.07	1.27	1.23	0.97
2400	1.14	1.47	1.29	0.80	0.80	1.00	1.08	1.38	1.28	1.37	1.30	0.95

Table B.1: χ^2/ndf values for PS method.

	$-0.7 < \cos\theta^{K}_{\text{CM}} -0.4$			$-0.4 < \cos\theta^{K}_{\text{CM}} -0.1$			$-0.1 < \cos\theta^{K}_{\text{CM}} 0.2$			$0.2 < \cos\theta^{K}_{\text{CM}} 0.5$		
E_{γ}/MeV	BG+S	BG	$\frac{\text{BG}}{\text{BG+S}}$	BG+S	BG	$\frac{\text{BG}}{\text{BG+S}}$	BG+S	BG	$\frac{\text{BG}}{\text{BG+S}}$	BG+S	BG	$\frac{\text{BG}}{\text{BG+S}}$
1050	0.00	0.00	-	18.7	22.0	1.18	1.04	1.10	1.06	1.47	1.40	0.95
1150	21.2	138.6	6.55	0.65	3.56	5.46	0.78	1.57	2.02	1.57	2.95	1.88
1250	9.12	23.6	2.59	2.79	4.29	1.54	1.71	4.45	2.61	1.75	3.01	1.72
1350	3.26	3.30	1.01	0.97	1.53	1.57	0.95	1.94	2.05	0.48	4.10	8.55
1450	0.31	0.48	1.54	0.83	1.09	1.32	2.32	4.19	1.80	1.02	1.92	1.89
1550	0.69	0.63	0.92	2.07	2.38	1.15	0.93	2.59	2.80	2.34	2.37	1.01
1650	0.81	0.80	0.98	1.14	1.41	1.23	0.60	1.71	2.83	1.98	2.09	1.06
1750	1.11	1.17	1.06	0.56	0.64	1.13	0.49	0.61	1.24	0.85	1.19	1.41
1850	2.11	1.95	0.92	0.65	0.77	1.19	0.95	1.10	1.16	0.96	0.96	0.99
2050	0.77	0.73	0.95	0.57	0.57	1.00	1.18	1.10	0.93	1.34	1.26	0.94
2400	1.48	1.64	1.11	0.85	0.78	0.92	1.14	1.24	1.09	1.30	1.21	0.93

Table B.2: χ^2/ndf values for RD method.

	$-0.7 < \cos\theta^{K}_{\mathrm{CM}}-0.4$			$-0.4 < \cos\theta^{K}_{\mathrm{CM}}-0.1$			$-0.1 < \cos\theta^{K}_{\mathrm{CM}}0.2$			$0.2 < \cos\theta^{K}_{\mathrm{CM}}0.5$		
E_{γ}/MeV	BG+S	BG	$\frac{\mathrm{S+BG}}{\mathrm{BG}}$	BG+S	BG	$\frac{\mathrm{S+BG}}{\mathrm{BG}}$	BG+S	BG	$\frac{\mathrm{S+BG}}{\mathrm{BG}}$	BG+S	BG	$\frac{\mathrm{S+BG}}{\mathrm{BG}}$
1050	0.92	0.92	1.00	0.98	0.98	1.00	1.00	1.00	1.00	0.48	0.46	1.04
1150	0.31	0.41	0.76	1.00	1.00	1.00	0.67	0.39	1.74	0.98	0.33	2.95
1250	0.90	0.91	0.99	0.16	0.06	2.79	0.39	0.00	390.89	0.61	0.06	10.46
1350	0.74	0.74	1.00	0.98	0.86	1.14	0.95	0.55	1.72	0.98	0.09	10.85
1450	1.00	0.75	1.34	0.98	0.76	1.29	0.15	0.02	8.33	0.98	0.24	4.14
1550	0.97	0.97	1.00	0.33	0.15	2.18	0.84	0.06	14.47	0.92	0.83	1.11
1650	1.00	0.92	1.09	1.00	0.39	2.56	0.83	0.46	1.81	0.59	0.07	7.93
1750	0.94	0.50	1.90	1.00	0.93	1.07	0.89	0.81	1.10	1.00	0.36	2.82
1850	0.28	0.28	1.00	0.86	0.83	1.03	0.88	0.86	1.02	0.94	0.77	1.21
2050	1.00	0.99	1.01	1.00	0.99	1.00	0.88	0.67	1.30	0.97	0.82	1.20
2400	0.79	0.63	1.26	1.00	1.00	1.00	0.84	0.94	0.90	0.97	0.97	1.00

Table B.3: KS values for PS method.

	$-0.7 < \cos\theta^{K}_{\mathrm{CM}}-0.4$			$-0.4 < \cos\theta^{K}_{\mathrm{CM}}-0.1$			$-0.1 < \cos\theta^{K}_{\mathrm{CM}}0.2$			$0.2 < \cos\theta^{K}_{\mathrm{CM}}0.5$		
E_{γ}/MeV	BG+S	BG	$\frac{\mathrm{S+BG}}{\mathrm{BG}}$	BG+S	BG	$\frac{\mathrm{S+BG}}{\mathrm{BG}}$	BG+S	BG	$\frac{\mathrm{S+BG}}{\mathrm{BG}}$	BG+S	BG	$\frac{\mathrm{S+BG}}{\mathrm{BG}}$
1050	0.02	$\approx 10^{-26}$	$\approx 10^{24}$	$\approx 10^{-4}$	$\approx 10^{-20}$	$\approx 10^{16}$	0.78	0.31	2.49	0.64	0.76	0.85
1150	0.01	$\approx 10^{-33}$	$\approx 10^{31}$	1.00	0.003	359	0.36	0.22	1.67	0.90	0.003	269
1250	0.05	$\approx 10^{-10}$	$\approx 10^{7}$	0.20	$\approx 10^{-5}$	3527	0.37	$\approx 10^{-5}$	10637	0.58	$\approx 10^{-4}$	735
1350	0.02	0.003	6.20	0.85	0.08	10.56	0.59	0.01	48.71	1.00	0.001	797
1450	1.00	0.98	1.02	0.88	0.49	1.79	0.02	0.00	6845	1.00	0.49	2.04
1550	0.64	0.64	1.00	0.10	0.01	10.14	0.54	0.09	6.27	0.01	0.01	1.25
1650	1.00	0.86	1.15	1.00	0.71	1.41	0.75	0.06	13.60	0.32	0.05	6.99
1750	1.00	0.92	1.09	0.87	0.70	1.24	0.37	0.18	2.12	1.00	0.79	1.27
1850	0.04	0.04	1.00	0.74	0.60	1.23	0.70	0.39	1.80	0.54	0.37	1.43
2050	0.98	1.00	0.99	0.90	0.86	1.05	0.60	0.56	1.06	0.18	0.18	1.01
2400	0.34	0.19	1.79	0.76	0.76	1.00	0.69	0.72	0.95	0.77	0.78	0.99

Table B.4: KS values for RD method.

	$-0.7 < \cos\theta^{K}_{\mathrm{CM}} -0.4$				$-0.4 < \cos\theta^{K}_{\mathrm{CM}} -0.1$			
E_γ/MeV	ζ(BG+S)	ζ(BG)	ζ(BG)-ζ(BG+S)	p	ζ(BG+S)	ζ(BG)	ζ(BG)-ζ(BG+S)	p
1050	0.00	0.00	0.00	1	7.37	7.37	0.00	1
1150	16.21	15.99	-0.22	1	2.10	4.62	2.52	0.02
1250	8.64	9.85	1.21	0.07	22.04	27.54	5.50	$9.3 \cdot 10^{-4}$
1350	8.10	8.10	0.00	1	7.55	11.59	4.04	0.01
1450	4.30	7.98	3.68	0.01	8.10	11.22	3.12	0.02
1550	5.82	5.82	0.00	1	22.24	26.18	3.94	0.01
1650	9.51	10.92	1.41	0.10	14.98	20.56	5.58	$1.9 \cdot 10^{-3}$
1750	13.30	15.63	2.33	0.05	5.88	7.33	1.45	0.11
1850	22.38	22.38	0.00	1	6.84	8.73	1.89	0.07
2050	9.65	10.41	0.76	0.16	5.70	6.43	0.73	0.25
2400	12.49	16.14	3.65	0.03	9.55	9.55	0.00	1

	$-0.1 < \cos\theta^{K}_{\mathrm{CM}} 0.2$				$0.2 < \cos\theta^{K}_{\mathrm{CM}} 0.5$			
E_γ/MeV	ζ(BG+S)	ζ(BG)	ζ(BG)-ζ(BG+S)	p	ζ(BG+S)	ζ(BG)	ζ(BG)-ζ(BG+S)	p
1050	4.97	4.21	-0.76	1	11.49	11.47	-0.02	1
1150	5.57	12.03	6.46	$7.9 \cdot 10^{-4}$	8.75	10.98	2.23	0.04
1250	13.64	25.32	11.68	$7.3 \cdot 10^{-14}$	14.20	19.19	4.99	$7.8 \cdot 10^{-4}$
1350	7.33	12.62	5.29	$3.9 \cdot 10^{-4}$	4.32	30.19	25.87	$2.5 \cdot 10^{-21}$
1450	19.71	31.63	11.92	$6.2 \cdot 10^{-6}$	9.35	18.37	9.02	$1.4 \cdot 10^{-4}$
1550	10.38	28.86	18.48	$2.8 \cdot 10^{-8}$	15.36	20.20	4.84	$4.1 \cdot 10^{-3}$
1650	5.64	15.99	10.35	$2.4 \cdot 10^{-5}$	25.13	29.19	4.06	0.01
1750	3.29	4.96	1.67	0.08	11.12	18.33	7.21	$7.8 \cdot 10^{-4}$
1850	8.07	9.76	1.69	0.08	8.72	10.55	1.83	0.07
2050	11.72	12.51	0.79	0.24	15.24	16.05	0.81	0.20
2400	12.95	16.57	3.62	0.04	15.10	15.59	0.49	0.28

Table B.5: Values of ζ, $\Delta\zeta$ and p determined for the hypothesis test with PS background description.

	$-0.7 < \cos\theta^{K}_{\mathrm{CM}} -0.4$				$-0.4 < \cos\theta^{K}_{\mathrm{CM}} -0.1$			
E_γ/MeV	ζ(BG+S)	ζ(BG)	ζ(BG)-ζ(BG+S)	p	ζ(BG+S)	ζ(BG)	ζ(BG)-ζ(BG+S)	p
1050	0.00	0.00	0.00	1	111.87	154.14	42.27	$1.7 \cdot 10^{-18}$
1150	127.02	970.50	843.48	$5.5 \cdot 10^{-222}$	4.56	28.46	23.90	$4.0 \cdot 10^{-3}$
1250	63.87	188.94	125.07	$3.0 \cdot 10^{-18}$	22.30	38.64	16.34	0.12
1350	29.36	32.97	3.61	0.24	7.79	13.76	5.97	0.03
1450	3.77	6.28	2.51	0.14	8.28	12.01	3.73	0.05
1550	7.59	7.59	0.00	1	24.88	31.00	6.12	$4.3 \cdot 10^{-3}$
1650	10.52	11.15	0.63	0.37	14.88	19.72	4.84	0.01
1750	13.28	15.27	1.99	0.13	6.77	8.30	1.53	0.18
1850	25.31	25.31	0.00	1	7.77	9.98	2.21	0.07
2050	9.18	9.47	0.29	0.63	6.84	7.41	0.57	0.38
2400	16.24	19.71	3.47	0.03	10.15	10.15	0.00	1

	$-0.1 < \cos\theta^{K}_{\mathrm{CM}} 0.2$				$0.2 < \cos\theta^{K}_{\mathrm{CM}} 0.5$			
E_γ/MeV	ζ(BG+S)	ζ(BG)	ζ(BG)-ζ(BG+S)	p	ζ(BG+S)	ζ(BG)	ζ(BG)-ζ(BG+S)	p
1050	6.24	7.71	1.47	0.27	10.29	11.19	0.90	0.35
1150	7.02	15.73	8.71	0.25	11.01	23.63	12.62	0.02
1250	13.64	35.61	21.97	0.02	15.76	30.05	14.29	0.01
1350	9.47	21.38	11.91	$3.7 \cdot 10^{-3}$	4.32	36.93	32.61	$3.0 \cdot 10^{-12}$
1450	25.55	50.26	24.71	$8.5 \cdot 10^{-9}$	9.14	19.19	10.05	$7.6 \cdot 10^{-05}$
1550	11.10	33.62	22.52	$4.2 \cdot 10^{-9}$	23.42	26.07	2.65	0.06
1650	6.04	18.77	12.73	$1.2 \cdot 10^{-5}$	25.68	29.19	3.51	0.06
1750	5.93	7.98	2.05	0.11	11.01	16.71	5.70	0.01
1850	8.54	11.04	2.50	0.07	9.63	10.53	0.90	0.36
2050	14.12	14.30	0.18	0.66	17.41	17.64	0.23	0.74
2400	13.66	16.14	2.48	0.07	15.56	15.68	0.12	0.82

Table B.6: Values of ζ, $\Delta\zeta$ and p determined for the hypothesis test with RD background description.

APPENDIX C

Side band fits

The following pages show the fits to the side bands, that were not shown in chapter 6.3.

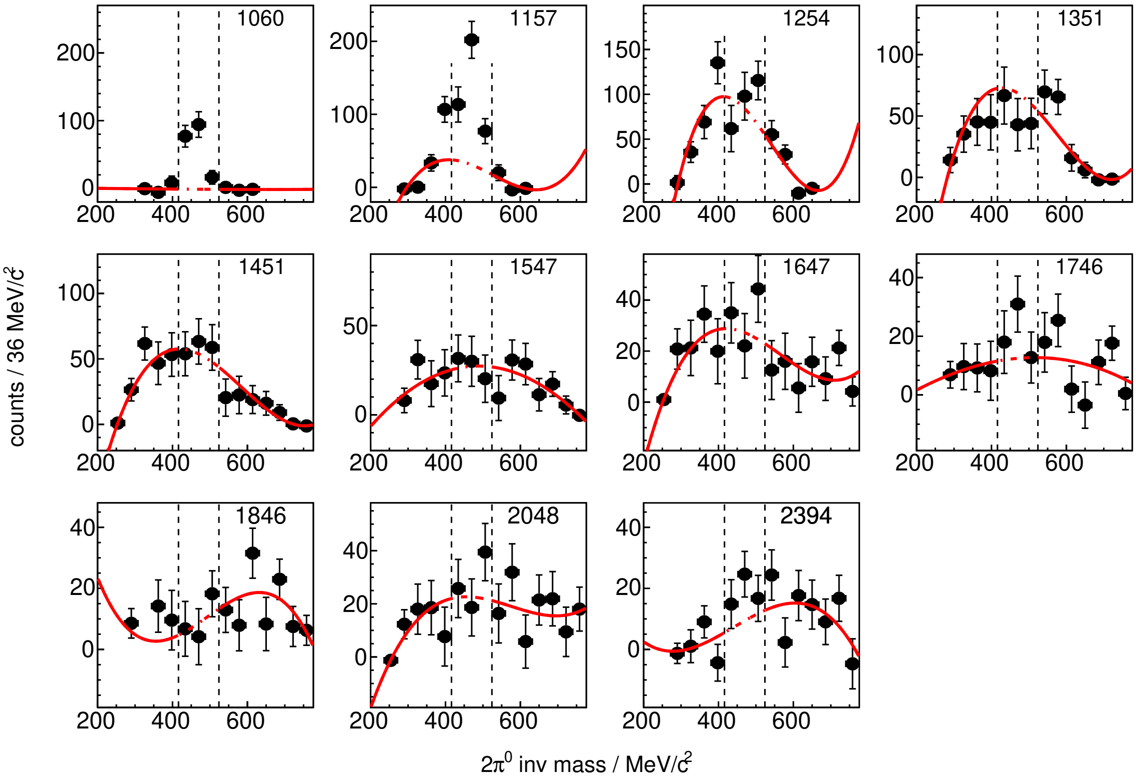

Figure C.1: $2\pi^0$ invariant mass spectrum in the angular range $-0.7 < \cos\theta^K_{\mathrm{CM}} < -0.4$. The region within the black dashed lines is identified as signal region. A polynomial of 3^{rd} degree is fitted to the data outside this region (red line). The fitted function is extrapolated to the signal region (red dashed line). The centre of each energy bin is given in each bin in MeV.

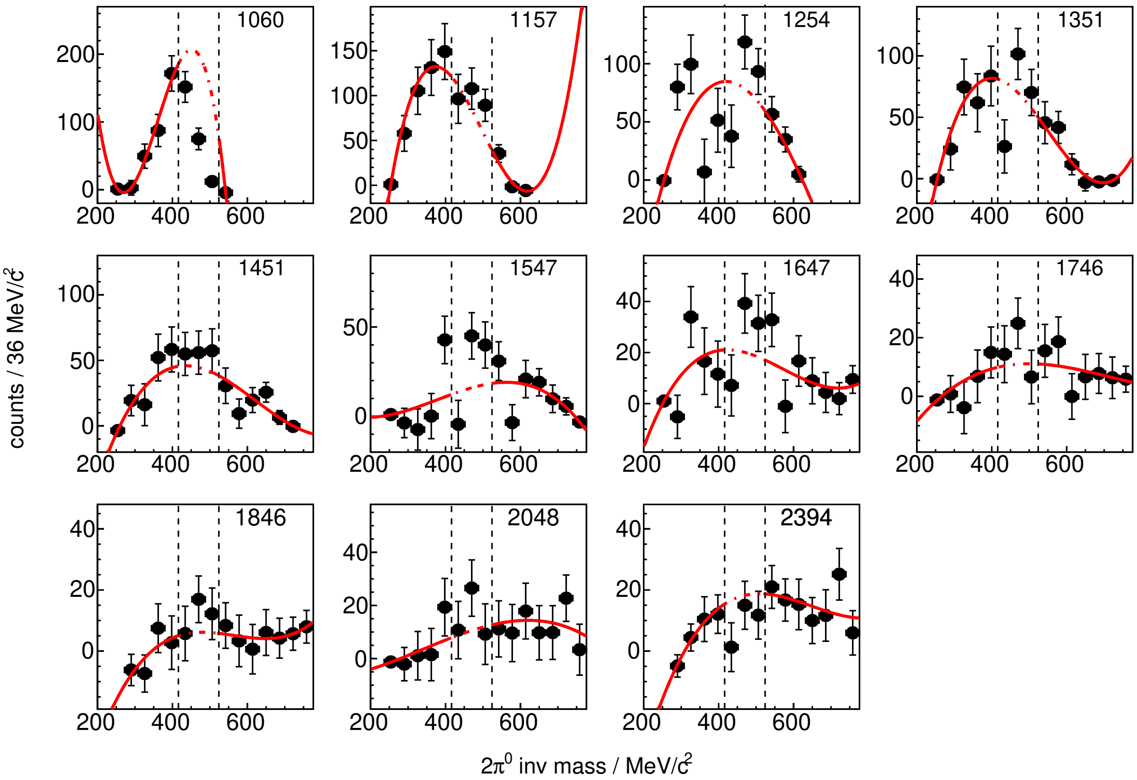

Figure C.2: $2\pi^0$ invariant mass spectrum in the angular range $-0.4 < \cos\theta^K_{\mathrm{CM}} < -0.1$. The region within the black dashed lines is identified as signal region. A polynomial of 3^{rd} degree is fitted to the data outside this region (red line). The fitted function is extrapolated to the signal region (red dashed line). The centre of each energy bin is given in each bin in MeV.

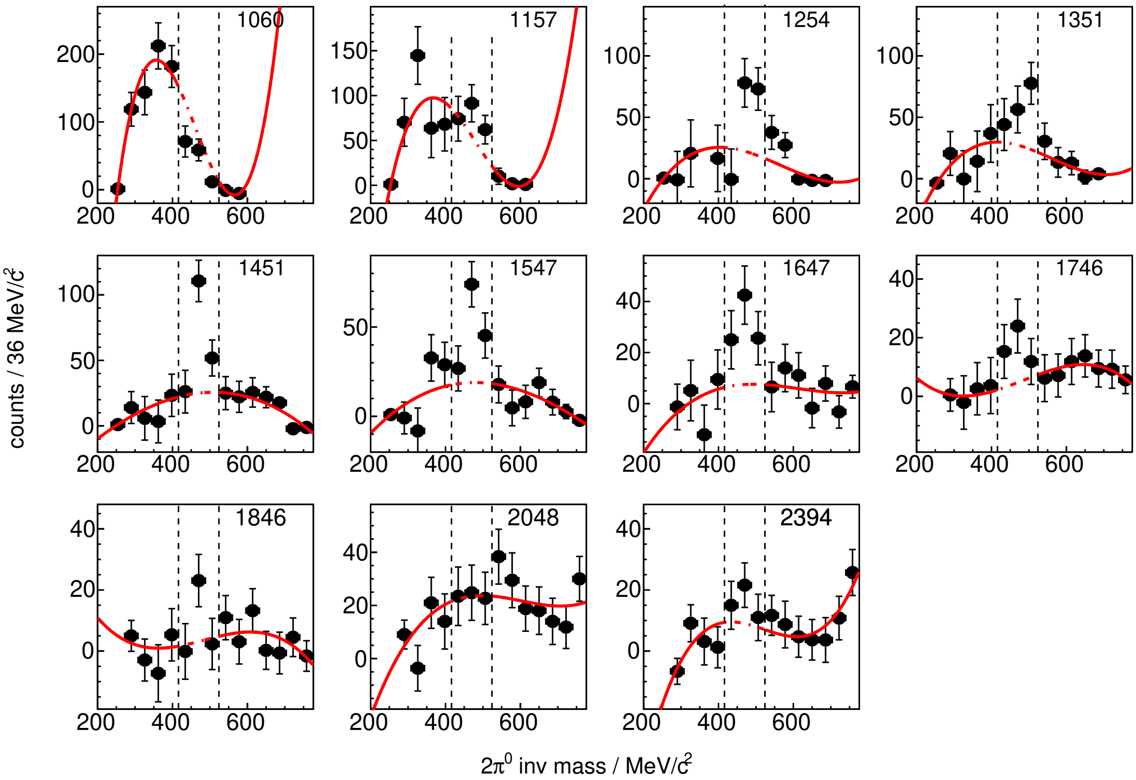

Figure C.3: $2\pi^0$ invariant mass spectrum in the angular range $-0.1 < \cos\theta^K_{\mathrm{CM}} < 0.2$. The region within the black dashed lines is identified as signal region. A polynomial of 3^{rd} degree is fitted to the data outside this region (red line). The fitted function is extrapolated to the signal region (red dashed line). The centre of each energy bin is given in each bin in MeV.

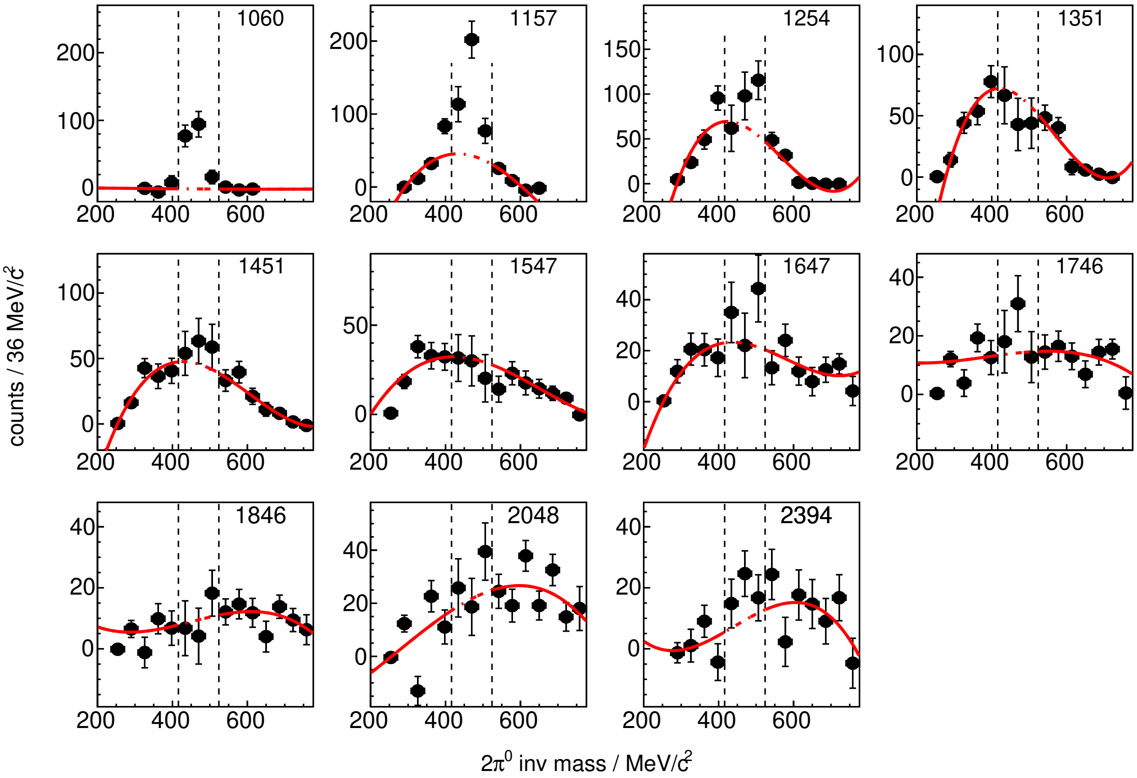

Figure C.4: $2\pi^0$ invariant mass spectrum in the angular range $-0.7 < \cos\theta^K_{\mathrm{CM}} < -0.4$. The region within the black dashed lines is identified as signal region. The data points outside the signal region are averaged as explained in chapter 6.3. A polynomial of 3^{rd} degree is fitted to these data points (red line). The fitted function is extrapolated to the signal region (red dashed line). The centre of each energy bin is given in each bin in MeV.

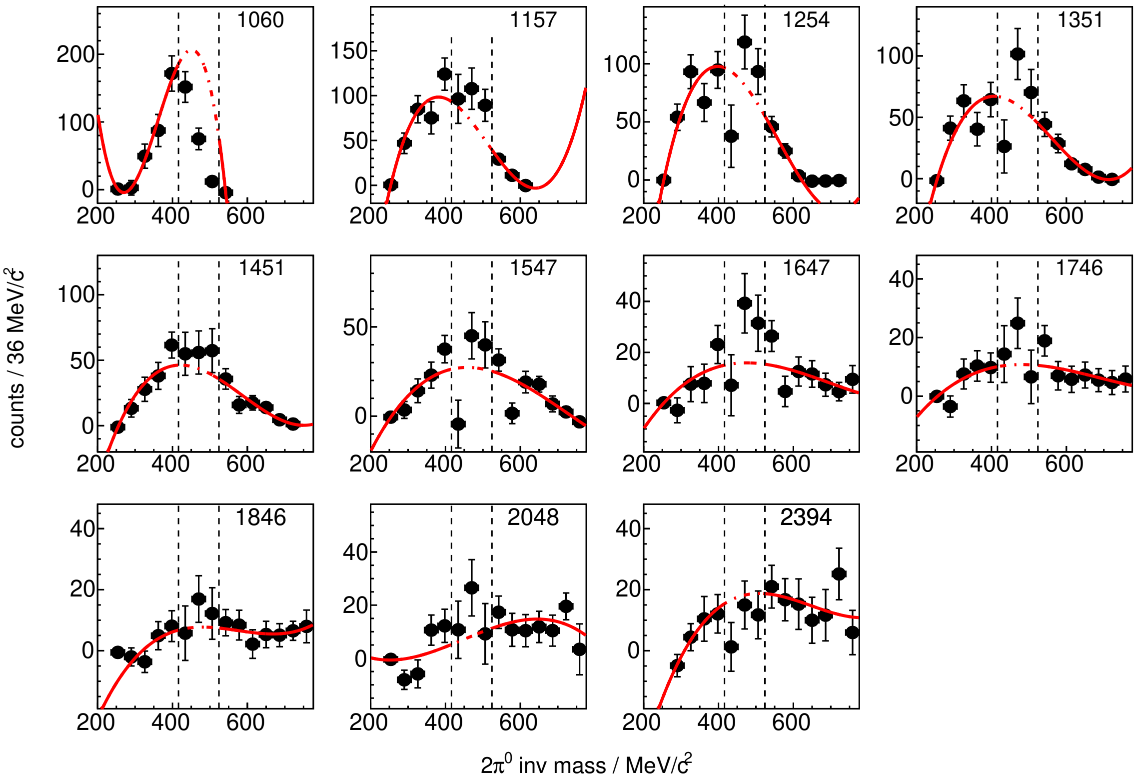

Figure C.5: $2\pi^0$ invariant mass spectrum in the angular range $-0.4 < \cos\theta^K_{\mathrm{CM}} < -0.1$. The region within the black dashed lines is identified as signal region. The data points outside the signal region are averaged as explained in chapter 6.3. A polynomial of 3^{rd} degree is fitted to these data points (red line). The fitted function is extrapolated to the signal region (red dashed line). The centre of each energy bin is given in each bin in MeV.

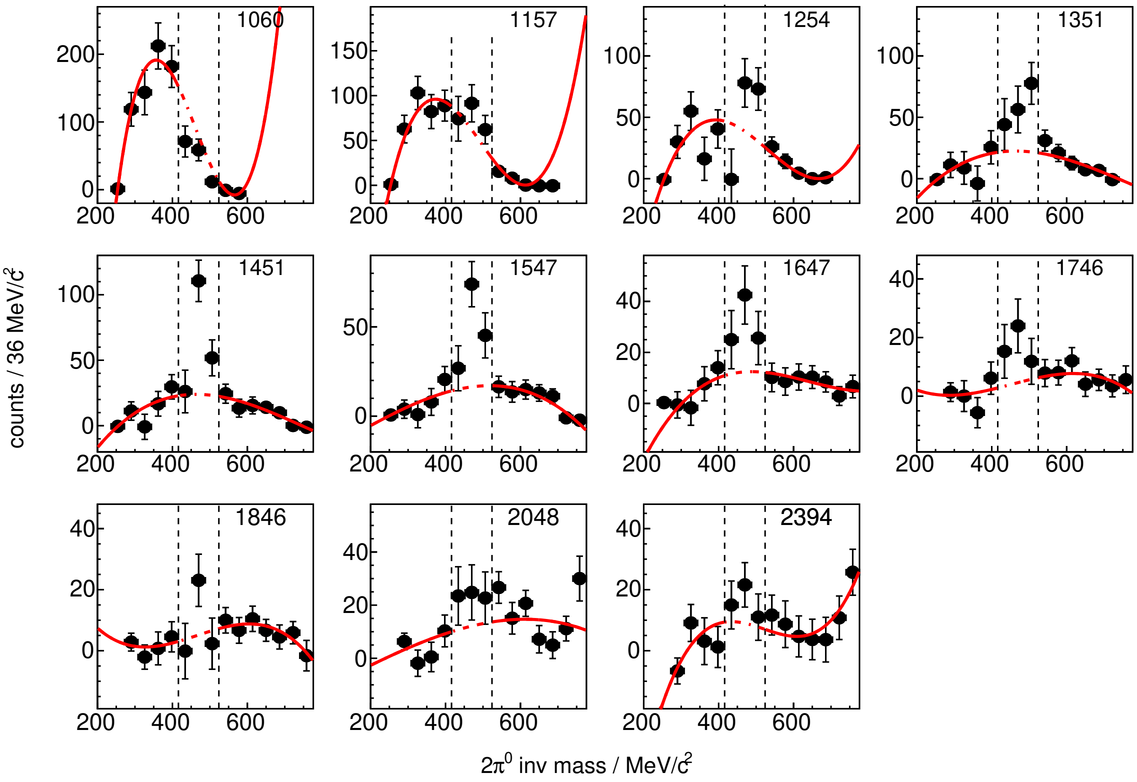

Figure C.6: $2\pi^0$ invariant mass spectrum in the angular range $-0.1 < \cos\theta^K_{\rm CM} < 0.2$. The region within the black dashed lines is identified as signal region. The data points outside the signal region are averaged as explained in chapter 6.3. A polynomial of 3^{rd} degree is fitted to these data points (red line). The fitted function is extrapolated to the signal region (red dashed line). The centre of each energy bin is given in each bin in MeV.

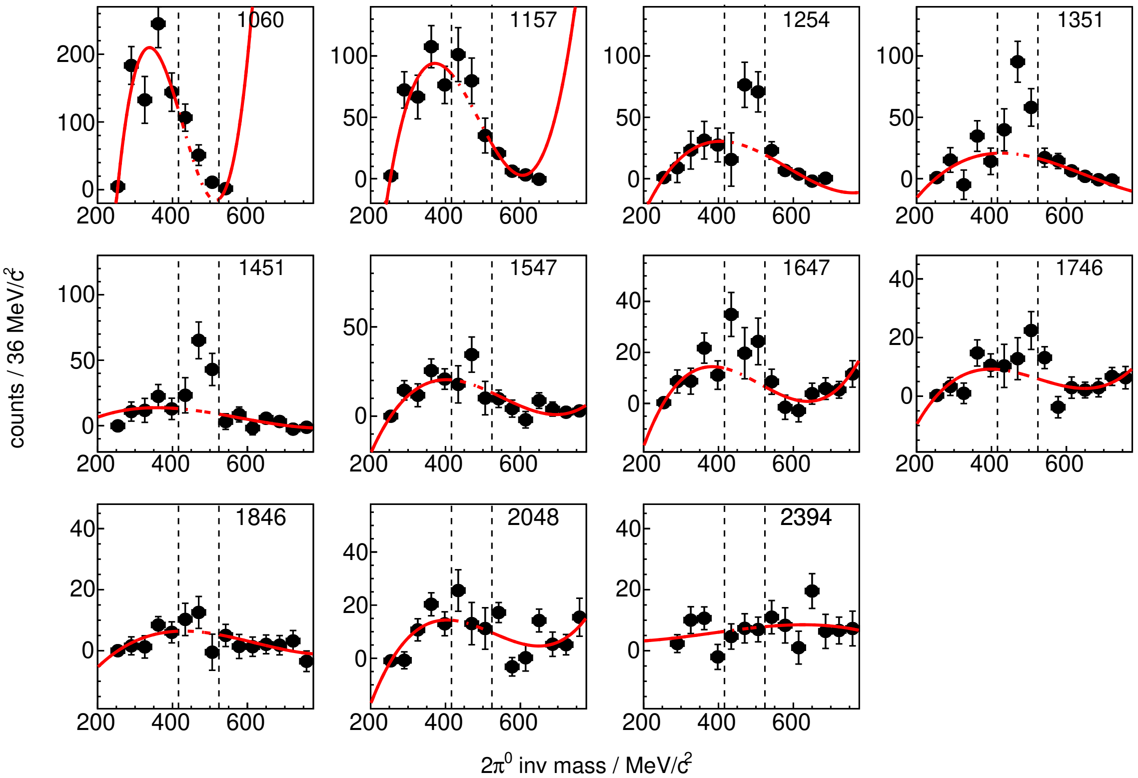

Figure C.7: $2\pi^0$ invariant mass spectrum in the angular range $0.2 < \cos\theta^K_{\mathrm{CM}} < 0.5$. The region within the black dashed lines is identified as signal region. The data points outside the signal region are averaged as explained in chapter 6.3. A polynomial of 3^{rd} degree is fitted to these data points (red line). The fitted function is extrapolated to the signal region (red dashed line). The centre of each energy bin is given in each bin in MeV.

APPENDIX D

Fits to larger angular bin

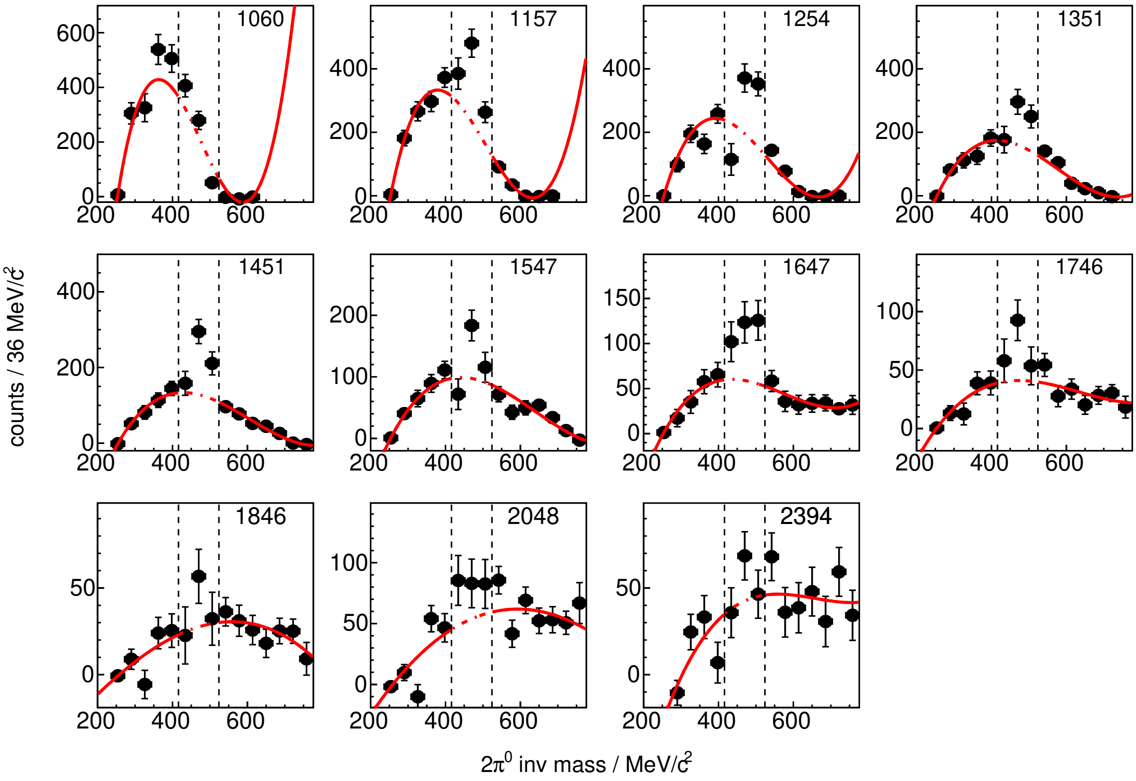

Figure D.1: $2\pi^0$ invariant mass spectrum in the angular range $-0.7 < \cos\theta^K_{\mathrm{CM}} < 0.5$. The region within the black dashed lines is identified as signal region. The data points outside the signal region are averaged as explained in chapter 6.3. A polynomial of 3^{rd} degree is fitted to these data points (red line). The fitted function is extrapolated to the signal region (red dashed line). The centre of each energy bin is given in each bin in MeV.

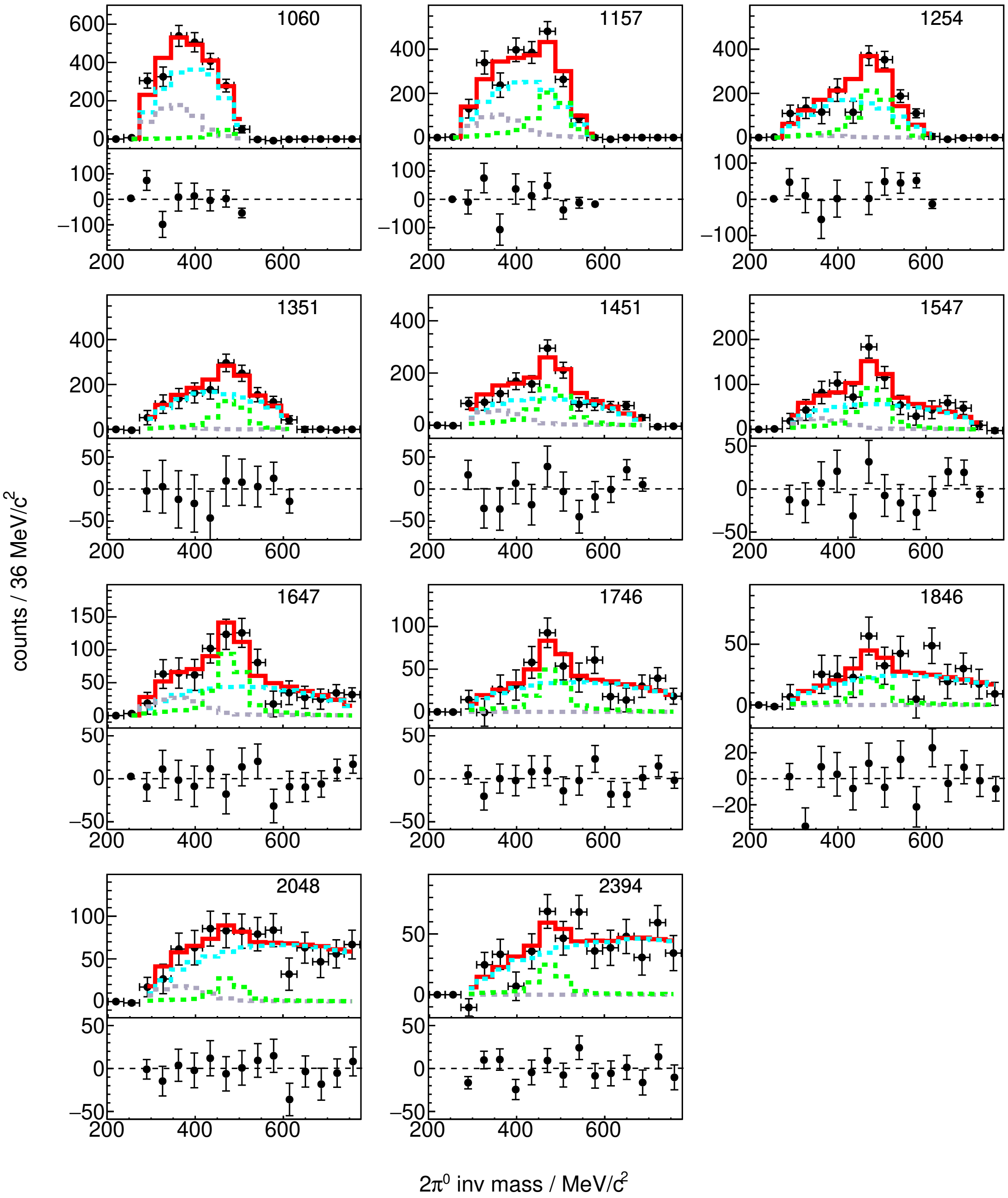

Figure D.2: Fits for all energies in the angular range $-0.7 < \cos\theta^K_{\mathrm{CM}} < 0.5$. The data is fitted with the expected signal spectrum $\gamma n \rightarrow K^0\Sigma^0$(green), $\gamma n \rightarrow \eta n$ (grey) and $\gamma n \rightarrow \pi^0\pi^0\pi^0 n$ (light blue). The full fit is shown in red. Underneath each fit the residuals are shown.

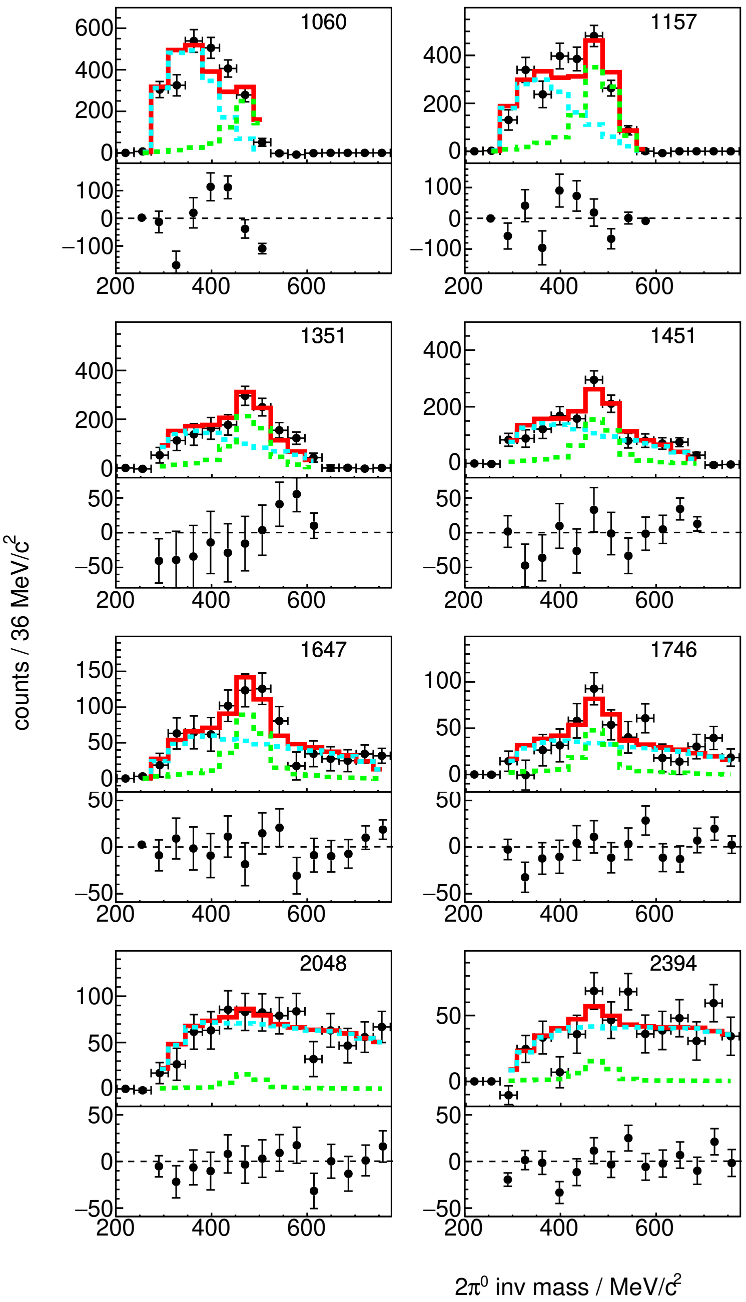

Figure D.3: Fits for all energies in the angular range $-0.7 < \cos\theta^{K}_{\mathrm{CM}} < 0.5$. The data is fitted with the expected signal spectrum from simulated $\gamma n \rightarrow K^0\Sigma^0$ (green) and a background spectrum determined from real data with relaxed cuts (light blue). The full fit is shown in red. Underneath each fit the residuals are shown.

List of Figures

List of Tables